The Dissertation Committee for Tanmoy Pramanik
certifies that this is the approved version of the following dissertation:

Shape-Engineered Ferromagnets and Micromagnetic Simulation Techniques for Spin-Transfer-Torque Random Access Memory

Committee:

Sanjay K. Banerjee, Supervisor

Leonard F. Register, Co-Supervisor

Jack C. Lee

S. V. Sreenivasan

Maxim Tsoi

Shape-Engineered Ferromagnets and Micromagnetic Simulation Techniques for Spin-Transfer-Torque Random Access Memory

by

Tanmoy Pramanik,

DISSERTATION

Presented to the Faculty of the Graduate School of

The University of Texas at Austin

in Partial Fulfillment

of the Requirements

for the Degree of

DOCTOR OF PHILOSOPHY

THE UNIVERSITY OF TEXAS AT AUSTIN

May 2018

To my family

Acknowledgments

First of all, I would like to thank my supervisor Dr. Sanjay Banerjee for giving me the opportunity to work in his group. None of this would have been possible without his continuous guidance, motivation and support throughout my PhD study. I would also like to thank my co-supervisor Dr. Leonard Register for his guidance, enthusiasm and creative thoughts. I possibly can't thank him enough for his tireless effort to make this work publishable. I thank Dr. Maxim Tsoi, Dr. Jack Lee and Dr. S.V. Sreenivasan for being in my PhD committee and sharing their valuable thoughts and suggestions on this work. I am grateful to Dr. Sreenivasan for supporting this work through the NASCENT center.

I would like to thank my mentors, colleagues and friends at the Microelectronics Research Center. Special thanks to Anupam Roy, Urmimala Roy, Samaresh Guchhait, Sushant Sonde, Hema Chandra Prakash Movva and Nima Asoudegi for mentoring and helping me learn the theoretical concepts and experimental techniques. Many thanks to Rik Dey and Amritesh Rai for being my friend and patiently helping me in all possible ways. Special thanks to Urmimama Roy, Anupam Roy and Rik Dey, who helped me almost everyday throughout this work. It has been a privilege to work with you. Thanks to Amithraj Valsaraj, Dax Crum and Dharmendar Reddy for the computing system that I have used aggressively during this work. I also thank Sarmita Majumdar for taking care of the PPMS and Priyamvada Jadaun for her contributions in the last part of this work. Many thanks to Tanuj Trivedi, Nitin Prasad, Xian Wu, Omar B Mohammed, Maruthi Yogeesh, Atresh Sanne, Md. Hasibul Alam, Sayema Chowdhury, Bahniman Ghosh, Kyounghwan Kim, Jaehyun Ahn, Stefano Larentis, Sayan Saha, Donghyi Koh, Andreas Hsieh, Sangwoo Kang, Yujia Zhai and Jason Mantey for their friendship, support and for the wonderful time.

I take this opportunity to thank the staff members at Microelectronics Research Center, especially Ricardo Garcia, William James, Johnny Johnson, Marylene Palard and

David Farnsworth for training me on the tools and for their tireless effort to keep every equipment running. Many thanks to Jean Toll, Christine Wood, Janet Monaco and Melanie Gullick for taking care of all the paperwork from the first day of my graduate study. I would also like to thank my mentor Dr. Christian Kaiser, Dr. Savas Gider and my manager Dr. Qunwen Leng at Western Digital for the opportunity to work with them during the brief internship.

Finally, I thank my parents, *Didi*, *Dada*, brother-in-law and sister-in-law for inspiring me throughout all these years. I could not have done this without *Dada*, who guided me in every step of my career towards a researcher. Special thanks to *Didi* who never forgets to keep an eye on me. Thank you for taking care of me. Last but not the least, I thank my wife Prapti for her endless love and support. Thank you for being patient with me and taking care of me during the most difficult times in the past years.

Shape-Engineered Ferromagnets and Micromagnetic Simulation Techniques for Spin-Transfer-Torque Random Access Memory

Tanmoy Pramanik, Ph.D.
The University of Texas at Austin, 2018

Supervisors: Sanjay K. Banerjee
Leonard F. Register

Spin-transfer-torque random access memory (STTRAM) has received great attention as a prospective universal memory due to high speed read and write capabilities, scalability to smaller technology nodes and non-volatile data retention. Two major factors that could limit the performance of large scale STTRAM arrays are the high switching current and the stochastic switching behavior. In this work, possible routes to mitigate these issues have been explored and new techniques have been proposed to estimate the reliability of the write process. Large area of the selection transistor required to support high switching current impacts the bit storage density of an STTRAM memory array. To increase the bit storage density, a multi-state STTRAM cell employing a cross-shaped ferromagnet was proposed previously. Here, the spin-transfer-torque (STT) driven magnetization dynamics of the cross-shaped ferromagnet is revisited. As a low power alternative, voltage controlled magnetic anisotropy (VCMA) based writing scheme is studied. Trade-offs and limitations of the VCMA-induced switching over STT are also discussed. In the next part of this dissertation, magnetic properties and magnetization process of epitaxial chromium telluride thin films have been studied. Presence of strong perpendicular magnetic anisotropy in this material makes it an attractive choice for device applications. In this work, anisotropy energies of chromium telluride thin films have been estimated from magnetization measurements. The magnetization reversal process is then studied

using analytical models as well as micromagnetic simulations. The last part of this work focuses on the write error rates (WER) of STTRAM. The stochastic write process of STTRAM at finite temperatures gives rise to write errors when a bit fails to switch within the duration of the write pulse. Ultra-low WER on the scale of 10^{-9} or less are desired for practical applications. Micromagnetic simulations are required to capture spatially-incoherent magnetization dynamics inside a ferromagnet, which may effect the WER. In this work, using the techniques of rare event enhancement, reliable calculation of WERs to 10^{-9} is demonstrated while keeping the computational effort to a minimum. Employing rare-event-enhanced micromagnetic simulations, WERs of both perpendicular and in-plane STTRAM bits are calculated and effects of spatially-incoherent excitations on the WER slopes are discussed.

Table of Contents

List of Tables

List of Figures

Chapter 1

Introduction

Transistor scaling following the Moore's law has transformed the computing devices by continuously improving the performance and efficiency of the integrated circuit transistors while reducing the product cost [1]. Continuous dimensional scaling has allowed more components to fit into the integrated circuits expanding the horizon of electronics and computing devices to everyday life. As feature size of integrated circuit elements shrinks to dimensions comparable to only hundred's of atoms, scaling these devices becomes very difficult, if not impossible. This prediction has triggered an intense search for alternative technologies that allow scaling to even smaller dimensions and help the existing devices to meet the performance and efficiency criteria, or completely replace them in future. Solutions targeting both logic and memory applications are being explored [1–3]. The expectation on the future memory technologies has become even more demanding. While the existing memory technologies, such as dynamic random access memory (DRAM), flash memory, and hard disk drives (HDD) are being optimized to their fullest potentials, multiple emerging technologies are also being pursued as a replacement [2, 4–8]. Among the emerging memory devices, spin-transfer-torque random access memory (STTRAM), is being pursued actively as a replacement for one or more levels in the memory hierarchy [9–11]. Aggressive research efforts of the past decades have taken this technology to the prototyping stage and there is now an ongoing effort towards successful commercialization [5]. In this chapter, the basic working principles of STTRAM will be described followed by a discussion that motivates this work. A brief introduction to micromagnetic framework and magnetization dynamics is also provided.

1.1 Spin-transfer-torque random access memory

Ferromagnetic materials have long been used for memory applications—from magnetic core memories used in early generations of computers to high density terabyte hard disk drives (HDD) in today's computers. One of the most important discoveries that led to the modern HDDs and also played a major role in the development of magnetic random access memories (MRAM) is the discovery of giant magneto-resistance (GMR) effect (independently) by Albert Fert [12] and Peter Grunberg [13] in 1988 (awarded Noble prize in Physics in 2007). The GMR effect causes a change in the electrical resistance when the ferromagnetic layers in a Ferromagnet (FM)/Non-magnet (NM)/Ferromagnet (FM) structure change their magnetic orientation. This discovery transformed the way of how information stored as magnetization could be read into electrical signals. Application of this mechanism in the read head of HDDs allowed a much denser storage of digital information. This discovery then was followed by the discovery of tunnel magneto-resistance (TMR), which is similar to GMR, but offers a higher degree of sensitivity than GMR. TMR was first demonstrated experimentally by Julliere in 1975 in an Fe/Ge/Co magnetic tunnel junction (MTJ) with 14% magneto-resistance at 4.2 K [14]. Large TMR effects ($\sim$ 10 to 20% at 300K) were subsequently demonstrated by Miyazaki et al. (in an Fe/Al2O3/Fe MTJ) [15] and Moodera et al. (in a CoFe/Al2O3/Co MTJ) [16] in 1995 leading to the rapid development of MRAM based on these high TMR MTJs. Earlier reports of MRAM also addressed design of GMR based sensing [17, 18]. Following the demonstration of TMR, multiple studies of MRAM with 1-transistor and 1-MTJ memory cell were published [19–22] and MRAM gained widespread importance as a promising nonvolatile memory technology. In these MRAM memory cells the read operation made use of the TMR effect, and the write operation required creating a magnetic field by sending a current through the word line [23]. This generation of MRAM continued to develop for about a decade.

The current generation of MRAM, the so-called spin-transfer-torque random access memory (STTRAM) offers an all-electrical read and write process. The read mechanism remained the same, although discovery of MgO tunnel barrier led to much larger TMR ratios compared to the earlier MTJs with AlO_x tunnel barriers [24–27]. The write

technique is based on the process called spin-transfer-torque switching, discovered by Slonczewski [28] and Berger [29] in 1996. Field switched MRAM is not expected to work as the dimensions of the memory cells are being scaled down aggressively [5]. STTRAM, on the other hand, has been shown to be compatible with scaling to very small dimensions (up to less than 10 nm in lateral dimensions demonstrated in recent years [30–32]). Rapid research and development in both academia and industry during the past decade has enabled STTRAM to reach the prototyping stage and it is expected to appear in commercial products in near future [5].

MRAM (or STTRAM) stores binary information as the relative orientation of two FMs in a MTJ nanopillar (Figure 1.1). Two FM layers are separated by a thin insulating tunnel barrier. As shown in Figure 1.1(a)-(b), the remanent magnetization of the FM layers could be in the plane of the thin film (henceforth referred to as I-MTJ or I-STT), or, along the out-of-plane (perpendicular) direction (henceforth referred to as P-MTJ or P-STT). In the I-MTJ structure, the FM electrodes are usually patterned in an elliptical shape so as to engineer the equilibrium energy valleys of the magnets. The equilibrium energy valleys of the magnets in a P-MTJ structure is governed by the perpendicular anisotropy energy and these magnets are usually patterned in a circular shape. The read mechanism relies on the TMR effect which results into a low resistance, R_{P}, or high resistance, R_{AP}, of the two terminal MTJ nanopillar when the magnetization of the two FM layers are parallel (P) or anti-parallel (AP), respectively. The difference in resistance between these two states defines the TMR ratio as,

$$TMR = \frac{R_{\mathrm{AP}} - R_{\mathrm{P}}}{R_{\mathrm{P}}}. \tag{1.1}$$

Typical MTJ nanopillars used in the memory arrays have TMR ratios of $\sim$100% - 200% [5]. Figure 1.1(c) shows example of an STTRAM memory array with four memory cells. Due to low ON-OFF ratio of the MTJ, usually a selection transistor is required in each cell connected in series with the MTJ.

TMR effect can be explained assuming a spin-dependent tunneling transport across the tunnel barrier. The tunneling process is assumed to be spin-conserving i.e., the majority spin from one electrode can only tunnel to the majority spin states on the other

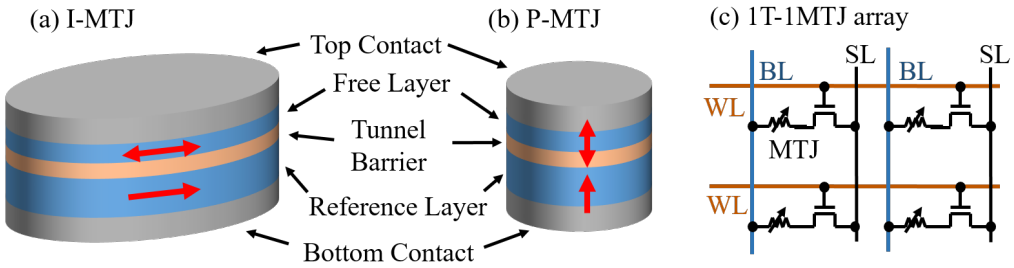

Figure 1.1: Simplified schematic of an MTJ with (a) in-plane magnetized FMs (I-MTJ) and (b) perpendicular magnetized FMs (P-MTJ). (c) Typical memory array with 1-transistor 1-MTJ memory cells.

electrode. The band-structure of the majority and minority electrons in the FM electrodes are split by an exchange interaction that creates an asymmetry of the density of states at the Fermi energy for the two spin channels. In the AP state, as in Figure 1.2(a) for both spin channels the tunneling probability is reduced as either type of carrier sees a reduced density of states at the Fermi energy at one of the FM electrodes. In the P state, as in Figure 1.2(b), for the majority channel there are enough states available at both the electrodes, increasing the tunneling probability. Hence the P state shows a lower resistance than the AP state. Based on these simplified assumptions, Julliere suggested the following relation between the TMR and the degree of spin-polarization of the ferromagnetic electrodes [33],

$$TMR = \frac{2P_1P_2}{1 - P_1P_2}, \tag{1.2}$$

where P_1 and P_2 are spin polarization of density of states at the Fermi energy in the ferromagnetic electrodes. However, tunnel barrier dielectric does play a role in achieving high TMR, as was established later by more detailed theories as well as experimental results [33]. TMR values more than 600% at 300 K has been achieved so far using CoFe ferromagnetic electrodes and MgO tunnel barrier [34].

The write process changes the magnetic orientation of one of the FM layer, the so-called "free" layer (FL) FM in the MTJ stack. The other FM layer is designed to remain magnetized along a predefined direction and hence referred to as the "fixed" or "reference" layer (RL) FM. As mentioned previously, earlier generations of MRAMs used a magnetic field induced switching process where the magnetic field required for

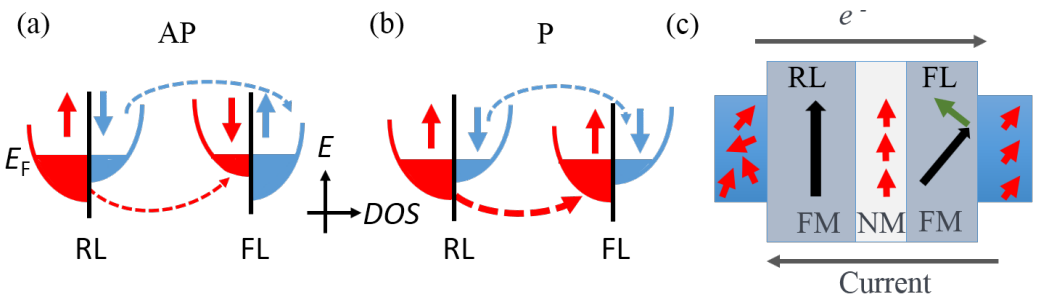

Figure 1.2: Read (TMR) and write (STT) processes in an MTJ. (a) & (b) explain the transport mechanism using spin-dependent tunneling processes (dotted arrows) for AP (a) and P (b) configurations of the FM electrodes. STT switching process for AP to P transition is explained in (c). Small RED arrows denote electron spin and small green arrow is the direction of the torque.

the switching is generated by a current carrying wire. The STT-induced switching offers a more controlled and efficient way of switching. The STT write process for the AP to P transition is illustrated in Figure 1.2(c). Unpolarized electrons enter the fixed FM and get spin-polarized according to the direction of the fixed FM. These spin-polarized electrons then tunnel through the tunnel barrier and enter the free FM. Electrons coming out at the right end of the tunnel junction again follow the polarization direction of the free FM. If the magnetic orientation of the free FM is different from that of fixed FM, electrons must have transferred their angular momentum as they traveled through the free FM. This angular momentum exerts a torque on the free FM that tries to align the free FM towards the fixed FM. When the current direction is reversed, through a similar process of angular momentum transfer (via the reflected electrons [35]), the free layer aligns anti-parallel to the fixed layer. The switching times of the memory element and the retention properties (the magnetic bit stability) will depend on the magnetic properties of the FM layers and the spin-filtering properties of their interfaces with the tunnel barrier. The next section introduces the theoretical framework that will be used throughout this dissertation to describe magnetic properties and magnetization dynamics of these magnets.

1.2 Micromagnetic framework and magnetization dynamics

Knowledge of equilibrium magnetization configurations, their long term stability under real operating conditions, and STT-induced dynamics is necessary for quantitative understanding of STTRAM. Micromagnetic simulations are very useful for this purpose. The term *micromagnetics* was first introduced by Brown [36]. Within the micromagnetic framework, magnetization of a ferromagnetic material is treated as a classical vector of fixed length (equals the saturation magnetic moment $M_{\rm s}$) with its direction allowed to vary continuously over spatial coordinates [37]. The space-varying magnetization vector is then represented as $M_{\rm s}\bar{m}(\bar{r})$, where, $\bar{m}(\bar{r})$ is the space-varying unit vector pointing at the direction of magnetization. The basic energy terms required to describe the magnetization processes are the exchange, magnetostatic and anisotropy energy terms (where, depending on the material under consideration the latter term may be omitted). Minimizing this total energy functional with respect to the magnetization, equilibrium magnetization states are then obtained. The gradient of this energy with respect to magnetization is the effective field that governs the magnetization dynamics.

The total energy $E_{\rm Total}$ for a given magnetization distribution $\bar{m}(\bar{r})$ for a ferromagnet of volume V can be written as,

$$E_{\rm Total} = \int_V \left[A_{\rm ex} \left(|\nabla \bar{m}|\right)^2 - \frac{1}{2}\mu_0 M_{\rm s}(\bar{H}_{\rm d} \cdot \bar{m}) + e_{\rm anisotropy} - \mu_0 M_{\rm s}(\bar{H}_{\rm ext} \cdot \bar{m}) \right], \quad (1.3)$$

where the first three terms correspond to the exchange, magnetostatic and anisotropy energies, respectively, and the fourth term takes into account the Zeeman energy due to the applied magnetic field $\bar{H}_{\rm ext}$. Note that SI unit has been followed in the above equation and same will be used for the rest of the dissertation. The exchange energy term, $A_{\rm ex}|\nabla \bar{m}|^2$, contains the information of quantum-mechanical exchange interaction. This term is the continuum form of the well-known Heisenberg exchange interaction. $A_{\rm ex}$ is the exchange coefficient used in the micromagnetic description.

The magnetostatic energy term, also known as the stray field energy or demagnetizing energy, accounts for the classical interactions among the magnetized particles within the ferromagnet's body. As it originates from the magnetization itself, it is also

called magnetostatic self energy. This energy and the corresponding demagnetizing field, $\bar{H}_{\rm d}$, can be evaluated from the Maxwell's equations [37, 38]. From Maxwell's equations, in absence of charge and displacement currents, one obtains $\bar{\nabla} \times \bar{H}_{\rm d} = 0$. Hence $\bar{H}_{\rm d}$ can be expressed as the gradient of a scalar potential, such that $\bar{H}_{\rm d} = -\bar{\nabla}U$, where the negative sign is used as a convention. Again from another of Maxwell's equations one obtains $\bar{\nabla} \cdot \bar{B} = 0$. Substituting $\bar{B} = \mu_0(\bar{H}_{\rm d} + M_{\rm s}\bar{m})$ and $\bar{H}_{\rm d} = -\bar{\nabla}U$ in $\bar{\nabla} \cdot \bar{B} = 0$ gives,

$$\nabla^2 U = M_{\rm s}\bar{\nabla} \cdot \bar{m}. \tag{1.4}$$

In the above equation $\bar{\nabla} \cdot \bar{M}$ acts the magnetic charge density. Outside the ferromagnetic region $M_{\rm s} = 0$, giving $\nabla^2 U = 0$. Then at the boundary $\bar{H}_{\rm d}$ parallel to the surface is continuous, and $\bar{B}$ perpendicular to the surface is continuous. These two constraints result in to two boundary conditions for U. Solving the above equation with the boundary conditions, $\bar{H}_{\rm d}$ is obtained.

The anisotropy energy can be of different forms depending on the symmetry of the crystal structure of the ferromagnetic material. For the purpose of this dissertation, only uniaxial anisotropy is discussed here. More information on anisotropy can be found in [37, 38]. Uniaxial anisotropy attempts to align the magnetic moments $\bar{m}$ within the material along a certain crystal axis (easy axis type) or away from the axis (easy plane type). This type of anisotropy could arise in a material with, e.g., a hexagonal crystal structure [38]. In thinner ferromagnetic films, interface anisotropy also can act as a source of uniaxial anisotropy [39, 40]. For both cases, the anisotropy energy can be written as [37, 38],

$$e_{\rm anisotropy} = K_{\rm u1}\left[1 - (\bar{u} \cdot \bar{m})^2\right] + K_{\rm u2}\left[1 - (\bar{u} \cdot \bar{m})^2\right]^2 + ..., \tag{1.5}$$

where $\bar{u}$ is the anisotropy axis, $K_{\rm u1}$ is the first order anisotropy term, and $K_{\rm u2}$ is the second order anisotropy term. Higher order terms (including $K_{\rm u2}$) are usually negligible. Again, for the materials and devices considered in this dissertation, only perpendicular magnetic anisotropy (PMA) is relevant. For PMA $\bar{u} = \hat{z}$ with $\hat{z}$ being the out-of-plane normal (along the thickness) direction of the ferromagnetic thin film. Replacing $\bar{u}$ with $\hat{z}$ in the above equation, one obtains,

$$e_{\rm anisotropy} = K_{u1}\left[1 - \cos^2\theta\right] + K_{u2}\left[1 - \cos^2\theta\right]^2 + ..., \tag{1.6}$$

where θ is the polar angle (angle between the vectors $\hat{z}$ and $\bar{u}$) of magnetization $\bar{m}$.

The effective magnetic field $\bar{H}_{\text{eff}}$ can be obtained from E_{Total} as,

$$\bar{H}_{\text{eff}}(\bar{r}) = -\frac{1}{\mu_0 M_{\text{s}}} \nabla_{\bar{m}} \left[A_{\text{ex}} \left(|\nabla \bar{m}| \right)^2 - \frac{1}{2} \mu_0 M_{\text{s}} (\bar{H}_{\text{d}} \cdot \bar{m}) + e_{\text{anisotropy}} - \mu_0 M_{\text{s}} (\bar{H}_{\text{ext}} \cdot \bar{m}) \right], \tag{1.7}$$

where $\nabla_{\bar{\text{m}}} = \left(\begin{array}{ccc} \hat{x} \frac{\partial}{\partial m_{\text{x}}}, & \hat{y} \frac{\partial}{\partial m_{\text{y}}}, & \hat{z} \frac{\partial}{\partial m_{\text{z}}} \end{array} \right)$ denotes differentiation with respect to the magnetization $\bar{m} = \left(\begin{array}{ccc} m_{\text{x}}, & m_{\text{y}}, & m_{\text{z}} \end{array} \right)$. The dynamics of the magnetic moments under this effective magnetic field then is obtained from the Landau-Lifshitz-Gilbert (LLG) equation,

$$\frac{d\bar{m}}{dt} = -\gamma \left(\bar{m} \times \bar{H}_{\text{eff}} \right) - \alpha \left(\bar{m} \times \frac{d\bar{m}}{dt} \right). \tag{1.8}$$

In the above equation, $\gamma = 2.21 \times 10^5$ m/A·s is the gyromagnetic ratio and α is the Gilbert damping constant. The first term accounts for a precessional motion of the magnetic moment $\bar{m}(\bar{r})$ around the effective magnetic field $\bar{H}_{\text{eff}}(\bar{r})$. The second term then accounts for different energy dissipation processes that eventually align the magnetic moments to the direction of local effective magnetic fields.

In presence of spin-transfer-torque two more terms are then added to the above equation as,

$$\frac{d\bar{m}}{dt} = -\gamma \left(\bar{m} \times \bar{H}_{\text{eff}} \right) - \alpha \left(\bar{m} \times \frac{d\bar{m}}{dt} \right) + \gamma\beta\epsilon \left(\bar{m} \times (\bar{m}_{\text{p}} \times \bar{m}) \right) - \gamma\beta\epsilon_{\text{p}} \left(m \times m_{\text{p}} \right). \tag{1.9}$$

The third and fourth terms in the above equation are known as the Slonczewski-like and field-like torque terms, respectively. The factor $\beta = \frac{\hbar}{\mu_0 q} \frac{J}{t_{\text{FL}} M_{\text{s}}}$, where J is the charge current density, $q = 1.6 \times 10^{-19}$ Coulomb is the magnitude of electron charge. $\epsilon = \eta/2$, where η is the spin-polarization of the charge current. The factor ϵ_{p} is usually smaller than ϵ and will be ignored in most of the discussions in this dissertation unless otherwise specified. The above equation with the Slonczewski-like term also is referred to as the Landau-Lifshitz-Gilbert-Slonczewski (LLGS) equation. Equation 1.9 can be represented in the equivalent Landau-Lifshitz form as,

$$\frac{d\bar{m}}{dt} = -\gamma' \left(\bar{m} \times \bar{H}_{\text{eff}} \right) - \alpha\gamma' \left(\bar{m} \times \left(\bar{m} \times \bar{H}_{\text{eff}} \right) \right) + \gamma'\beta \left(\epsilon + \alpha\epsilon_{\text{p}} \right) \left(\bar{m} \times (\bar{m}_{\text{p}} \times \bar{m}) \right) - \gamma'\beta \left(\epsilon_{\text{p}} - \alpha\epsilon \right) \left(m \times m_{\text{p}} \right), \tag{1.10}$$

where $\gamma' = \frac{\gamma}{1+\alpha^2}$. In micromagnetic simulations [41, 42], the above equation is then numerically integrated with appropriate boundary conditions. To obtain the magnetization dynamics, an initial magnetization state also is required. To obtain the initial equilibrium magnetization configuration, the STT terms in Equation 1.10 are set to zero and the time integration is continued for sufficiently long times such that the $\frac{d\bar{m}}{dt}$ term becomes negligible. Alternatively, the equilibrium magnetization configuration may be obtained by direct energy minimization.

State-of-the art micromagnetic simulators such as Object Oriented Micromagnetic Framework (OOMMF) [41] or MuMax3 [42] allow one to study magnetization dynamics as well as equilibrium magnetic states over ferromagnetic volumes of arbitrary shapes and sizes. Micromagnetic simulations described in subsequent chapters are performed using these two codes. However, for the purpose of STTRAM, useful insights from the above equations can be obtained by approximating the magnetization $\bar{m}$ to be uniform over the volume of the ferromagnet. This approximation, the so-called "macrospin approximation," is often sufficient to obtain an estimate of the switching current, switching time and retention properties of an STTRAM bit, as the ferromagnetic electrodes are usually patterned in nanoscale dimensions.

1.2.1 Macrospin approximation

Assuming an uniformly magnetized ferromagnet, the demagnetizing field can be written in the form $\bar{H}_{\mathrm{d}} = -M_s N \bar{m}$, where N is the demagnetizing tensor with only diagonal terms N_{xx}, N_{yy}, N_{zz} being non-zero and $N_{\mathrm{xx}} + N_{\mathrm{yy}} + N_{\mathrm{zz}} = 1$ [37]. The factors N_{xx}, N_{yy} and N_{zz} can be determined from Aarhoni's formula [43] for FMs of rectangular shape, or by using micromagnetic simulations for other simple shapes (e.g., ellipses or circles) [44]. The total energy (Equation 1.3) within the macrospin approximation can be written as (expressing demagnetizing energy using the above factors, and a first order uniaxial anisotropy energy with anisotropy axis along the out-of-plane z direction),

$$E_{\mathrm{Total}} = V\left[\frac{1}{2}\mu_0 M_{\mathrm{s}}^2\left(N_{\mathrm{xx}}m_{\mathrm{x}}^2 + N_{\mathrm{yy}}m_{\mathrm{y}}^2 + N_{\mathrm{zz}}m_{\mathrm{z}}^2\right) + K_{\mathrm{u1}}(1 - m_{\mathrm{z}}^2)\right], \tag{1.11}$$

where V is the volume of the bit and $\bar{m} = \begin{pmatrix} m_{\mathrm{x}}, & m_{\mathrm{y}}, & m_{\mathrm{z}} \end{pmatrix}$ is the magnetization vector of the uniformly magnetized ferromagnetic body. For an I-STT bit, the FL magnet is patterned in an elliptic shape and has negligible uniaxial anisotropy ($K_{\mathrm{u1}} = 0$). Assuming the major axis of the elliptic FM along the $\hat{x}$ direction and minor axis along the $\hat{y}$ direction, Equation 1.11 gives two energy minima along $\bar{m} = \pm\hat{x}$. The minimum energy barrier separating these two minima then decides the thermal stability factor Δ of the equilibrium states. For the I-STT bit with elliptic magnet, from the above equation, one obtains,

$$\Delta^{\mathrm{I-STT}} = \frac{V}{k_{\mathrm{B}}T}\frac{1}{2}\mu_0 M_{\mathrm{s}}^2\left(N_{\mathrm{yy}} - N_{\mathrm{xx}}\right) = \frac{V}{k_{\mathrm{B}}T}\frac{1}{2}\mu_0 M_{\mathrm{s}} H_{\mathrm{K}}^{\mathrm{I-STT}}, \tag{1.12}$$

where k_{B} is the Boltzmann's constant and T is the temperature. In the expression on the far right of Equation 1.12, it is useful to define the shape-anisotropy field as $H_{\mathrm{K}}^{\mathrm{I-STT}} = M_{\mathrm{s}}\left(N_{\mathrm{yy}} - N_{\mathrm{xx}}\right)$. The retention time τ_{life} is related to Δ by the Néel-Brown relaxation model [45, 46], with $\tau_{\mathrm{life}} = \tau_0 \exp(\Delta)$. For ~10 years of retention, $\Delta \geq 40$ is required. For the I-STT bit, the thermal stability $\Delta^{\mathrm{I-STT}}$ then is controlled by the factors N_{xx} and N_{yy}. These factors again are decided by the aspect ratio of the elliptic or rectangular FM.

For a P-STT bit of circular shape $N_{\mathrm{xx}} = N_{\mathrm{yy}}$. Strong perpendicular anisotropy energy K_{u1} prefers out-of-plane alignment of the magnet, giving two equilibrium states along $\bar{m} = \pm\hat{z}$. The thermal stability factor for the P-STT bit becomes,

$$\Delta^{\mathrm{P-STT}} = \frac{V}{k_{\mathrm{B}}T}\frac{1}{2}\mu_0 M_{\mathrm{s}}\left[\frac{2K_{\mathrm{u1}}}{\mu_0 M_{\mathrm{s}}} - (N_{\mathrm{zz}} - N_{\mathrm{xx}})M_s\right] = \frac{V}{k_{\mathrm{B}}T}\frac{1}{2}\mu_0 M_{\mathrm{s}} H_{\mathrm{K}}^{\mathrm{P-STT}}, \tag{1.13}$$

where, $H_{\mathrm{K}}^{\mathrm{P-STT}} = \left[\frac{2K_{\mathrm{u1}}}{\mu_0 M_{\mathrm{s}}} - (N_{\mathrm{zz}} - N_{\mathrm{xx}})M_s\right]$, is the effective perpendicular anisotropy field. In this case the thermal stability factor is largely controlled by the product $K_{\mathrm{u1}}V$ and weakly dependent on the shape of the magnet.

The macrospin approximation also gives an analytical estimate of the critical current requited to switch the free layer magnet between the equilibrium energy valleys. The critical current required to destabilize an energy minima can be obtained from the stability condition of the linearized LLGS equation [47, 48]. For an I-STT bit, the critical current for STT switching, neglecting the field-like torque and anisotropy terms, can be

expressed as,

$$I_{c0}^{\mathrm{I-STT}} = \frac{\alpha\mu_0 qVM_s^2}{2\hbar\epsilon}\left[N_{yy} + N_{zz} - 2N_{xx}\right] = \frac{\alpha q}{\hbar\epsilon}\left[k_B T\Delta^{\mathrm{I-STT}} + \frac{1}{2}\mu_0 M_s^2(N_{zz} - N_{xx})\right]. \tag{1.14}$$

Similarly, the critical current for a P-STT bit, neglecting the field-like torque term, becomes,

$$I_{c0}^{\mathrm{P-STT}} = \frac{2\alpha qV}{\hbar\epsilon}\left[K_{u1} - \frac{1}{2}\mu_0 M_s^2(N_{zz} - N_{xx})\right] = \frac{2\alpha q}{\hbar\epsilon}k_B T\Delta^{\mathrm{P-STT}}. \tag{1.15}$$

In Equation 1.14, for the I-STT bit $\frac{1}{2}\mu_0 M_s^2(N_{zz} - N_{xx}) \gg k_B T\Delta^{\mathrm{I-STT}}$. Due to the additional factor of $\frac{1}{2}\mu_0 M_s^2(N_{zz} - N_{xx})$, the critical switching current for an I-STT bit will be much higher than a P-STT bit of same thermal stability. With typical values of material parameters, the switching current density obtained from the above equations are of the order of 10^{10} A/m^2 [45, 47]. Also, the above equations are only valid in the zero temperature limit. For finite temperature simulations, a random fluctuating field term is added to the effective field in the LLGS equation. Hence magnetization dynamics at finite temperature is stochastic [49–51]. Details of the stochastic LLGS equation and stochastic write process at a finite temperature will be discussed in Chapter 4.

1.3 Dissertation overview

Two key points to note from the discussion above is that: (1) the critical switching current of an STTRAM bit is quite high, and (2) the write process is stochastic. To ensure a fast and reliable write operation, a relatively high current (higher than the critical current) must be applied. The area of the selection transistor required to support such a large current is much bigger than the area of the MTJ itself (the transistor area could be as large as ~ 10 times the the MTJ area [5]). Thus the STTRAM cell area is limited by the selection transistor size. To achieve higher memory density, switching current must be reduced. Materials with ultra-low damping and/or higher spin-torque efficiency can lower the switching current without affecting the thermal stability. Another option is to accommodate multiple bits within a single cell while having the same transistor area. The latter approach is explored in this work. As shown in a previous work [7], by

using a cross-shaped magnet as the free layer, four equilibrium state could be realized and two bits could be stored within a single MTJ. In Chapter 2, we revisit this idea of a shape-engineered FM and investigate low power switching mechanisms for this multi-state memory cell.

As explained in the previous section, in order to achieve a lower critical current density while meeting the long term storage criterion, magnets with perpendicular magnetic anisotropy are more attractive than in-plane magnets. The thermal stability factor, Δ of a P-STT bit (Equation 1.13) is roughly proportional to the product of the anisotropy strength per unit volume K_{u1}, and the volume of the bit V. Thus as the free layer volume is scaled down, materials with higher K_{u1} would be required to maintain $\Delta \geq 40$. This has triggered a search for materials with higher PMA energy [11, 52]. In Chapter 3, we focus on the magnetic anisotropy and magnetization reversal in chromium telluride thin films with strong perpendicular magnetic anisotropy. Although for device applications patterned magnets are usually required, material property of the ferromagnetic materials are often studied using thin films. Chapter 3 also serves to explain how material properties are determined from the magnetization vs. applied field measurements.

In Chapter 4 and 5, we focus on the stochastic write process of STTRAM, especially the problem of estimating write error probabilities. The probability that the free layer remains unswitched at the end of a finite duration current pulse is called the write error rate (WER). For practical applications WER needs to be lower than a certain value e.g., 10^{-9} [11] depending on the error correction capabilities. WER can be modeled precisely within the macrospin approximation from the Fokker-Planck equation. However, the free layer FM may not always follow a macrospin model. Spatially-incoherent magnetization states excited by the combined effects of STT and thermal fluctuations may influence the switching process and the WER. Micromagnetic simulations are required to capture such spatially-incoherent switching processes. Number of independent simulations required for reliable estimation of such ultra-low WERs makes this approach infeasible. In Chapter 4 and 5, a new method is proposed which enables computation of such ultra-low WER of an STTRAM bit including micromagnetic effects. In Chapter

4, we focus on the WER of a P-STT bit. The case of an I-STT bit is then discussed in Chapter 5.

Chapter 6 concludes the dissertation by summarizing the key findings and identifying potential future research directions.

Chapter 2

Cross-shaped ferromagnet based multi-state magnetic memory

To meet the switching current requirement of a STTRAM cell a large selection transistor is required, which limits the bit packing density of the memory array. Even for the state-of-the art perpendicular STTRAM technology, with the transistor being 5-10 times larger than the area of the MTJ [5], the cell area could be up to $\sim$14-20F^2. To improve the information storage density of STTRAM memory arrays, multi-level cells (MLCs) have been studied where the storage density could be improved by storing more than one bit within a single cell [53, 54]. To store n bits in one cell, 2^n different states (equilibrium magnetic states, each with a unique resistance) are required. A two bit/cell memory could be realized by connecting two different MTJs in series or parallel to each other, with each MTJ switching at a different current density [55–57]. Similar MLC STTRAM structures have also been studied where the STT mechanism is replaced by a spin-orbit-torque (SOT) or spin-Hall-effect (SHE) based writing scheme [58, 59]. However it could be difficult to extend this technique to more than two bit/cell using either of these approaches. Another possible route to achieve higher packing density is to explore circuit level solutions where multiple single bit MTJs can be accessed by a single

The results reported in this chapter have been published in: (1) "Micromagnetic simulations of spin-wave normal modes and the spin-transfer-torque driven magnetization dynamics of a ferromagnetic cross" by T. Pramanik, U. Roy, M. Tsoi, L. F. Register, S. K. Banerjee in Journal of Applied Physics, vol. 115, no. 17, pp. 17D123, 2014. (2) "Proposal of a Multistate Memory Using Voltage Controlled Magnetic Anisotropy of a Cross-Shaped Ferromagnet" by T. Pramanik, U. Roy, L. F. Register, S. K. Banerjee, in IEEE Transactions on Nanotechnology, vol. 14, issue 5, pages 883-888, 2015. Contributions: T. Pramanik carried out the micromagnetic simulations, T. Pramanik and U. Roy wrote the manuscripts, M. Tsoi, L. F. Register and S. K. Banerjee supervised the work, and all authors reviewed and commented on the results and the manuscript. T. Pramanik is the corresponding author for the publications.

selection transistor [60–63]. More disruptive solutions have also been explored recently using domain wall motion confined in magnetic nanotracks to realize more than two resistance states [64, 65]. In this work, we'll explore an option that modifies the shape of the free layer (FL) ferromagnet (FM) to create more than two energy minima with each of them having a distinct resistance value. Nanomagnets of various complex shapes were previously studied for a wide range of device applications [66–70]. An approach very similar to the one discussed here was also proposed previously in a patent [71] where the possibility of storing up to three bits (eight states) within a single FM was mentioned. A more recent study showed six magnetic states in a similar shape-engineered FM [72]. This approach has the advantage that the structure of the MTJ remains same as for a single bit case, and it could be extended to more than two bit/cell storage. However, details of the write process that involves magnetization switching were not reported. Our previous study focusing on the STT-induced write mechanism of a cross-shaped FM (a two bit per cell memory) revealed complex switching dynamics and very large write current requirement [7, 73] that outweighs the benefit of a multi-state memory.

In this chapter, first, our previous work [73] on the cross-shaped FM based two bits/cell STTRAM is summarized. Next, magnetic normal modes of such a shape-engineered FM are studied to understand the origin of complex switching dynamics observed previously [74]. Finally, to lower the write energy, a voltage controlled switching mechanism [75] of a similar shape-engineered structure is studied.

2.1 Cross-shaped ferromagnet for two bits/cell STTRAM

The multi-state concept explored in [7] is schematically shown in Figure 2.1. Magnetization easy direction of an elongated particle, such as a rectangle or an ellipse follows the long axis of the element [Figure 2.1(a)]. Guided by the same intuition, more than one easy direction possibly could be designed by adding another easy direction to the rectangle. The result is a cross-shaped element with four equivalent energy minima as shown in Figure 2.1(b). Indeed, bi-axial anisotropy of such shapes has been explored earlier [76], although the dimensions were much larger. Four energy minima, as depicted

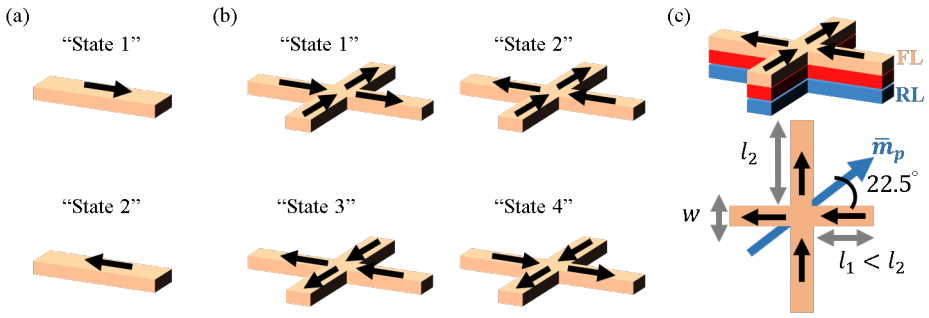

Figure 2.1: Multi-state magnetic memory based on a cross-shaped ferromagnet: (a) Equilibrium energy minima for a rectangular FM follow the long axis of the rectangle. (b) Four different magnetized states corresponding to four equilibrium energy minima of the cross-shaped FM. (c) Cross-shaped MTJ with the RL uniformly magnetized along an asymmetric angle of $22.5°$ that resolves four energy minima of the cross-shaped FL into four different resistance levels allowing storage of 2 bits within one memory cell (1 MTJ).

schematically in Figure 2.1(b), for such a nanoscale cross-shaped FM can be obtained from micromagnetic simulations [73]. The shape anisotropy of the branches and hence the barrier height between the minima are controlled by the aspect ratio (AR) of the branches. The multi-state MTJ structure is shown in Figure2.1(c) with the reference layer (RL) magnet assumed to be oriented at an angle of $22.5°$ with the short branch. The non-trivial magnetization direction of the RL magnet presumably could be achieved by engineering a synthetic-antiferromagnet (SAF) structure pinned by an antiferromagnet layer underneath. The asymmetry in the RL magnetization direction together with the asymmetry in the branch dimensions [$l_1 \neq l_2$ in Figure 2.1(c)] results in four well-separated resistance levels that could store 2 bits [77].

These two asymmetries (asymmetries in the branch dimensions and the direction of the RL magnetization) are also required to design a reliable STT-induced write process for the multi-state FM [73]. Table 2.1 summarizes the switching process of the multi-state bit studied in [73]. These switching current densities are, of course, for certain choices of material parameters and dimensions, but serve the purpose of illustrating the switching mechanism. Depending on the current pulse amplitude the bit could be switched from "State 1" to "State 2" or from "State 1" to "State 3". Switching to "State 4" from "State

Table 2.1: Switching of the cross-shaped FM with STT. The initial state in each case is "State 1". Pulse durations are not drawn to scale. For more details see [73].

Current density (A/cm^2)	Pulse shape	Final state
$J_0 < 0.25\times10^8$	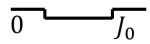	"State 1"
$0.25\times10^8 \leq J_{1\to2} \leq 1.75\times10^8$		"State 2"
$1.75\times10^8 < J_{1\to2,3} < 3.5\times10^8$	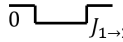	"State 2 or 3"
$J_{1\to3} \geq 3.5\times10^8$	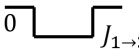	"State 3"
$J_{1\to3}$, followed by $-J_{1\to2}$	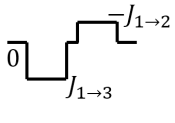	"State 4"

1" has to be via "State 3" and requires two opposite polarity pulses. In general, switching between any two arbitrary states could be realized using one or two pulses of appropriate polarities and amplitudes. Note that the current density required for switching is of the order of 10^8 A/cm^2. There also exists a certain range of current densities where the final state could be either "State 2" or "State 3". In this range the final magnetization state is picked randomly with increased current density [73]. Though the reason for such anomaly is not well understood, this random behavior seems to disappear with a different set of material parameters [78]. In the following section, normal modes of excitation of the cross-shaped FM is studied with a hope to illuminate the complex magnetization dynamics observed during switching.

2.2 Magnetic normal modes of the cross-shaped ferromagnet excited by STT

Spin-transfer-torque (STT) driven ferromagnetic resonance (ST-FMR) [79] and spin wave (SW) excitations [80, 81] in magnetic thin films and patterned magnets have been explored widely over the last decade due to both fundamental interest and potential

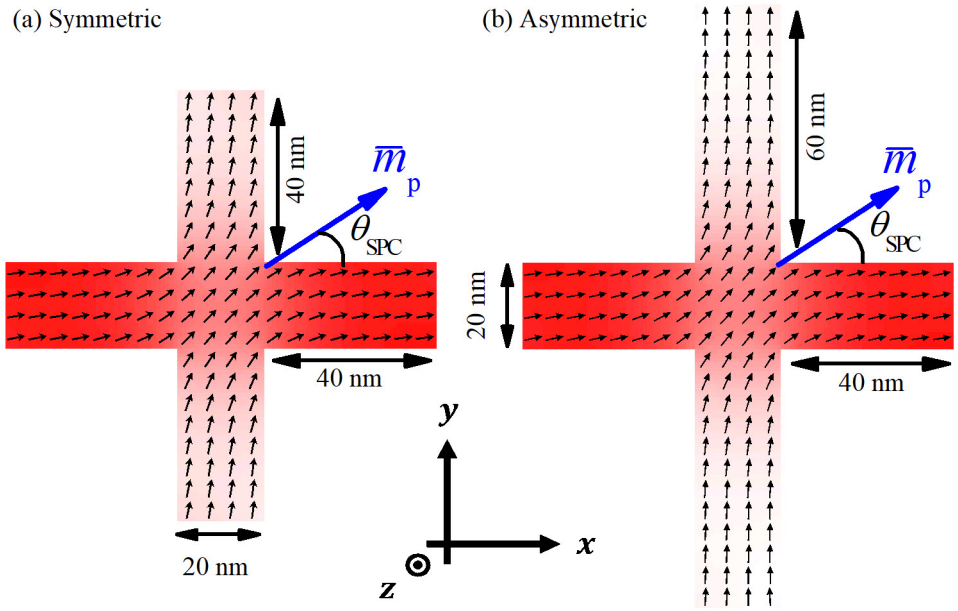

Figure 2.2: "State 1" magnetization distribution for two different geometries of cross-shaped FM: (a) Symmetric branches (b) Asymmetric branches. Direction of the RL magnetization $\vec{m}_p$ defines the spin-polarization direction θ_{SPC} of the current.

applications in spintronic devices [82–85]. Here, spin wave modes of the cross-shaped FM are calculated using the micromagnetic spectral mapping technique for different degree of asymmetry in the branch dimensions and the spin-polarization direction of the current.

All micromagnetic simulations have been done using OOMMF [41]. To separate out the effect of asymmetry in the branch dimensions from the effect of asymmetry in the direction of the spin polarized current (θ_{SPC}), two different structures have been simulated. These two configurations are shown in Figure 2.2 along with the lateral dimension of the structure and the axes convention. The thickness of the magnet is 2 nm in both cases. Then for each shape, two different θ_{SPC} values are considered: $\theta_{\mathrm{SPC}} = 45°$ (henceforth referred to as symmetric SPC) and $\theta_{\mathrm{SPC}} = 22.5°$ (henceforth referred to as asymmetric SPC). Only the free layer magnet is simulated assuming the fixed layer magnet to act only as a source of spin polarized current. The material parameters used are: saturation magnetization $M_{\mathrm{s}} = 1400 \times 10^3$ A/m, exchange constant $A_{\mathrm{ex}} = 30 \times 10^{-12}$

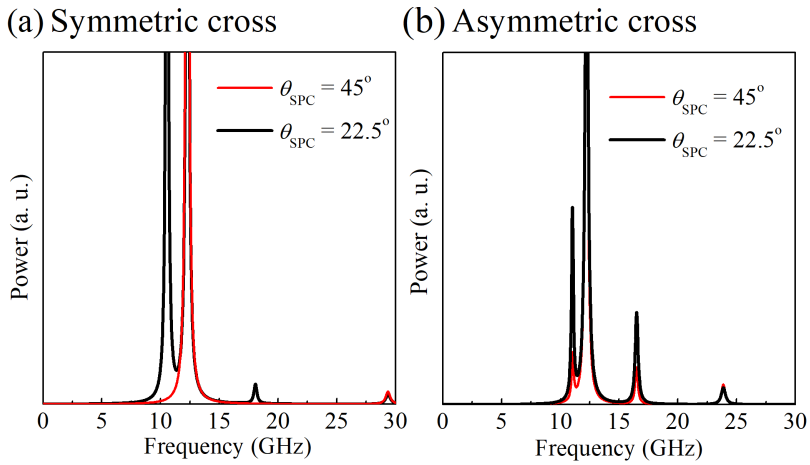

Figure 2.3: Power spectra obtained from the z-component of magnetization for (a) symmetric and (b) asymmetric cross-shaped FM with $\theta_{\mathrm{SPC}} = 45°$ and $\theta_{\mathrm{SPC}} = 22.5°$. Adapted from [74].

J/m, Gilbert damping constant $\alpha = 0.01$, spin polarization of the current $\eta = 0.4$. A cell size of 2 nm has been used for all three directions. Field-like-torque (FLT) is set to be 30% of STT [73,86]. Spin-wave modes are calculated employing techniques as described in [44]. Equilibrium magnetic configuration equivalent to "State 1" (as in Figure 2.2) is obtained first by energy minimization. Then a SPC pulse of given symmetry (θ_{SPC}) and current density of 10^7 A/cm^2 is applied on the equilibrium state at time $t = 0$ ns. The applied current strength is low enough (much lower than the switching currents noted in Table 2.1) such that only a small amplitude oscillation is induced. This magnetization dynamics is recorded up to 10 ns at a sampling interval of 5 ps allowing one to investigate frequencies up to 100 GHz with a resolution of 100 MHz. To obtain the frequency domain data, fast Fourier transom (FFT) is computed from the time domain variation of out-of-plane (z) component of magnetization for each discretized cell. The frequency spectra is then obtained by averaging the FFT power over all of the discretized cells in the magnetic domain. After identifying peaks from the spectra, spectral maps are obtained by plotting space varying FFT amplitude and phase for each frequency peak in the spectra.

Frequency spectra obtained for the above two cases are shown in Figure 2.3. For the symmetric cross (Figure 2.3(a)), two peaks at 12.3 GHz and 29.4 GHz are present for both $\theta_{\mathrm{SPC}} = 45°$ and $\theta_{\mathrm{SPC}} = 22.5°$, while two additional peaks at 10.6 GHz and 18.1 GHz

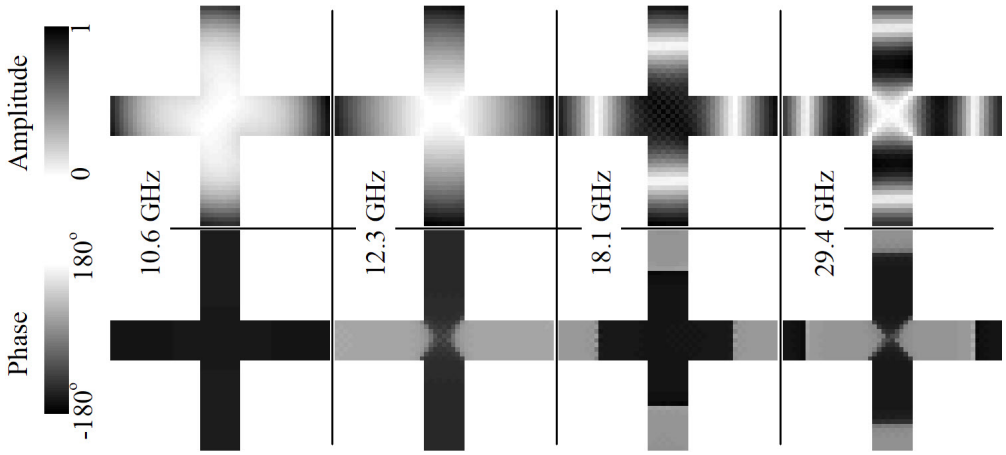

Figure 2.4: Spatial distribution of oscillation amplitude and phase in the symmetric cross-shaped FM corresponding to the peaks shown in Figure 2.3(a) for $\theta_{\mathrm{SPC}} = 22.5°$. All images follow the same color map shown on the left. Adapted from [74].

appears only for $\theta_{\mathrm{SPC}} = 22.5°$. Such dependence of the excited modes on the direction of SPC was also reported for an elliptic magnet [87]. Spatial maps of oscillation amplitude and phase corresponding to the peaks are shown in Figure 2.4. The peaks at 10.6 GHz could be identified as a quasi-uniform mode (although the precession amplitude is higher at the edges). The peak at 12.3 GHz also shows stronger oscillation at the branch edges similar to the 10.6 Hz modes. But the phase image shows that for this mode, precession at any two neighboring branches are in out-of-phase. The other two modes at 18.1 GHz and 29.4 GHz are found to be higher order standing wave like excitations.

Figure 2.3(b) shows the spectra for the asymmetric cross. For both $\theta_{\mathrm{SPC}} = 45°$ and $\theta_{\mathrm{SPC}} = 22.5°$ same set of modes are found. Spatial maps of oscillation amplitude and phase corresponding to the peaks are shown in Figure 2.5. The first two peaks at 11.0 GHz and 12.2 GHz show edge mode like spatial variation in the short and long branches, respectively. The mode at 12.2 GHz again shows out-of-phase precession at any two neighboring branches. The peaks at 16.5 GHz and 23.9 GHz shows standing wave like pattern in the branches. In the case of asymmetric cross changing the direction of polarization of SPC does not give rise to any additional modes. This is probably due to the dominance of shape anisotropy (over asymmetry of polarization direction of SPC) dictated by the asymmetry of dimensions of the short and the long branches.

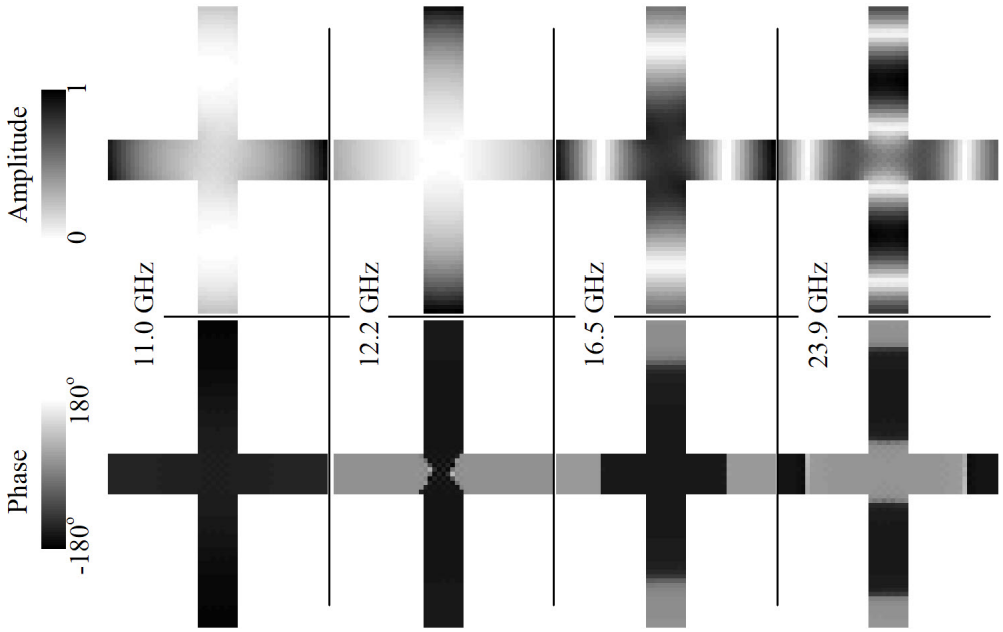

Figure 2.5: Spatial distribution of oscillation amplitude and phase in the asymmetric cross-shaped FM corresponding to the peaks shown in Figure 2.3(b) for $\theta_{\mathrm{SPC}} = 22.5°$. All images follow the same color map shown on the left. Adapted from [74].

As mentioned earlier, the cross-shaped FM could be considered as a ferromagnet having an effective bi-axial anisotropy created by two rectangles coupled at the center. It is interesting to compare the excited mode frequencies with that of rectangular FMs of similar dimensions. In absence of any external magnetic field, the uniform mode frequency f_{U} of a thin rectangular FM is given by the Kittel's formula [44],

$$f_{\mathrm{U}} = \frac{1}{2\pi}\gamma\mu_0 M_{\mathrm{s}}\sqrt{(N_{\mathrm{zz}} - N_{\mathrm{xx}})(N_{\mathrm{yy}} - N_{\mathrm{xx}})}, \tag{2.1}$$

where, gyromagnetic ratio $\gamma = 1.76 \times 10^{11}$ rad/T·s, vacuum permeability $\mu_0 = 4\pi \times 10^{-7}$ V·s/A·m and N_{xx}, N_{yy}, N_{zz} are the diagonal elements of the demagnetizing tensor for a rectangle with the long side along the x direction and the short side along the y direction. Saturation magnetization $M_{\mathrm{s}} = 1400 \times 10^3$ A/m is used. The demagnetizing factors are estimated from Aharoni's formula [43]. The uniform mode frequencies calculated using Equation 2.1 for different aspect ratio rectangles are listed in Table 2.2. As evident, the uniform mode frequencies of rectangles with dimensions equal to the branches of the cross-shaped FM are quite close to the first two peaks obtained in Figure 2.3(a)-(b).

Table 2.2: Uniform mode frequencies from Kittel's formula.

Length (nm)	Width (nm)	Thickness (nm)	Frequency (GHz)
40	20	2	10.3
60	20	2	12.3
100	20	2	13.8
140	20	1.8	14.5

Note that, for the cross-shaped FM, the precession in the branches are localized at the edges and rather non-uniform, presumably due to the non-uniformity of the effective field originating from the 45° domain wall at the center of the cross. Also, the frequency of the rectangles with length equal to the lateral (or vertical) extent of the cross-shaped FM, are much higher than the quasi-uniform mode frequencies observed in Figure 2.3(a)-(b). This is expected as the center creates a coupling among the branches giving rise to an effective biaxial anisotropy, while weakening the shape anisotropy of the constituent rectangles themselves.

The confinement in the branches is decided by the non-uniform internal magnetic field and could be studied further following methods similar to the ones in [84, 88]. Nevertheless, the above results indicate that the asymmetry of the cross dimensions has a stronger effect on the excited spin wave modes than the direction of spin-polarization of the current. This could be a reason of why an asymmetric cross-shaped structure is necessary together with the asymmetry of the RL to better resolve the switching current densities from "State 1" to "State 2" and "State 1" to "State 3" [73].

2.3 Voltage controlled switching of the cross-shaped ferromagnet

STT-based write scheme for the cross-shaped FM requires a large write current. The issue becomes worse when we need well separated current levels targeting specific final states. Higher current levels (compared to the critical current of a single bit device) would also require an increased area of the drive transistor, i.e., this multi-level cell enables two bit/cell storage, albeit with an increased transistor size. As a result the storage

density does not increase much (if not reduced) even with this multi-state cell. In the following section, we attempt to address this issue with a low power voltage controlled switching method for the cross-shaped ferromagnet.

2.3.1 Voltage controlled magnetic anisotropy

Recently voltage control of magnetism has become a very active area of research due to fundamental interest and due to the possibility of manipulating magnetism at the nanoscale in a more energy efficient manner by applying electric fields instead of currents [89]. Voltage controlled magnetic anisotropy (VCMA) is one these options that has recently gained a lot of interest as this could be observed at CoFe/MgO interfaces that is also the material of choice for conventional STTRAM [40]. Perpendicular magnetic anisotropy (PMA) at the interface of MgO with Fe-based alloys is also used in perpendicular STTRAM bit [40, 90, 91]. Once the thickness of the FM is reduced below a critical limit, this anisotropy could win over the out-of-plane demagnetizing field of a ferromagnetic thin film. Below this critical thickness the magnetization prefers to align along the out-of-plane (normal to the plane of the thin film) direction. This anisotropy energy has been shown to be dependent on the electric field across the interface [84, 92–102] and the effect has been termed as voltage controlled magnetic anisotropy (VCMA). VCMA may assist STT-induced switching, resulting in a significant reduction of the STT-switching current density [96, 98, 99]. Alternatively, VCMA-induced precessional motion may be used to achieve switching, without the need for STT. The latter approach of precessional switching offers a highly efficient write process offering ultra-low write energy compared to the STT-based write process. This option has already been explored theoretically [101] and demonstrated experimentally [95, 100] in patterned FMs of rectangular, elliptic and circular shapes.

Figure 2.6(a) shows a typical arrangement for VCMA-based precessional switching of FL in an in-plane MTJ structure. For an MTJ, as the electric field direction is opposite at the two FM/MgO interfaces, PMA energy density will be reduced at one interface and increased at the other interface. During switching the electric field is applied to increase the PMA energy of the FL (i.e., PMA energy of the RL is reduced under the

same electric field, which has no effect on the already in-plane RL magnet). The variation of the anisotropy energy K_{u1} with the applied electric field F has been shown to be,

$$K_{\mathrm{u1}} = \frac{1}{t_{\mathrm{FL}}}[K_{\mathrm{t}} - \zeta F], \tag{2.2}$$

where, ζ is the VCMA coefficient (change of interface anisotropy energy in J/m^2 per unit of applied electric field in V/m) and t_{FL} is the thickness of the FL, K_{t} is the anisotropy energy per unit interface area. The thickness term t_{FL} in the denominator indicates the interfacial nature of the anisotropy as well as the VCMA effect. Figure 2.6(b-d) explain the VCMA-based switching process for an in-plane FL with equilibrium ($F = 0$) energy minima along the x-axis. The voltage is turned on at time $t = 0$ ns. With the energy minima now along the z-axis, the FL magnet begins to precess around this new effective field. If the voltage is left turned ON, as in Figure 2.6(b), the magnetization finally aligns itself toward the $+z$ direction. If the voltage is turned OFF after the half-precession cycle (~ 0.7 ns, Figure 2.6(c)) or after the full precession cycle (~ 1.3 ns, Figure 2.6(d)), the FL gets damped to the nearest energy minima (along the x direction). Hence, by controlling the voltage pulse width the bit can be switched from one state to the other. As there is no STT required in this process, by optimizing the MgO thickness (to reduce the current flow due to the applied electric field), essentially a completely voltage-controlled write process can be designed.

Note that after the application of the voltage pulse, the magnet could choose either the $+z$ or the $-z$ direction (they are equivalent in terms of energy) depending on the initial value of the out-of-plane component of the magnetization at $t = 0$ [103]. The precession direction would be opposite for these two cases. As this small out-of-plane component of magnetization at $t = 0$ would be randomly decided by the thermal fluctuations, there is hardly any control on the precession direction. For this single bit device, the precession direction does not affect the final state (turning OFF the pulse at ~ 0.7 ns will toggle the state). However, the direction of precession becomes important for the cross-shaped FM based multi-state bit. As discussed in the following section, a small out-of-plane magnetic field would be necessary to break the symmetry of the out-of-plane directions and ensure same direction of rotation each time a pulse is applied.

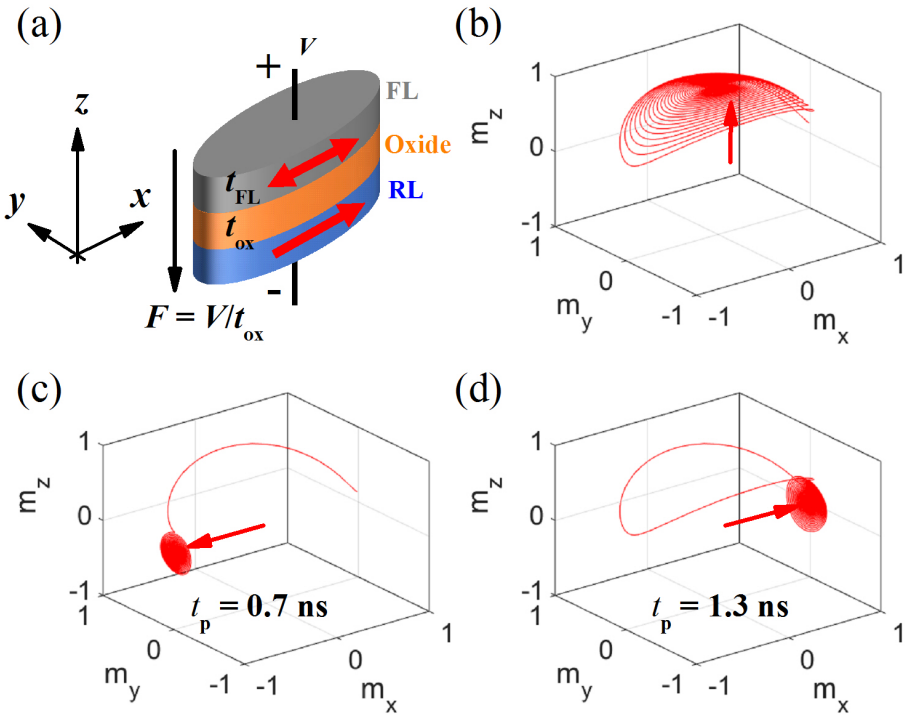

Figure 2.6: VCMA-based precessional switching explained using macrospin simulations of an in-plane FL magnet. (a) In-plane MTJ with the FL thickness optimized to obtain substantially large PMA, while retaining in-plane orientation at equilibrium. Axes definitions and polarity of positive bias is also shown. (b) Precessional magnetization trajectory taken by the FL magnet under applied bias voltage. (c) A 0.7 ns long voltage pulse switches the FL from $+x$ to $-x$ direction. (d) A 1.3 ns long pulse returns the FL to the initial $+x$ direction.

As explained in section 2.1, four equilibrium magnetization states of a cross-shaped FM arise out of the shape induced anisotropy. The logic state associated with the equilibrium magnetization states are determined by the in-plane magnetization components guided by the shape of the magnet. Materials with strong PMA are not suitable for such a device, as PMA favors out-of-plane magnetization irrespective of the shape. However, by choosing appropriate dimensions and thickness of a cross-shaped FM with significant interfacial PMA, it is possible to switch the magnetization between the equilibrium magnetization states using VCMA-based precessional motion, while the in-plane component of the magnetization provides multi-state functionality as before [75].

2.3.2 Switching cross-shaped ferromagnet using VCMA

2.3.2.1 Simulation details

Again, OOMMF [41] simulations are used to obtain the equilibrium magnetization states and magnetization dynamics of the cross-shaped FM. Following previous reports [95, 101, 104], the interfacial PMA is included as a uniaxial anisotropy field in the effective field term in Landau-Lifshitz-Gilbert (LLG) equation. For all the simulations, a cell size of 1 nm is used in the x and y directions (axes definitions are shown in Figure 2.7). The cell size in the out-of-plane (z) direction is set equal to the thickness of the cross-shaped FM. Material parameters used are: saturation magnetization $M_{\rm s} = 1150$ kA/m, damping constant $\alpha = 0.01$, exchange constant $A = 30$ pJ/m, interfacial perpendicular anisotropy $K_{\rm t} = 1.3$ mJ/m^2, which are typical for CoFeB alloys [40, 96, 105]. The interfacial PMA is assumed to change linearly with the applied electric field as per Equation 2.2, with a coefficient of electric field control of magnetic anisotropy ζ. The reported (experimental and theoretical) values of the coefficient ζ varies from 30 μJ/m^2 per 1 V/nm of electric field to 100 μJ/m^2 per 1 V/nm of electric field [92–97, 106]. We assumed $\zeta = 50$ μJ/m^2 per 1 V/nm for all the simulations. We define the positive bias voltage with polarity as shown in Figure 2.7 (inset). Hence, with a positive bias voltage the electric field points from the FL magnet towards the MgO layer at the FM-MgO interface, increasing the interfacial PMA of the FL, consistent with experimental reports [96, 97, 100]. The reported values of the breakdown electric field for an MgO tunnel barrier varies from 0.8 V/nm to 2.4 V/nm [107–109]. A bias voltage of 1.5 V and MgO tunnel barrier thickness of 1 nm are used for all the simulations. The resulting electric field of 1.5 V/nm is within the breakdown voltage range given above. Effect of STT (resulting from the leakage current flow through the MgO tunnel barrier under an applied voltage) has been neglected because the leakage current is expected to be much smaller than the current required to produce significant STT. Higher order anisotropy terms and finite temperature effects have not been considered. The rise and fall times of the voltage pulses are taken to be zero.

Previously in section 2.1 and 2.2, a cross-shaped FM with branches of rectangular shape was considered following the previous study [73]. However, VCMA-induced

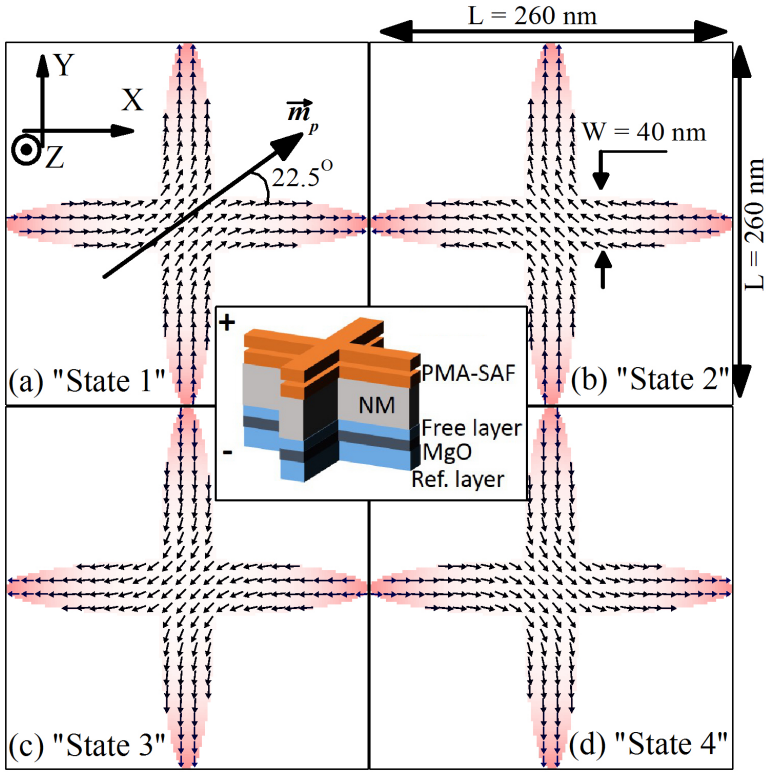

Figure 2.7: Four equilibrium magnetization states of the cross-shaped FM with branches of elliptic shape: (a) “State 1”; (b)“State 2”; (c)“State 3”; (d) “State 4”. Red to white color variation signifies highest to zero out-of-plane magnetization. Axes definitions and RL direction ($\vec{m}_{\mathrm{p}}$) are shown in (a). Dimensions are shown in (b). The inset shows the proposed design of the cross-shaped MTJ stack and the PMA-SAF stack for generating a small internal magnetic field. The thick non-magnetic metal (NM) separates the two stacks. The polarity for positive bias is also shown in the inset. This figure has been reproduced from [75].

dynamics of such a cross-shaped FM involves domain wall like excitations and rather chaotic precession. A cross-shaped FM with elliptical branches is found to be more suited for VCMA-based switching. As shown in Figure 2.7, the modified cross-shaped FM can be considered as two ellipses with major axes perpendicular to each other. For each of the two ellipses, the minor axis is 40 nm long and the major axis is 260 nm long. The length of the minor axis of the ellipses within the cross-shaped FM is defined as width W, and length of the major axis is defined as length L of the cross-shaped FM (see Figure 2.7). The aspect ratio AR of the cross-shaped FM is then defined as L/W.

Keeping the lateral dimensions the same, the thickness of the cross-shaped FM is tuned in such a way that the magnetization of the branches tends to remain in-plane in equilibrium with some out-of-plane component at the end of the branches (as shown in Figure 2.7). The out-of-plane component of the magnetization at the end of the branches can be positive (in +z) or negative (in -z), which gives rise to four more states in addition to the four states shown in Figure 2.7 (States shown in Figure 2.7 have positive out-of-plane components). During or after switching using a voltage pulse, the magnetization can settle down at an energy minima with negative out-of-plane component of the magnetization. To eliminate this latter possibility here, a small external magnetic field of 20 Oe towards the +z direction is assumed to be present, making the four states with positive out-of-plane magnetization energetically more favorable. This small uniform bias magnetic field can be generated internally using an additional PMA synthetic antiferromagnet (SAF) stack [110, 111] placed at an appropriate distance from the MTJ stack and separated by a thick non-magnetic metal layer (see Figure 2.7 inset). This small out-of-plane field also contributes to the canted magnetization of the branches in equilibrium. To obtain the initial equilibrium states shown in Figure 2.7, the magnetization is first saturated by an applied field towards a direction close to one of the equilibrium states, and then it is allowed to relax while the applied field (except the small fixed out-of-plane field mentioned int the previous section) is removed.

Similar to the cross-shaped FM in [73], the modified cross-shaped FM has four equilibrium magnetization configurations. These four equilibrium magnetization states have four different resistance values when the cross-shaped FM is used as the FL in a MTJ structure with the RL pointed at an asymmetric angle (e.g., 22.5°) with respect to the x-axis, as shown in Figure 2.7(a). Note that, the branch dimensions are same as opposed to the structure studied in [73]. So the RL orientation may require additional adjustments to design four well resolved resistance states corresponding to the four states shown in figure 2.7 [77]. Adjusting the RL orientation does not affect the VCMA-based precessional switching as the STT term is negligible.

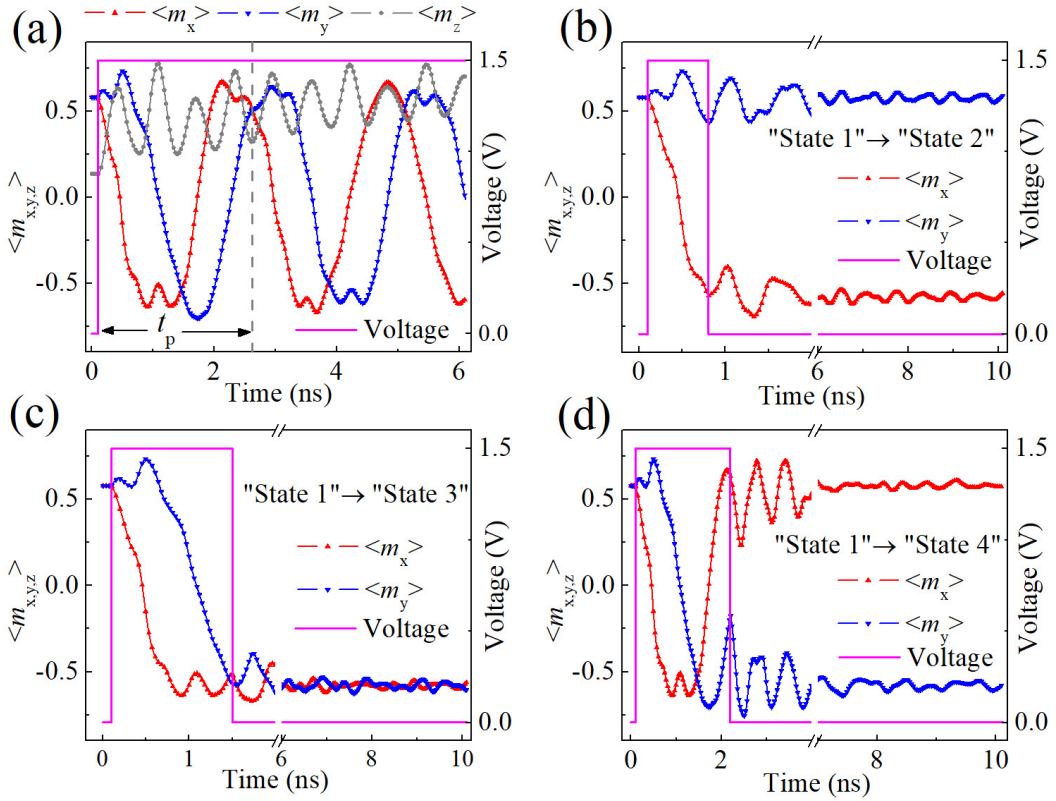

Figure 2.8: VCMA-induced magnetization dynamics due to an applied voltage starting at "State 1": (a) in presence of the voltage magnetization rotates towards the out-of-plane direction; (b) switching to "State 2" with a voltage pulse width of 0.7 ns; (c) switching to "State 3" with a voltage pulse width of 1.4 ns; (d) switching to "State 4" with a voltage pulse width of 2.1 ns. The symbols $\langle m_x \rangle$, $\langle m_y \rangle$ and $\langle m_z \rangle$ denote spatially averaged x, y and z components of the magnetization respectively. Approximate time period of rotation of magnetization t_{p} is marked in (a). This figure has been adapted from [75].

2.3.2.2 VCMA-induced dynamics and switching

To study the VCMA-induced dynamics, a voltage pulse is applied, taking one of the equilibrium magnetization states as the initial magnetization (e.g., "State 1" in Figure 2.8). When a positive voltage pulse is applied, the PMA of the FL is increased. The magnetization of the branches start to precess around the new effective field direction, which points towards a more out-of-plane direction. The precession direction is anti-clockwise (clockwise) for a positive (negative) out-of-plane component of initial magnetization, which is why control of the out-of-plane component as discussed before is

important. As a result of this precession, magnetization configuration traverses the states in the order "State 1"→"State 2"→"State 3"→"State 4"→"State 1", starting from any of the equilibrium states. This precessional motion is shown in Figure 2.8(a) in terms of spatially averaged x, y and z components of the magnetization. If the voltage is turned off after different time durations, the magnetization of the branches are damped to the nearest energy minima, switching the FM to different equilibrium magnetization states. With a voltage pulse duration of 0.7 ns, 1.4 ns and 2.1 ns, "State 1" can be switched to "State 2", "State 3" and "State 4", as shown in Figure 2.8(b), (c) and (d) respectively. Similarly, starting with "State 2", a voltage pulse duration of 0.7 ns, 1.4 ns and 2.1 ns will result in "State 3", "State 4" and "State 1" respectively. Hence starting with any state, other states can be reached by a voltage pulse of appropriate duration. These pulse duration are of the same order of magnitude as reported for rectangular or elliptic bits [95, 100, 101]. Precession of magnetization of the cross-shaped FM as shown in Figure 2.8(a) is not perfectly periodic. The time period of rotation $t_{\rm p}$, as marked in Figure 2.8(a), is the time taken by the spatially averaged magnetization to come back to the initial magnetization.

VCMA-induced precessional switching in elliptic [101], rectangular [95] or circular [100] nanomagnets is conceptually similar to precessional magnetization switching using short magnetic field pulses [103, 112]. Duration of voltage pulse (field pulse) and critical voltage (field) for switching can be calculated for elliptic, rectangular or circular nanomagnets within the macrospin approximation [103]. But it is difficult to approximate the cross-shaped FM as a macrospin and, thus, a simple analytical approach to calculate $t_{\rm p}$ might not be possible. Therefore micromagnetic simulations are used to calculate $t_{\rm p}$ and voltage pulse durations required for switching to different states.

Neglecting the power dissipation due to leakage current flow through the MgO tunnel barrier, the energy consumed per write operation can be estimated by the charging energy of the parallel plate capacitor formed by the MTJ [95]. Considering a dielectric constant of $\sim$10 for MgO, write energy per write operation is approximately $\sim$1.5 fJ for the assumed dimension of the cross-shaped FM. This energy is much less than the energy required for STT-induced switching ($\sim$0.1-10 pJ) [5, 9, 113]. Considering a leakage current of $\sim 10^4$ A/cm^2 [96] for example, and a maximum pulse duration of 2.1 ns

(switching from "State 1" to "State 4"), the energy wasted by the leakage current is about ∼5 fJ, which is more than the energy required for VCMA-induced switching. Therefore it is important to reduce the leakage current as much as possible to reduce the power consumption in such a device.

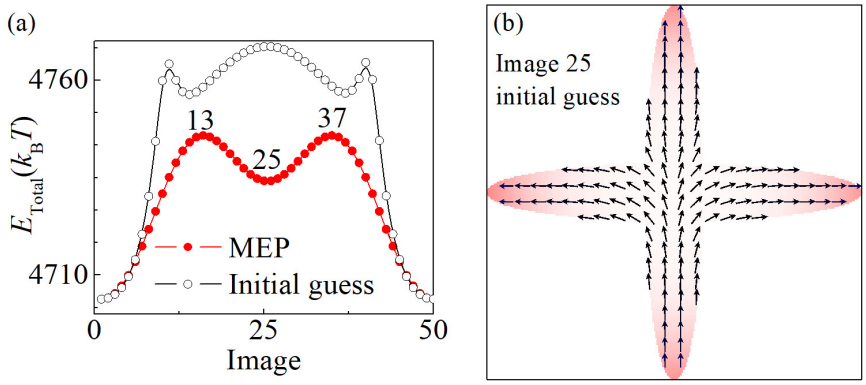

Figure 2.9: Reversal of the cross-shaped FM from "State 1" to "State 2" following the MEP as obtained using the string method: (a) Energy of the initial guess path and the MEP with 50 images. (b) Initial guess of Image 25. This figure has been adapted from [75].

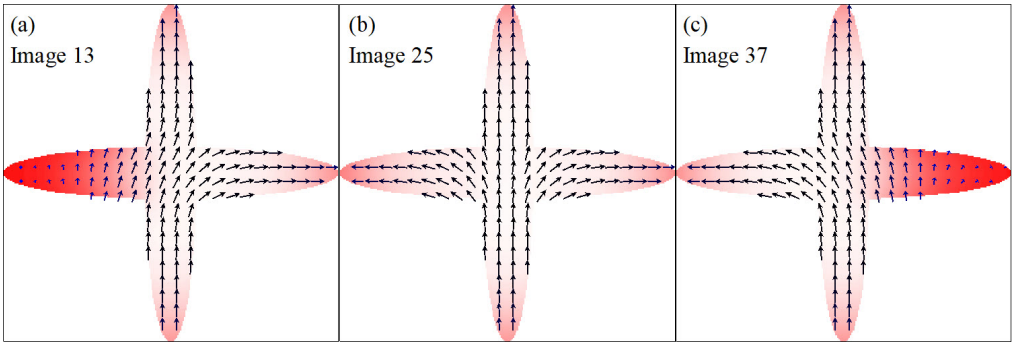

Figure 2.10: Magnetization configurations of selected images on the MEP shown in Figure 2.9: (a) Image 13, (b) Image 25 and (c) Image 37. This figure has been adapted from [75].

2.4 Thermal stability of the cross-shaped ferromagnet

As discussed in Chapter 1, to ensure the retention of the stored information in a magnetic memory, the energy barrier isolating the energy minima should be high enough ($\sim 40 - 60$ times for 10 years of retention) compared to the thermal energy $k_{\text{B}}T$ (k_{B} is

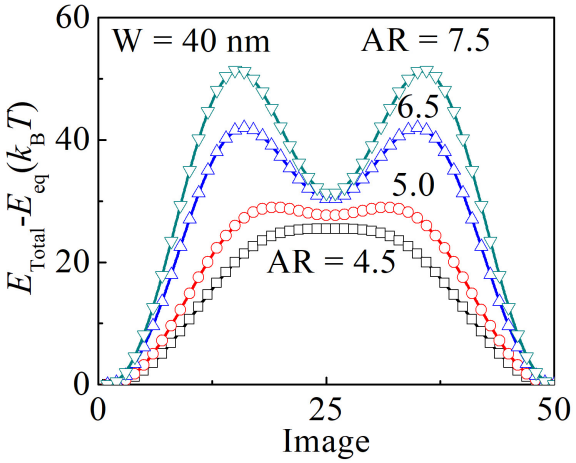

Figure 2.11: MEP for switching from "State 1" to "State 2" for different aspect ratios AR of the cross-shaped FM obtained using the string method. E_{eq} is the total energy of "State 1" (or "State 2"). With increasing AR, the energy maximum at Image 25 turns into a energy minimum. This figure has been adapted from [75].

the Boltzmann constant, $T = 300$ K). For the case of the cross-shaped FM, the minimum energy barrier between any two equilibrium states will decide the thermal stability Δ of this multi-state memory. To estimate Δ for an elliptic/rectangular FM, analytical formulae noted in Section 1.2.1 often can be used reasonably [11]. However, due to the complex micromagnetic nature of the energy landscape of a cross-shaped FM, such analytical equations cannot be used. Even for nanomagnets with basic shapes (such as ellipse or rectangle) magnetization switching might occur through nucleation and propagation of domain walls [11, 114]. For such cases, where the magnetization switching along the minimum energy path (MEP) could not be approximated as coherent rotation, the nudged elastic band (NEB) method [115] and the string method [114, 116, 117] were applied to estimate the MEP between equilibrium states of the FM. However, to employ the NEB technique one needs to determine the effective magnetic field along the direction perpendicular to the guess path (or so-called "string"). The string method is a modified version of the NEB technique, where this step is avoided by using a re-normalization technique. This process allows one to use a micromagnetic solver (e.g., OOMMF) to calculate the effective field and take the subsequent time-integration. For this reason, the string method is employed here to estimate the MEP between the equilibrium magnetization states of

the cross-shaped FM. The height of the MEP then determines the thermal stability Δ of the memory bit.

The details of the implementation of the string method employing OOMMF can be found elsewhere [114, 116, 118]. Our code has also been benchmarked for a simple PMA magnet against previously reported results (Figure 1 of [114]). The thermal stability is determined by the energy required to switch the cross-shaped FM from one state to another state, which involves flipping of only one of the two intersecting ellipses along an MEP. So we assumed an initial guess path with 50 images with "State 1" and "State 2" as the 1^{st} and the 50^{th} images, respectively. To guide the initial guess path towards the MEP with a reasonable number of iterations, we consider another image (the 25^{th} image) on the initial guess path. The 25^{th} image is created such that the two horizontal branches (branches along the x direction) magnetized opposite to each other [see Figure 2.9(b)]. With these three images, considering equal arc-length discretization [116, 118] of the MEP, an initial guess path with 50 images is generated by spline interpolation. We have verified that increasing the number of images to 100 does not change the resulting MEP. Each of the 48 images (i.e., except Image 1 and Image 50, which are held fixed) is then allowed to relax for 10 ps using OOMMF with a damping constant of 1 and without the precession term in the LLG equation [116]. After each iteration, to maintain equal distance between the images on the path, the resulting images are again interpolated on the string using spline interpolation [118]. The relaxation and interpolation steps are repeated until the total micromagnetic energy of each image does not change significantly (more than 0.5 $k_{\mathrm{B}}T$) between consecutive iterations.

For the cross-shaped FM with dimensions as shown in Figure 2.7, the energies of the initial guess path and the final MEP are plotted in Figure 2.9(a). The total energy (E_{Total}) for each image includes the magnetostatic, the exchange, the uniaxial anisotropy (due to the PMA) and the Zeeman energies (due to the small fixed perpendicular magnetic field). From the final converged MEP (Figure 2.9(a)), it can be noted that the switching from "State 1" to "State 2" along the MEP occurs via two energy maxima (at Image 13 and Image 37) and an energy minimum (at Image 25). Magnetization distributions for Image 13, Image 25 and Image 37 on the MEP are shown in Figure 2.10(a)-(c). The

barrier height for thermal flipping is decided by the energy required to switch "State 1" ("State 2") over the energy maxima at Image 13 (Image 37), taking the cross-shaped FM to the energy minima at Image 25. Image 13 and Image 37 show the horizontal branches flipping along the MEP following a path that is partially out-of-plane, which is expected because of the presence of a perpendicular anisotropy field. The thermal stability factor, Δ, as decided by the barrier height is approximately 41, which provides sufficient retention time for non-volatile operation [46]. The energy of Image 25 on the MEP depends on the aspect ratio AR of the cross-shaped FM as shown in Figure 2.11. The energy minimum at Image 25 on the MEP gradually becomes an energy maximum with decreasing aspect ratio.

Table 2.3: Thermal stability factor Δ and time period of rotation t_{p} for different dimensions of the cross-shaped FM. This table has been reproduced from [75].

W (nm)	*AR* (*L*/*W*)	t_{FL} (nm)	Thermal stability factor Δ	Time period of rotation t_{p} (ns)
25	6.0	1.9	23	1.8
25	7.0	1.9	26	2.2
35	6.0	1.8	27	1.8
35	7.0	1.8	33	2.1
40	4.5	1.8	25	1.9
40	5.0	1.8	29	2.0
40	5.5	1.8	33	2.2
40	6.5	1.8	42	2.6
40	7.5	1.8	51	3.1

2.5 Effect of dimension on the VCMA-induced switching and thermal stability

The dependence of t_{p} and Δ on the dimensions of the cross-shaped FM are summarized in Table 2.3. Material parameters, MgO barrier thickness and applied voltage pulse amplitude are kept same as the ones noted in section 2.3.2.1. As evident from Equation 2.2, if the thickness t_{FL} is increased, while keeping W and AR the same, the equilibrium magnetization becomes increasingly in-plane because the PMA energy per

unit volume K_{u1} is reduced. Eventually, the electric field F required to switch such a cross-shaped FM exceeds the breakdown field of the MgO tunnel barrier. This sets the upper limit of t_{FL} for a given set of W and AR. On the other hand, if t_{FL} is lower than a critical value then the PMA overcomes the shape anisotropy and the equilibrium magnetization becomes predominantly out-of-plane. To make the cross-shaped FM work as a multi-state memory switchable by voltage, the thickness must be tuned close to a value so that the out-of-plane demagnetizing field is comparable to and somewhat compensated by the interfacial perpendicular anisotropy field [98]. If the AR is lowered, keeping t_{FL} and W the same, Δ is reduced, which is similar to the scaling of Δ for an elliptic bit as a function of the aspect ratio [119]. Too low an AR results in small shape anisotropy and predominantly out-of-plane equilibrium magnetization. Increasing the AR increases t_{p} as well as Δ. From Table 2.3 it is evident that $\Delta \geq 40$ could be achieved for cross-shaped FMs with W = 40 nm and an AR over 6.5. Efficient patterning techniques would be required to make such large aspect ratio shapes. Designing a layout with efficient placement of the cross-shaped bits would be important to maximize the information storage density.

2.6 Summary

In summary, we have shown that a cross-shaped FM switched using VCMA could provide a low-power non-volatile random access memory, where two bits can be stored in each memory cell using four equilibrium magnetization states. Compared to the previously studied STT-based switching process, a voltage controlled switching mechanism allows for much lowered write energy per write operation. The energy barrier height between the equilibrium energy valleys of the cross-shaped FM has been estimated using the string method. For certain minimum dimensions of the cross-shaped FM, this barrier height is sufficient to ensure the thermal stability of the memory bits. However, the switching relies on shape anisotropy, and it has been shown that the dimensions of the cross-shaped FM are critically important for the switching to be viable while maintaining the thermal stability and multi-state functionality. For the latter reason, despite being able

to store two bits, the structure may not provide enhanced storage density as compared to two analogous single-bit devices.

Chapter 3

Perpendicular magnetic anisotropy and magnetization reversal in epitaxial chromium telluride thin films

Although, lithographically patterned magnets of nanoscale dimensions are required for nanoscale device applications, study of magnetic thin films prior to their patterning is equally important. New materials will be required in near future if magnetic devices are to retain their properties when the device dimensions are scaled down. By studying the magnetic properties and magnetization reversal processes in a thin film, one estimates the material properties, identifies optimum growth recipes to tailor specific properties and determines any unexpected modification of material properties during the subsequent patterning steps. In this chapter, magnetic properties and magnetization reversal mechanisms in thin films with strong perpendicular magnetic anisotropy (PMA) will be investigated.

Ultra-high density, low-cost and efficient storage [120] and non-volatile memory devices [40, 121] are required to fulfill the increasing demand for data storage and data-intensive computing. As stated in Chapter 1, PMA magnets offer more efficient operation of STTRAM. Interestingly, for hard disk drives (HDD), which store information as the magnetization of the individual domains on a magnetic thin film media, high anisotropy

The results reported in this chapter have been published in the journal article titled "Angular dependence of magnetization reversal in epitaxial chromium telluride thin films with perpendicular magnetic anisotropy" by T. Pramanik, A. Roy, R. Dey, A. Rai, S. Guchhait, HCP Movva, C-C. Hsieh, S. K. Banerjee in Journal of Magnetism and Magnetic Materials, vol. 437, pages 72-77, 2017. Contributions: Samples were grown by A. Roy. A. Roy carried out the material characterization. T. Pramanik and S. Guchhait conducted the magnetic measurements. R. Dey and S. Guchhait conducted the transport measurements. T. Pramanik carried out the simulations with help from A. Roy and R. Dey. A. Roy, T. Pramanik and R. Dey wrote the manuscript and are the corresponding authors of this publication. S. K. Banerjee supervised the work. All authors reviewed and commented on the results and the manuscript.

perpendicular media (with out-of-plane remanent magnetization) offers increased bit storage density when compared to longitudinal media (with in-plane remanent magnetization). The retention time of the stored information in such perpendicular thin film media depends on the ratio of the anisotropy energy to the thermal energy, $K_{\mathrm{u1}}V/k_{\mathrm{B}}T$, where K_{u1} is the PMA energy per unit volume, and V is the effective volume of the bit in the media [120]. Materials with high PMA energy are thus desired to increase the memory density.

3.1 Magnetic anisotropy of chromium telluride thin films

3.1.1 Growth and material characterization

A number of choices for PMA thin films are already well known [39, 121]. Magnetic properties and magnetization reversal processes in these thin films are also well established. Chromium telluride ($Cr_{1-\delta}Te$) material systems have been known for a long time due to their complex and interesting magnetic properties. Early studies have focused on the crystal structure and magnetic moments of different phases in bulk form [122–125], while recent studies have focused more on thin films suitable for device applications, e.g., intrinsic exchange bias [126], possibility of half-metallic ferromagnetism [127], and electric field modulation of ferromagnetism [128]. In this chapter, we focus on the magnetic anisotropy and magnetization reversal properties of epitaxial Cr_2Te_3 thin films.

Different stable stoichiometries of chromium telluride ($Cr_{1-\delta}Te$) material system have metal deficient crystal structures, depending on the value of δ, and are ferromagnetic metals with a Curie temperature varying from 180 K to 340 K [129]. The thin films used in this study were grown in a molecular beam epitaxy (MBE) chamber under ultra-high vacuum (UHV) conditions [130, 131]. Details of the growth and characterization systems and growth techniques have been described elsewhere [132, 133]. A reflection high energy electron diffraction (RHEED) setup attached to the MBE system have been used for *in situ* monitoring of surface reconstruction and growth. RHEED patterns captured during the growth indicated hexagonal structure and high crystalline quality of the grown thin films. Hexagonal crystal structure and growth along the along (001) direc-

tion (*c*-axis) were also confirmed by X-ray diffraction measurements. The elemental compositions of the grown films were investigated using an *in situ* X-ray photoelectron spectroscopy (XPS). *In situ* scanning tunneling microscopy (STM) study of the surface of Cr_2Te_3 thin film grown on Si(111)-(7×7) surfaces revealed characteristically triangular shaped structures. Careful investigation also reveals that the islands are truncated triangular, or, more precisely truncated hexagonal, with sharp edges or partially rounded edges in shape [130, 131]. The growth structurally agrees very well with other reports of the growth of a thin film following hexagonal structure due to substrate crystal symmetry of a hcp(0001) and fcc(111) [132, 134–137]. Magnetic and transport measurements were carried out with 9 T Quantum Design physical property measurement system (PPMS) equipped with a vibrating sample magnetometry (VSM) option, capable of cooling samples down to 2 K.

3.1.2 Magnetic property measurements

Magnetic and magneto-transport measurements carried out on Cr_2Te_3 thin films confirmed a ferromagnetic Curie temperature (T_c) of $\sim$ 180 K [131]. Figure 3.1(a) and (b) show the in-plane and out-of-plane hysteresis loops, respectively, of a 20 nm thick film at 2 K. The square shape of the out-of-plane hysteresis loop with a coercive field much smaller than the in-plane saturation field indicates presence of strong PMA along the *c*-axis.

From this basic measurement a number of material parameters can be estimated. First, the saturation magnetization of $M_{\rm s} = 620\times10^3$ A/m is estimated from the measured moment at saturation and the thin film volume. Then, the anisotropy energy coefficients are also extracted using the the method proposed by Sucksmith and Thompson [138]. This method relies on the fact that, the hard axis (in-plane directions) magnetization remains quasi-coherent even for an extended thin film. Hysteresis in the in-plane magnetization curve near zero field due to formation of multi-domain states may affect the estimation of anisotropy coefficients by the above technique which assumes coherent rotation. However, as suggested in [139], anisotropy coefficients should be estimated from the fit to the non-hysteretic part of the magnetization curve. Thus, we have excluded the field range

where the hysteresis occurs and fit only the data obtained at fields where there is no identifiable hysteresis (shown in the inset of Figure 3.1(a)). Data points at very high fields, which mark the onset of saturation have been excluded from the fitting as well. As the coherent rotation mechanism is valid in the selected range of magnetic field, the Sucksmith-Thomson method should yield a reliable estimation of the anisotropy coefficients. The first and second order anisotropy coefficients extracted from the fit are $K_{u1} = 8.71 \times 10^5$ J/m^3 and $K_{u2} = 2.85 \times 10^5$ J/m^3, respectively. This yields a ratio of $K_{u2}/K_{u1} = 0.33$ and a hard axis saturation field of $H_{sat} = 3.8$ T. The fitted in-plane magnetization curve, also shown in Figure 3.1(a), agrees well with the experimental data. Previously, a strong second order uniaxial anisotropy with $\mid K_{u2}/K_{u1} \mid \approx 1$ at 296 K was reported in CrTe [125]. Comparable values of cubic anisotropy and uniaxial anisotropy coefficients were also reported for CrTe with zinc-blende structure [140]. The ratio K_{u2}/K_{u1} in our thin film is similar to the value for bulk cobalt ($K_{u2}/K_{u1} \approx 0.28$) [141] and Co/Pt thin films ($K_{u2}/K_{u1} \approx$ 0.3-0.4) [142], but much higher than values observed in Ta/CoFeB/MgO material systems ($K_{u2}/K_{u1} <$ 0.1) [143].

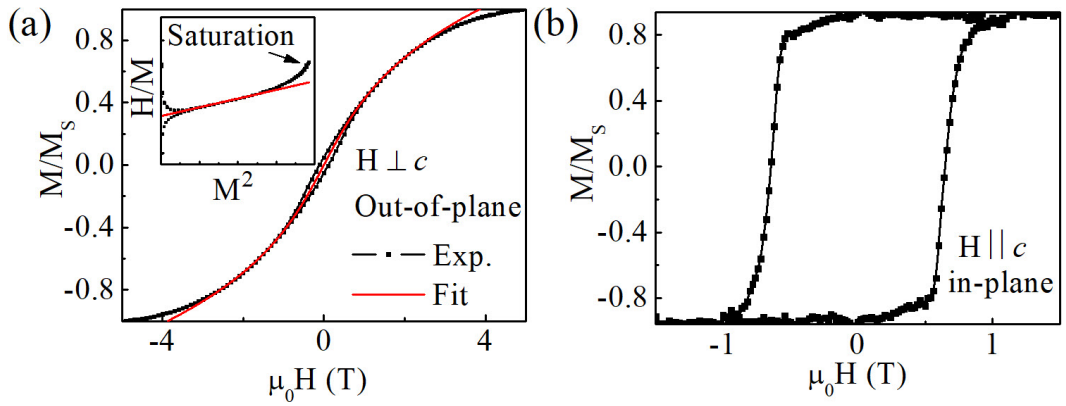

Figure 3.1: VSM measurements of a 20 nm thick film at 2 K. (a) Hysteresis loop (Black squares) measured with magnetic field applied in the in-plane (hard axis) direction. Analytical model (Red solid line) assuming coherent rotation with first and second order anisotropy terms agrees well with the magnetization curve. The values of the first and second order anisotropy terms are extracted from the y-intercept and the slope, respectively, of the straight line fit to the data as shown in the inset. (b) Hysteresis loop measured with magnetic field applied in the out-of-plane (easy axis) direction. This figure has been adapted from [130].

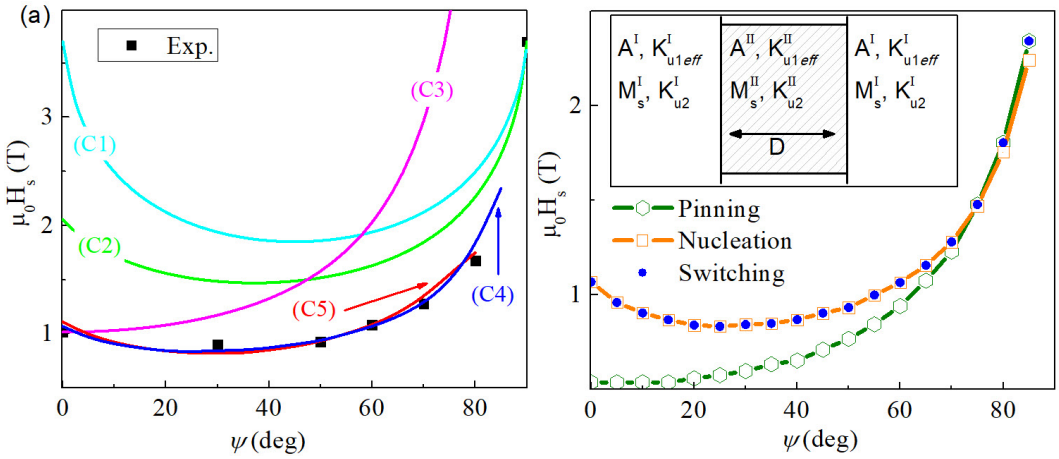

Figure 3.2: (a) Angular dependence of the switching field for a 4 nm thick film at 2 K. Experimental data points are shown by black solid squares. SW model considering only first order anisotropy (C1) and both first and second order anisotropies (C2). Kondorsky model (C3), one-dimensional defect model (C4), and micromagnetic simulations (C5). (b) Angular dependence of the nucleation field (squares) and pinning field (hexagons) obtained from the one-dimensional model of a defect (inset) with the best fit values of the model parameters. The switching fields (circle) coincide with the nucleation fields up to $\psi = 70^\circ$ and with the pinning fields for $\psi > 70^\circ$. This figure has been adapted from [130].

3.2 Angular dependence of the switching field

In Figure 3.2, the angular dependence of switching field from a 4 nm thick film is shown as a function of the angle (ψ) between the direction of the magnetic field and the anisotropy axis (*c*-axis). We have inferred the switching fields (black squares in Figure 3.2(a)) from the magnetoresistance measurements. The magnetoresistance shows hysteresis with two sharp maxima at the same magnitude of positive and negative field values that correspond to the switching fields (H_s) [131]. As observed, the saturation field at $\psi = 90^\circ$ is $\sim$ 3.7 T, which is very close to the hard axis saturation field of 3.8 T for the 20 nm thick film [Figure 3.1(a)]. Assuming the same ratio of K_{u2}/K_{u1} = 0.33 and a saturation field of $H_{sat} = 3.7$ T, the anisotropy energies are calculated to be $K_{u1} = 8.39\times10^5$ J/m^3 and $K_{u2} = 2.75\times10^5$ J/m^3 for this 4 nm thick film. From the angular dependence of the switching field, we attempt to explain the magnetization reversal mechanism based on existing theoretical models.

Again, the simplest form of angular dependence is obtained form the well known Stoner-Wohlfarth (SW) model [144] valid within the macrospin approximation. Assuming only the first order anisotropy, the switching field $H_{\rm s}$ is given by,

$$h_{\rm s}^{2/3}\sin^{2/3}\psi + h_{\rm s}\cos^{2/3}\psi = 1, \tag{3.1}$$

where $h_{\rm s} = H_{\rm s}/H_{\rm sat}$ is the normalized switching field magnitude. The angular variation predicted by this equation shown in Figure 3.2(a) (curve C1) clearly indicates a different switching mechanism being responsible for the observed angular dependence. SW relation can be modified to take into account the second order anisotropy term [145]. In this case the switching field $h_{\rm s}$ is to be numerically solved from the equations below,

$$\begin{aligned} h_{\rm x} &= h_{\rm s}\sin\psi = A\cos^3\theta + B\cos^5\theta, \\ h_{\rm z} &= h_{\rm s}\cos\psi = C\sin^3\theta + B\sin^5\theta. \end{aligned} \tag{3.2}$$

The coefficients in the above two equations are $A = -1 - 6r_{\rm eff}$, $B = 6r_{\rm eff}$, and $C = 1 - 4r_{\rm eff}$, where $r_{\rm eff} = \frac{K_{\rm u2}}{K_{\rm u1,eff}}$ and $K_{\rm u1eff} = K_{\rm u1} - \frac{1}{2}\mu_0 M_{\rm s}^2$. θ is the polar angle (angle between the out-of-plane normal and the magnetization direction) of the magnetization vector. This extended model with second order anisotropy included into the SW calculation, is still insufficient [curve C2 in Figure 3.2(a)] and very different from the angular dependence observed in the experiment. This is not unexpected, as the coherent rotation models are only applicable for smaller particles with dimensions of the order of single domain particle.

A more probable mechanism for magnetization reversal in extended thin films is by nucleation and propagation of reverse domain(s) [146]. In this case the switching field is decided by either of the two related mechanisms: nucleation of reverse domains or propagation of domain walls. As long as the reversal is limited by the nucleation field, the angular dependence may still follow a SW-like behavior even for larger particles [147]. For a thin film, the propagation of a domain wall can be hindered due to imperfections and thus the magnetization reversal process follows the Kondorsky model governed by the domain wall pinning strength. The Kondorsky model has the well-known inverse cosine angular dependence given by the equation,

$$H_{\rm s}(\psi) = \frac{H_{\rm s}(0^\circ)}{\cos\psi}. \tag{3.3}$$

As can be seen from Figure 4, the experimental data in our case does not follow the Kondorsky model [curve C3 in Figure 3.2(a)].

Note that the switching fields are lower than the anisotropy field which is also well-known for other hard magnetic materials such as Sm-Co or Nd-Fe-B [148]. Such deviation can be explained considering nucleation and domain wall pinning due to defects and inhomogeneities in the material [148–150]. Following Sakuma et. al. [149], we assume a simple one-dimensional model with a defect of width D in an otherwise perfect host region infinitely extended in either direction as shown in Figure 3.2(b) inset. This model assumes three dimensionless parameters that defines the defect region: $E = \frac{A_{\rm ex}^{\rm II} K_{\rm u1eff}^{\rm II}}{A_{\rm ex}^{\rm I} K_{\rm u1eff}^{\rm I}}$, $F = \frac{A_{\rm ex}^{\rm II} M_{\rm s}^{\rm II}}{A_{\rm ex}^{\rm I} M_{\rm s}^{\rm I}}$, $G = \frac{A_{\rm ex}^{\rm II} K_{\rm u2}^{\rm II}}{A_{\rm ex}^{\rm I} K_{\rm u2}^{\rm I}}$, where $A_{\rm ex}$ is the exchange constant and superscripts I and II denote the host and the defect regions, respectively. The defect region is considered to be magnetically weaker than the host so that, $0 \leq E, F \leq 1$. We also assume that both the first and second order anisotropy energies are lowered by the same ratio in the defect giving $E = G$ (instead of $G = 0$ as has been considered in [151]). From a uniformly magnetized initial state, as the external magnetic field is increased to reverse the magnetization, magnetization inside the defect region starts to follow the external field more closely than the host region. The maximum field above which a reverse domain appears inside the defect i.e., the magnetization inside the defect points towards the external magnetic field, is defined as the nucleation field. The pinning field is defined as the maximum field above which the defect region fails to limit the growth of an already reversed domain into the host regions. Depending on the values of E, F, D and ψ, a reversed domain inside the defect could either escape into the host region, triggering magnetization reversal at the nucleation field or remain pinned inside the defect region until the value of the pinning field is reached. The higher of these two fields decides the switching field. For each set of E, F and D, the nucleation and pinning fields are obtained as a function of ψ and compared with the experimentally observed angular dependence. The best fit is obtained with $E = 0.23$, $F = 1.0$ and $D = 14$ nm. With these parameters the switching field from this model agrees well with the experimentally observed angular variation of the switching field [curve C4 in Figure 3.2(a)]. The corresponding nucleation and pinning fields are shown in Figure 3.2(b) which reveals that nucleation dominates the switching

mechanism for $\psi < 70°$, above which the pinning field exceeds the nucleation field. This simple model adequately explains the comparative role of nucleation and pinning in the switching process.

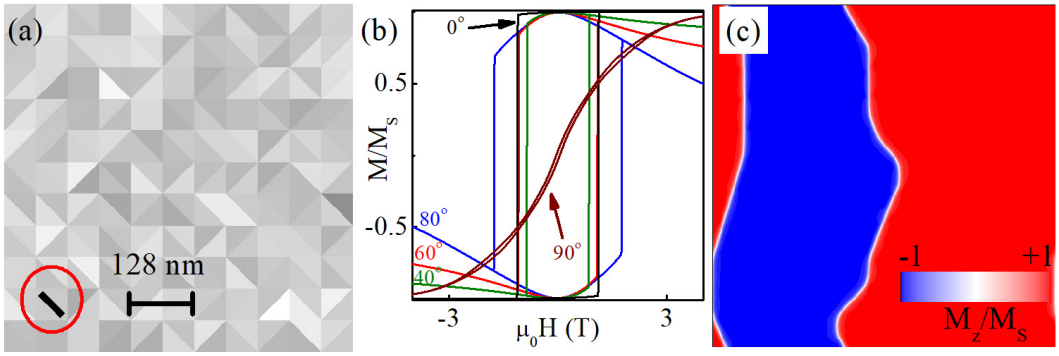

Figure 3.3: (a) The variation of the anisotropy energy K_{u1} over randomly organized triangular grains considered in the micromagnetic model. Black to White corresponds to minimum to maximum value of the anisotropy energy. The defect is marked by the red circle. (b) Simulated hysteresis loops for different orientation of the magnetic field. Average out-of-plane component of magnetization (M_z) shows rectangular hysteresis loops for magnetic field orientations $\psi \leq 80°$. For $\psi = 90°$, average in-plane component of magnetization (M_x) is plotted. (c) Domain structure formed at remanence after saturation in the applied magnetic field with $\psi = 90°$. The scale bar is same for (a) and (c). This figure has been adapted from [130].

3.3 Micromagnetic simulations

We attempt to picturize the magnetization reversal dynamics by means of micromagnetic simulations using MuMax3 micromagnetic simulator [42]. The microstructure of the thin film is modeled in the simulation as randomly organized isosceles right triangles [Figure 3.3(a)]. Our assumption is valid since the STM morphologies of the film shows random azimuthal distribution of triangular or hexagonal features of sizes 50 nm $-$ 100 nm and their merging in various ways to form a continuous film [130]. We believe that this random orientation can produce a variation in the arrangement of the spins, giving rise to a randomly distributed domain structure with the spins inside each domain oriented in the same direction. Presence of spiral-like features can also add up to this cause. Existence of such imperfections suggests that a variation in the magnetic

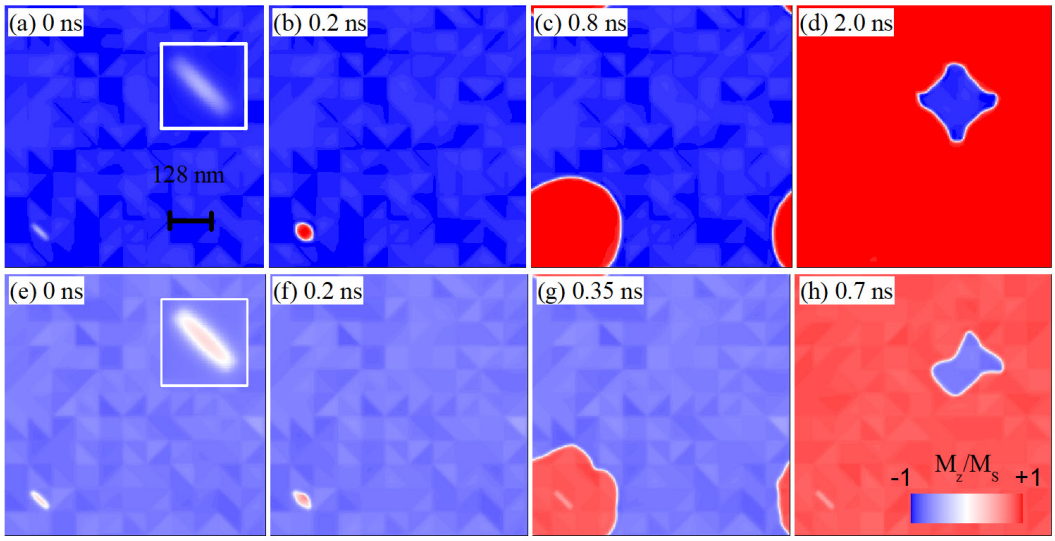

Figure 3.4: Magnetization dynamics observed in the micromagnetic simulation during switching from -z magnetized state to +z magnetized state. (a)-(d) show switching by reverse domain nucleation and domain wall propagation at an applied field of 0.93 T along $\psi = 10^\circ$ direction. Inset of (a) shows the magnetization inside the defect region at the onset of nucleation. (e)-(h) shows the switching by domain wall depinning and propagation at an applied field of 1.56 T along $\psi = 75^\circ$ direction. Inset of (e) shows the presence of an already nucleated reversed domain inside the defect. (a)-(h) follows the same color scale shown in (d). Length scale of (a)-(h) is shown in (a). This figure has been adapted from [130].

properties may also exist from island to island, as well as at the boundaries. The surface roughness estimated from STM imaging is found to be less than 1 nm and thus neglected in the micromagnetic model. For the micromagnetic simulations, a total of 242 grains were considered which results into simulation geometry of 704 nm $\times$ 704 nm $\times$ 4 nm. A space discretization size of 1.375 nm is considered along x and y directions and a space discretization of 2 nm is considered along z direction. Periodic boundary conditions are applied along the x and the y directions. The exchange energy constant used is 10 pJ/m, and both the saturation magnetization and exchange constant are assumed to be homogeneous throughout the thin film, as we have obtained F = 1 for the best fit considering the one-dimensional model. The anisotropy energies (both K_{u1} and K_{u2}) are assumed to be the same within each grain, but vary from grain to grain following a Gaussian distribution with a variation of 5 % of the corresponding average values. For each grain the

uniaxial anisotropy axis is also assumed to be randomly oriented with a tilt of 5° from the out of plane direction. A rectangular defect region of width $D = 14$ nm is considered at the boundary of two triangular grains [Figure 3.3(a)]. The material parameters inside the defect region are set such that $E = 0.23$ and $F = 1$ are fulfilled. An energy minimization solver [42] is used to simulate the hysteresis loops and a time integration solver with a damping constant of 0.5 has been used to simulate magnetization dynamics. We have considered $T = 0$ K for all the simulations.

Figure 3.3(b) shows the simulated hysteresis loops for the magnetic field applied at different angles from the out-of-plane direction. The in-plane hysteresis loop ($\psi = 90^\circ$), shown in Figure 3.3(b), agrees with the experiment ([Figure 3.1(a)]) qualitatively and shows similar narrow loop opening. The remanence state is always uniformly magnetized along $\pm z$ direction for $\psi \leq 80^\circ$, whereas, multiple domain walls are observed in the in-plane ($\psi = 90^\circ$) remanence state as shown in Figure 3.3(c). This also explains the higher magnetoresistance observed in the experiment at zero field for $\psi = 90^\circ$ as compared to $\psi \leq 80^\circ$ [131].

The magnetization configuration at different stages during switching for $\psi = 10^\circ$ and $\psi = 75^\circ$ are shown in Figure 3.4 (a)-(d) and (e)-(h), respectively. For both the cases, the nucleation is expected to initiate at a location where the anisotropy is much lower compared to the neighboring grains. In our simulation, the defect region has the lowest anisotropy energy [see Figure 3.3(a)], and thus acts as the nucleation center. Figure 3.4(a) shows the initial (time = 0 ns) magnetization configuration at the switching field. The magnetization inside the defect [inset in Figure 3.4(a)] starts deviating from the rest of the film and initiates the nucleation as time progresses [Figure 3.4(b)]. As the pinning field is lower than the nucleation field at $\psi = 10^\circ$, the nucleated reverse domain grows out of the defect region and gradually propagates to complete the switching as seen from Figure 3.4 (b)-(d). At $\psi = 75^\circ$, the initial magnetization configuration in Figure 3.4(e) shows an already nucleated domain [inset in Figure 3.4(e)] inside the defect. However, as the pinning field is higher than the nucleation field in this case, the reversed domain remained pinned in lower applied fields (not shown). When the magnetic field is increased further to the pinning field [shown in Figure 3.4(e)], the reverse domain overcomes the energy

barrier and the domain wall gradually propagates to complete the magnetization reversal as seen from Figure 3.4 (f)-(h). The angular dependence of the switching field obtained from the micromagnetic simulations, shown in Figure 3.2(a) (curve C5), also agrees well with the experimentally observed values. We note that the specific morphological features and defects can also contribute to the switching behavior. However, our simple model with a one-dimensional defect satisfactorily explains the angular dependence of the switching field observed in the experiment.

3.4 Summary

This chapter describes the magnetic anisotropy and magnetization reversal properties of epitaxial Cr_2Te_3 thin films based on magnetic and magneto-transport measurements. Anisotropy coefficients are estimated from the magnetization curves measured along the easy and hard axis directions. The angular dependence of the switching fields is then compared to different models to obtain insights into the magnetization reversal processes. Strong perpendicular anisotropy in Cr_2Te_3 thin films could be useful for achieving thermally robust nanomagnets for spintronics applications, as well as a high coercivity rare-earth-free material for permanent magnet applications. The angular dependence of the magnetization reversal in the film exhibits a complex nature. We show that a simple one-dimensional micromagnetic model of a defect can explain the angular variation satisfactorily. The magnetization switching dynamics studied using micromagnetic simulations confirmed the relative role of nucleation and pinning processes.

Although strong perpendicular magnetic anisotropy properties of this material makes it very attractive for magnetic devices, the Curie temperature has to be increased before it can be considered for practical applications. Further investigations with different compositions of this material may provide a solution with higher Curie temperature together with strong perpendicular magnetic anisotropy. Moreover suitable material combinations have to be devised so that these materials could be integrated into magnetic tunnel junction structures with strong spin-filtering properties.

Chapter 4

Write error rates of perpendicular spin-transfer-torque random access memory

Micromagnetic and macrospin calculations presented in the previous chapters do not take into account the effects of the thermal fluctuation field. The influence of thermal fluctuations on the magnetization cannot be ignored for practical device operating at finite-temperatures. In the equilibrium condition, random thermal kicks continuously deflect the magnetization from the energy minimized state. As discussed in Chapter 1, if the energy barrier between the energy minima is not high enough (compared to the thermal energy), these thermal kicks alone could trigger magnetization reversal. During magnetization reversal under external magnetic fields or currents, thermal fluctuations can assist or resist the reversal process randomly. As a result magnetization reversal becomes a stochastic process. These effects must be considered while evaluating the performance of a magnetic device or associated circuits. In this chapter, we focus on the write process of perpendicular STTRAM in presence of thermal fluctuation field.

The write process in an STTRAM bit becomes inherently stochastic due to the thermal fluctuation field. As a result, the time taken by the bit (magnetization of the free layer) to switch has a wide distribution [11, 45]. There will be a non-zero probability that

The results reported in this chapter have been published in the journal article titled "Write error rate of spin-transfer-torque random access memory including micromagnetic effects using rare event enhancement" by U. Roy, T. Pramanik, L. F. Register, S. K. Banerjee in IEEE Transactions on Magnetics, vol. 52, issue 10, pages 1-6, 2016. Contributions: U. Roy and L. F. Register conceived the idea. U. Roy initiated the work. T. Pramanik developed the codes and ran the simulations with help from U. Roy. L. F. Register and S. K. Banerjee supervised the work. U. Roy, T. Pramanik and L. F. Register wrote the manuscript. T. Pramanik is the corresponding author for the publication. All authors reviewed and commented on the results and the manuscript.

when a finite duration write pulse is turned off, the bit still will not have been written and a so-called write error will have taken place [11]. The probability that a write error takes place for a given applied current pulse of a given length is called the write error rate (WER). For correct operation of the STTRAM array, the WER needs to be $\sim 10^{-9}$ or less (depending on the requirement set by the error correction circuit (ECC) in the chip [11]). As a result, accurate modeling of the low probability tail of the WER becomes critical. WER of STTRAM bits can be modeled precisely within the macrospin approximation from the Fokker-Planck (FP) equation [51]. Landau-Lifshitz-Gilbert-Slonczewski (LLGS) simulations within the macrospin limit with a stochastic thermal field added also have been performed with up to $\sim 10^5$ independent switching trials to model switching time distributions [152]. However, experimentally observed effects such as sub-volume excitations [153] and the branching of the WER plots and associated higher than otherwise expected WER [154, 155] cannot be captured within the macrospin approximation. For an in-depth understanding and accurate prediction of the low probability tails of WER, micromagnetic effects must be taken into account. Previously, WER calculation including micromagnetic effects have been carried out using 64 and 10^3 independent stochastic simulations in [156] and [157], respectively. However, the extreme tails of WERs cannot be captured in this way for micromagnetic or even macrospin simulations.

In this chapter, first we'll summarize the available options to estimate WER of a STTRAM bit within the macrospin approximation. Next, we show calculation of WERs using stochastic LLGS simulations combined with a "rare event enhancement" (REE) technique [158]. Similar REE techniques have been used for Monte Carlo simulation of other systems where rare events nevertheless remain important [159, 160]. REE artificially enhances the rate of occurrence of low probability events while proportionately reducing their weights. We'll describe a prototype REE method tailored to the STTRAM switching physics and illustrate it with macrospin stochastic LLGS calculations, which allows comparison to reference FP results. Then we will provide results for full *micromagnetic* stochastic LLGS simulations, demonstrating the ability to reliably predict WER to 10^{-9} and likely beyond for sets of only $\sim 10^3$ ongoing LLGS simulations, with applied currents consistent with practical usage.

4.1 WER calculation within the macrospin approximation

4.1.1 Stochastic LLGS equation

Thermal fluctuations can be included in the micromagnetic framework following the approach of Brown [49, 50]. The stochastic version of LLGS equation that includes the thermal fluctuation field is given by,

$$\frac{d\bar{m}}{dt} = -\gamma(\bar{m} \times [\bar{H}_{\rm eff} + \bar{H}_{\rm th}]) + \alpha(\bar{m} \times \frac{d\bar{m}}{dt}) + \gamma\beta\epsilon(\bar{m} \times (\bar{m}_{\rm p} \times \bar{m})), \tag{4.1}$$

where, $\bar{H}_{\rm th}$ is the stochastic thermal field. Components of $\bar{H}_{\rm th}$ obey the relations $\langle H_{\rm th,i}(t)\rangle = 0$ and $\langle H_{\rm th,i}(t)\rangle H_{\rm th,j}(t')\rangle = 2D\delta_{\rm ij}\delta(t-t')$, with $i = x, y, z$ being the Cartesian co-ordinate axes and $D = \frac{\alpha k_{\rm B}T}{(1+\alpha^2)\gamma\mu_0 M_{\rm s}V}$. All other terms have their usual meaning as explained in Chapter 1. For micromagnetic simulations, V (in the expression for D) is the volume of one discretized cell, while in the macrospin limit, V is simply the volume of the magnet (e.g., free layer volume in an STTRAM bit).

Equation 4.1 must be integrated properly to yield the correct solution. In this work, we have used Heun scheme to integrate the above equation with small enough time steps to ensure convergence [161]. Details of the numerical integration algorithm are available in [161]. In each time step the components of $\bar{H}_{\rm th}$ are calculated by drawing numbers randomly from a Gaussian distribution with zero mean and unit standard deviation, and then multiplying it with an appropriate prefactor that decides the strength of the thermal kick. Because of this random field added to the total effective field, the magnetization trajectories will now be different for each trial simulation.

Figure 4.1(a) shows a few stochastic magnetization trajectories of a macrospin perpendicular STTRAM (P-STT) bit calculated using Equation 4.1. If the transition in the magnetization is not yet complete when the current pulse turns off, the FL magnet could return to the initial state causing a write failure.

The switching (or error) probability can also be estimated by calculating the switching time distribution for a bit for a given current density. In this case, the current is left turned on for long enough time to switch all of the trial simulations (e.g., 10^5 in Figure 4.1) for the same P-STT bit with the same applied current density. The

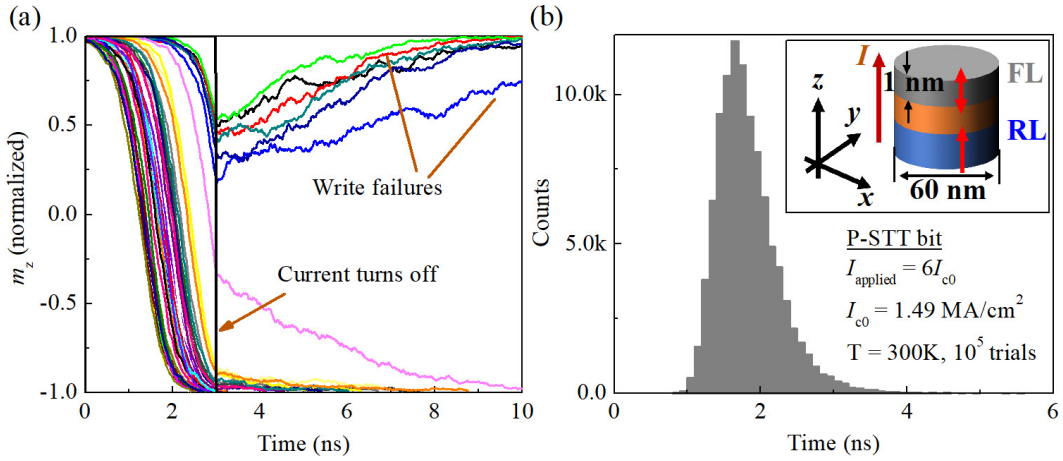

Figure 4.1: (a) Stochastic magnetization trajectories of out-of-plane component of magnetization, m_z, for a perpendicular FL magnet, calculated from macrospin simulations. The current pulse is turned on at time $t = 0$ ns and turned off at $t = 3$ ns. (b) Switching time distribution obtained by simulating 10^5 instances of the same P-STT bit. Inset shows the schematics of the bit with the dimensions of the magnets, direction of current flow and axes convention. Details of the simulation parameters are described in Section 4.2.1.

switching times (time taken to reach $m_z = 0$) for each of these cases are then noted. The distribution of these switching times is shown in Figure 4.1(b). In general the shape of this distribution is not symmetric and the degree of asymmetry varies depending on the applied current density. From the switching time distribution, as in Figure 4.1(b), one can then estimate the variation of switching probabilities, $P_{\rm sw}$ or unswitched probabilities, WER $= 1 - P_{\rm sw}$. Figure 4.2(a)) and 4.2(b) show variations of $P_{\rm sw}$ and WER, respectively, with time for various strength of applied currents. The logarithmic scale of Figure 4.2(b) clearly shows unreliable estimates below WER $= 10^{-4}$ for the WER curves obtained from the stochastic LLGS simulations. To get reliable estimates of WER to 10^{-9}, more than 10^9 simulations will be required. Fortunately, if the macrospin description is valid, WER of STTRAM bits can be modeled precisely from the Fokker-Planck (FP) equation [51, 162].

4.1.2 Fokker-Planck equation

The derivation of the Fokker-Planck (FP) equation governing the thermal fluctuation of a single domain magnet was described also in Brown's paper [49]. More recent

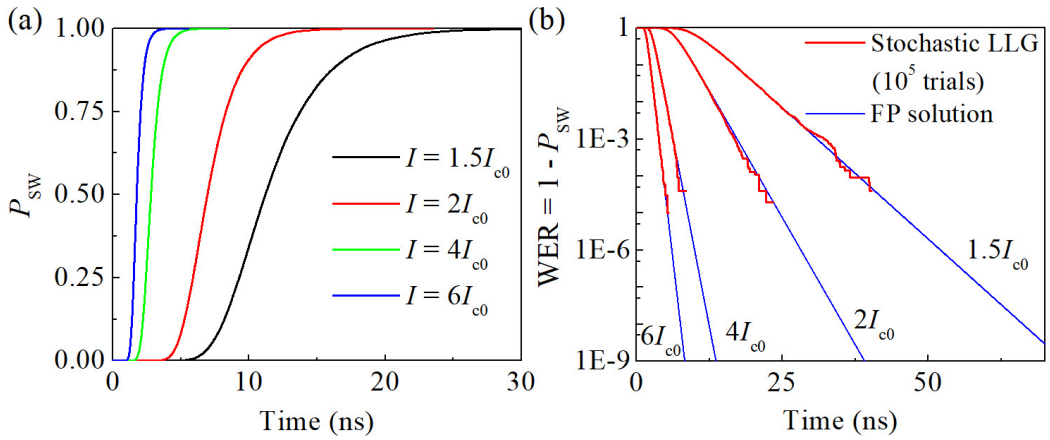

Figure 4.2: Variation of (a) Psw and (b) WER with time for different strengths of applied current. WERs obtained from FP equation is also shown in (b) for comparison. Details of the simulation parameters are described in Section 4.2.1.

derivation including the STT term can be found in [50, 51]. The magnetization unit vector can be represented in the spherical co-ordinate by the angles (θ, ϕ), where θ and ϕ are the polar and azimuthal angles of the magnetization vector $\bar{m}$. If $W(\theta, \phi, t)$ denotes the probability of the magnetization being pointed at the direction (θ, ϕ) at time t, then the FP equation is given by,

$$\frac{\partial W}{\partial t} = -\bar{\nabla}_{\text{sph}} \cdot \bar{J}, \tag{4.2}$$

where $\bar{\nabla}_{\text{sph}} = \left(\hat{\theta}\frac{1}{\sin\theta}\frac{\partial}{\partial\theta}, \quad \hat{\phi}\frac{\partial}{\partial\phi} \right)$ is the gradient in spherical co-ordinate excluding the term for the radial direction. The total surface current density $\bar{J} = \left(\hat{\theta}J_\theta, \quad \hat{\phi}J_\phi \right)$ is given as,

$$\begin{aligned} J_\theta &= \frac{\gamma}{1+\alpha^2}(H_\phi + \alpha H_\theta - \alpha A^{\text{ST}} m_{\text{p}}^\phi + A^{\text{ST}} m_{\text{p}}^\theta)W - k\frac{\partial W}{\partial \theta}, \\ J_\phi &= \frac{\gamma}{1+\alpha^2}(\alpha H_\phi - H_\theta + A^{\text{ST}} m_{\text{p}}^\phi + \alpha A^{\text{ST}} m_{\text{p}}^\theta)W - \frac{k}{\sin\theta}\frac{\partial W}{\partial \phi}, \end{aligned} \tag{4.3}$$

where the diffusion constant $k = \frac{k_B T}{M_s \mu_0 V(1+\alpha^2)}$, $H_\theta = \bar{H}_{\text{eff}} \cdot \hat{\theta}$, $H_\phi = \bar{H}_{\text{eff}} \cdot \hat{\phi}$, $m_{\text{p}}^\theta = \bar{m}_{\text{p}} \cdot \hat{\theta}$, $m_{\text{p}}^\phi = \bar{m}_{\text{p}} \cdot \hat{\phi}$, and $A^{\text{ST}} = \beta\epsilon$.

Considering the axial symmetry of a circular magnet as in the P-STT bit, ϕ dependence in the above FP equation can be dropped and the equation for a circular uniaxial

magnet may be written as [51],

$$\frac{\partial W}{\partial \acute{t}} = -\frac{1}{\sin\theta}\frac{\partial}{\partial\theta}\left[\sin^2\theta\left(-i_{\rm app}-\cos\theta\right)W - \frac{1}{2\Delta^{\rm P-STT}}\sin\theta\frac{\partial W}{\partial\theta}\right], \tag{4.4}$$

where $\acute{t} = t\frac{\alpha\gamma H_{\rm K}^{\rm P-STT}}{(1+\alpha^2)}$ is the normalized time, $i_{\rm app} = I_{\rm app}/I_{\rm c0}$ is the normalized applied current with $I_{\rm c0}$ being the critical current and Δ being the thermal stability factor of the P-STT bit. $H_{\rm K}^{\rm P-STT}$ is the effective perpendicular anisotropy field as explained in Section 1.2.1. Equation 4.4 can now be solved numerically for $W(\theta,t)$ using a finite difference grid from $\theta = 0$ to $\theta = \pi$ to obtain the time evolution of the probability density $W(\theta,t)$ for a given applied current. Assuming an initial magnetization along the $+z$ direction ($\theta = 0$), the initial probability distribution of $\bar{m}$ is obtained from a Boltzmann distribution as follows:

$$\begin{aligned} W(\theta, t=0) &= W_0 \exp\left[-E(\theta)/k_B T\right], \\ \int_0^{\pi/2} W(\theta, t=0)\sin\theta\, d\theta &= 1, \end{aligned} \tag{4.5}$$

where $E(\theta)$ is the total energy (including magnetostatic and uniaxial anisotropy) of the bit as a function of the orientation θ. Finally, the WER at time t is given by:

$$\mathrm{WER}(t) = \int_0^{\pi/2} W(\theta,t)\sin\theta\, d\theta, \tag{4.6}$$

where $W(\theta,t)$ is the solution obtained from Equation 4.4. Figure 4.2(b) shows the WER estimated from FP solutions together with the WER obtained from the stochastic LLGS equation.

In the next section, we describe the rare-event-enhancement (REE) technique to estimate WER to 10^{-9} with only 10^3 stochastic LLGS simulations.

4.2 Rare event enhancement technique to estimate write error

4.2.1 Details of the simulated bit

The simulated P-STT bit (as shown in Figure 4.1(b) inset) is assumed to have a free layer (FL) magnet of circular cross-section with a diameter of 60 nm and thickness of 1 nm. Only the FL magnet is considered in all simulations in this work assuming the

fixed layer to act only as a source of spin-polarized current that flows perpendicular to the plane of the FL (along the z direction). The spin-polarization direction, $\bar{m}_{\rm p}$, of the current is along the $+z$ axis with a spin torque efficiency factor (spin polarization factor) $\eta = 0.4$. A saturation magnetization $M_{\rm s} = 1.1 \times 10^6$ A/m, a uniaxial anisotropy energy $K_{\rm u1} = 8 \times 10^5$ J/m^3 with axis along the z direction, and a Gilbert damping constant $\alpha = 0.01$ were used. Assuming a rectangular box with sides 60 nm $\times$60 nm $\times$1 nm, the demagnetization factors are calculated to be: $N_{\rm xx} = N_{\rm yy} = 0.027$ and $N_{\rm zz} = 0.946$ [43]. The simulation temperature was set to $T = 300$ K. With the above parameters, the thermal stability factor of the PMA bit (calculated from Equation 1.13) is $\Delta \approx 67$ and the critical current for STT switching (calculated from Equation 1.15) is $I_{\rm c0} = 42.1$ μA. Heun's [161] scheme was used for integrating the stochastic LLGS equation with an integration time step of 1 fs for these macrospin simulations. Initial ($t = 0$) equilibrium thermal distributions of $\mathbf{m}(t)$ were obtained by starting with a value of $m_z = 1$ at $t = -5$ ns and performing the stochastic LLGS simulation up to $t = 0$ ns with no STT.

4.2.2 Basic method

We employ a REE method known as "importance splitting" [163–166]. The core idea is that for many stochastic systems, before the system reaches some state of extremely low level of probability L_N, it traverses multiple intermediate higher levels of probability [166]. Thus, extremely rare events can be reached with high probability by, from time to time, splitting "parent" trajectories that are more likely to lead to rare events into multiple "offspring" trajectories, but each of corresponding lower weight than the parents to conserve the norm. Each offspring trajectory then follows its own stochastically independent trajectory. Beyond this point, there is both much generality and detail to importance splitting methods and their optimization, which is beyond the scope of this work. Our goal here is only to demonstrate a specific, relatively simple, prototype adaptation to stochastic LLGS simulation of STTRAM switching as a proof-of-concept and starting point.

The first critical order of business is to choose a predictor of which trajectories are more likely to lead to rare events than others. For this STTRAM, the state of the bit

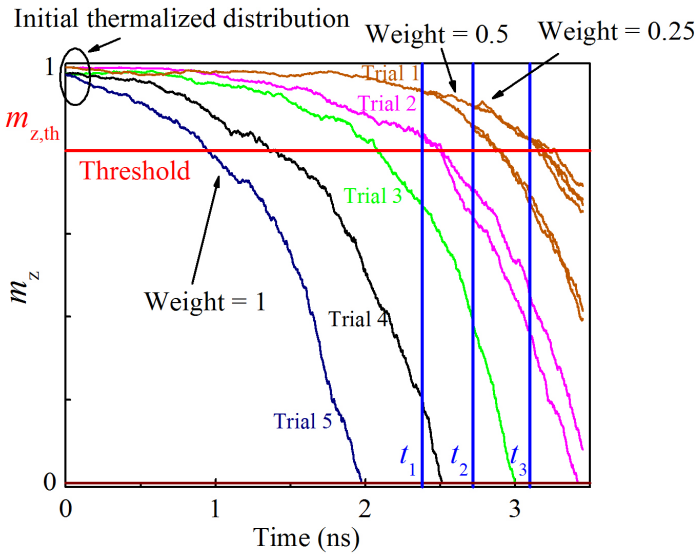

Figure 4.3: Enhancement of rare stochastic LLGS magnetization trajectories of the (normalized) m_z at discrete times $= t_1$, t_2, t_3 etc. STT switching is initiated at $t = 0$ ns from a thermalized distribution with m_z close to unity. Starting with m_z near but not at 1 due to the stochastic thermal field, the bit magnetization trajectories are pushed toward $m_z = -1$ due to STT but still subject to the stochastic thermal field, as the time progresses. Enhancement times are marked by blue vertical lines. The threshold value value of m_z is marked by the red horizontal line. This figure has been adapted from [158].

can be characterized reasonably by the surface-normal component of the magnetization normalized to the magnitude of the total magnetization, m_z such that $1 \geq m_z \geq -1$. At any time t, the greater $m_z(t)$, the smaller the in-plane component of the (normalized) magnetization $\mathbf{m}(t)$, the smaller the STT on the bit, and the slower the bit is being accelerated toward $m_z = -1$, and, thus, the longer switching is likely to take from that time forward. Moreover, the closer $m_z(t)$ is to unity, the greater the relative importance of the continuing stochastic thermal field as compared to the STT, and, thus, the less deterministic at least near future trajectories $\mathbf{m}(t)$ will be, where splitting completely deterministic trajectories serves no purpose even if that trajectory is likely to lead to a rare event. Thus, we chose m_z as our measure of the likelihood that a magnetization trajectory $\mathbf{m}(t)$ will ultimately lead to a rare non-switching event, as well as the potential usefulness of importance splitting of the trajectory.

The prototype REE procedure used here is illustrated in Figure 4.3. This figure and the chosen trajectories are optimized for conceptual clarity and not results. These trajectories also are for a P-STT bit of circular cross-section in the macrospin approximation, but for this prototype method the approach is the same for micromagnetic simulations. The simulation of switching is subdivided into time intervals of variable length $\tau_l = t_{l+1} - t_l$. These time intervals are adjusted on the fly such that, for a substantial set of trajectories $\mathbf{m}(t)$ considered simultaneously, the time interval is terminated when the number of trajectories for which m_z has fallen below zero at the end of the time interval is approximately equal to the number of trial for which m_z is closer to unity than a chosen m_z threshold value $m_{z,\mathrm{th}}$ (the choice of which will be returned to below). Then, at the beginning of each new time interval beyond the first, the parent trajectories $\mathbf{m}(t)$ with $m_z > m_{z,\mathrm{th}}$ are subdivided into two offspring trajectories, each weighted by one-half the weight of the parent trajectory, which then continue along their own stochastically independent subsequent trajectories; trajectories with $m_{z,\mathrm{th}} \geq m_z > 0$ are continued as they are with the same weighting; and trajectories with $m_z \leq 0$ are considered switched and are discontinued. (Trajectories with $m_z \leq 0$ are considered beyond the point of no return *if* the pulse were to continue. That some trajectories with $m_z \leq 0$ might not end up switched if the write pulse were turned off at this point or, conversely, that some trajectories with $m_z > 0$ would nevertheless end up switched if the write pulse were turned off at this point should not noticeably affect the WER within the resolution of interest here.) In principle, the total number of ongoing trajectories would be conserved precisely at all times in this way if we could terminate time intervals when the number of trajectories with $m_z \leq 0$ and the number with $m_z > m_{z,\mathrm{th}}$ were precisely equal. In practice, however, we have to stop and restart all of the stochastic LLGS simulations to check these numbers, which, so far, we have done at fixed small but nonzero time intervals. As a result we have allowed for a limited inequality, and the total number of ongoing trajectories can differ somewhat from the original through time. However, we also adjust the inequality window about the equality through time to bias the number of ongoing trajectories back toward the original value, so that the number of trajectories $\mathbf{m}(t)$ and—the associated computational effort of solving the stochastic LLGS simulations—remains effectively conserved

through simulation time. However, the enhancement of rare trajectories at the expense of more common trajectories during each time interval leads to an ultimately strong artificial skewing of the magnetization trajectories toward the rare events of interest, with the possibility of a given individual trajectory remaining within the l^{th} time interval τ_l having been enhanced by up to 2^l in the limit.

For Figure 4.3, specifically, a small illustrative sample of magnetization dynamics trajectories has been plotted vs. time along with a relatively low (far from unity) threshold $m_{z,\text{th}} = 0.8$ used for visual clarity. Trial trajectories 1 and 2 have $m_z > m_{z,\text{th}}$ at the beginning of the first enhancement t_1—a time determined considering many more trajectories not shown—and, hence, each of them are split into 2 offspring trajectories, each with their weights reduced from unity to 0.5. Trial trajectories 3 and 4 have $0 < m_z \leq m_{z,\text{th}}$, and hence advance as they are without any enhancement. Trial trajectory 5 has reached a negative value of m_z at t_1 (not shown) and is discontinued. At time t_2 both offspring trajectories of Trial trajectory 1 are again split in two offspring trajectories each, and each with a weight now reduced to 0.25, while Trial trajectory 4 is discontinued. This procedure continues at t_3 and beyond.

Like the choice of the predictor of low probability events, the choice of the threshold value of the predictor also is important. It also is non-trivial. To this end we now turn to a study of WER for macrospins calculated with our REE method. These macrospin simulations are, of course, computationally less demanding than micromagnetic simulations and, thus, allows for more simulations and larger data sets. They also allow for comparison to reference FP results.

4.2.3 Choosing threshold and illustration of REE using macrospin simulations

Figure 4.4 shows the simulated probabilities as a function of time of not having switched —essentially the WER if applied current were turned off at that time as discussed in the previous section —for the P-STT bit obtained with REE for three different values of $m_{z,\text{th}}$ as shown (Figure 4.4(b-d)), as well as without REE (Figure 4.4(a)) for reference. The applied current is $2I_{\text{c0}}$. Each of the, here, 100 simulation sets consist

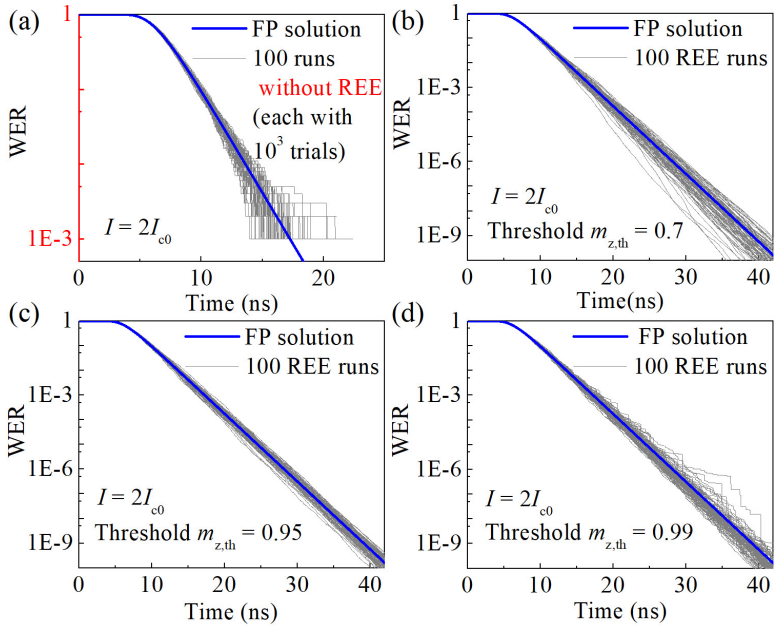

Figure 4.4: Effect of selection of threshold $m_{z,\mathrm{th}}$ used for REE on the calculated WER for a macrospin with an applied current of twice the critical current, I_{c0}, (thin lines, grey online) with the FP solution provided for reference (thick lines, blue online). The results of each figure represent 100 sets (each represented by its own grey line) of 10^3 independent trials. (a) Results without REE for reference. Intrinsically, the lowest non-zero value of WER for each set is 10^{-3} as seen. (b), (c) and (d) Results with REE with thresholds, $m_{z,\mathrm{th}} = 0.7$, 0.95 and 0.99, respectively. All choices of $m_{z,\mathrm{th}}$ provide vastly improved estimations of WER as compared to simulations without REE, but $m_{z,\mathrm{th}} = 0.95$ clearly provides the best of the three. This figure has been adapted from [158].

of 10^3 independent trials. Here a "trial" corresponds to a single initial trajectory, which subsequently may or may not give rise to one or more offspring trajectories. As the total weighting including continuing and switched (terminated) trajectories is conserved for each trial, the total weighting for all trajectories springing from all trials in a set is 10^3 at all times. Therefore, WER for each set of trials may be written as,

$$\mathrm{WER}(t) = \frac{\sum_{\mathrm{not-switched\,trajectories}} \mathrm{Weight}}{\sum_{\mathrm{all\,trajectories}} \mathrm{Weight}} = \frac{\sum_{\mathrm{not-switched\,trajectories}} \mathrm{Weight}}{10^3}. \quad (4.7)$$

As can be seen in Figure 4.4, use of REE with any of the choices of $m_{z,\mathrm{th}}$ provides vastly improved estimations of WER. However $m_{z,\mathrm{th}} = 0.95$ clearly provides the least variability among these choices. Consistent with the discussion of the previous subsection, if $m_{z,\mathrm{th}}$ is too low (further from unity), then, we waste REEs on too many trajectories

that are already largely deterministic. If $m_{z,\mathrm{th}}$ is too high (closer to unity), we miss REEs for too many trajectories that remain largely stochastic. Indicative of this latter limit is the quasi-step like behavior for many of the trial sets, noticeable at fairly large WERs but increasing in scale as WER decreases, as seen in Figure 4.4(d), partially reminiscent of the behavior for the REE free result of Figure 4.4(a) if at much smaller WERs.

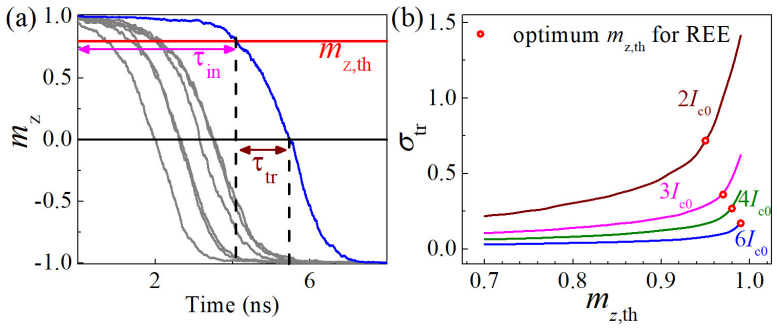

Figure 4.5: (a) Definition of transit time (τ_{tr}) and incubation time (τ_{in}) for an example stochastic magnetization trajectory marked in blue, for a candidate threshold $m_{z,\mathrm{th}}$ (marked by the red horizontal line). (b) Variation of standard deviation of τ_{tr} (σ_{tr}) of 10^3 trajectories as a function of the threshold $m_{z,\mathrm{th}}$. The optimum threshold for each current is marked as a red circle on the corresponding curves. This figure has been adapted from [158].

Toward identifying the optimum threshold a priori, a significant sample of individual trials—10^3 again for our simulations—of $\mathbf{m}(t)$ were simulated without REE. As shown in Figure 4.5(a), for each of these trials a "transit" time (τ_{tr}) was identified as a function of $m_{z,\mathrm{th}}$, which is defined as the time required for $\mathbf{m}(t)$ to fall from $m_z = m_{z,\mathrm{th}}$ to $m_z = 0$ (and, similarly, an "incubation" time (τ_{in}) is identified as the time for $\mathbf{m}(t)$ to reach $m_{z,\mathrm{th}}$ from $t = 0$) consistent with prior work [167–169]. We then considered the standard deviation in the transit time (σ_{tr}) among all trials. We found that the inflection point in this curve, as shown in Figure 4.5(b), provides a reasonably optimal value of $m_{z,\mathrm{th}}$ as the inflection signifies a transition between more stochastic paths with thus large variability in transit times, and more deterministic paths with thus similar transit times. In particular, the 0.95 value for $2I_{\mathrm{c0}}$ that was predicted in this way is consistent with the results of Figure 4.4. Moreover, as can be seen, the optimum value of $m_{z,\mathrm{th}}$ increased toward unity with increased applied current. The greater the current, the greater the STT

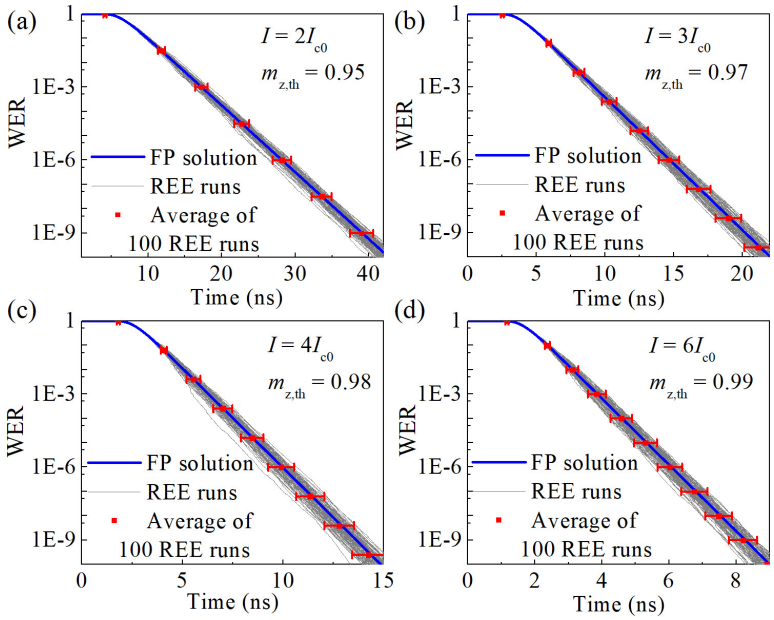

Figure 4.6: REE simulation of WER using a current-dependent optimized $m_{z,\mathrm{th}}$ threshold for an applied current of (a) $2I_{\mathrm{c0}}$, (b) $3I_{\mathrm{c0}}$, (c) $4I_{\mathrm{c0}}$, (d) $6I_{\mathrm{c0}}$. Error bars (red) represent $\pm 2\sigma$ among the samples. FP results (blue lines) are provided for comparison. This figure has been adapted from [158].

for a given value of m_z, the less deviation of m_z from unity that is required for the STT to overcome the thermal fluctuation field on average.

Figure 4.6 shows the WER for 100 sets of 10^3 trials each obtained with REE using the optimum thresholds found from Figure 4.5(b) for applied currents of $I = 2I_{\mathrm{c0}}$, $3I_{\mathrm{c0}}$ and $4I_{\mathrm{c0}}$, respectively, along with error bars representing a plus or minus two standard deviations $\pm 2\sigma$ (95%) confidence interval for the *individual* trial sets based on the variation among them. The $\pm 2\sigma$ confidence interval for the average result of all 100 sets of trials considered as a whole is an order of magnitude smaller still. This later average of the predicted WER from the all REE enhanced stochastic LLGS trials follows the exact FP solution quite well.

4.3 WER from REE enabled micromagnetic simulations

4.3.1 Simulation method and simulated system

The GPU-based micromagnetic simulator MuMax3 [42] was used to carry out the micromagnetic simulations. The parameters of the free magnet were taken to be the same as for the macrospin simulations (Section 4.2.1). The calculated values of thermal stability Δ and the critical current I_{c0} within the macrospin approximation may well be overestimates of the true values for the micromagnetic system, but still can be used as a reference. The grid size was taken to be 1.88 nm in the plane of the FL and 1 nm perpendicular to the plane of the FL. An exchange constant $A_{\mathrm{ex}} = 20$ pJ/m is used. A 10 fs integration step size was used for all the micromagnetic simulations. As for the macrospin trials, the initial population of trial trajectories was thermalized by simulating magnetization dynamics for 5 ns under the influence of thermal fluctuations before the current was applied at $t = 0$. For these micromagnetic REE simulations, as a simple extension of the approach used for the macrospin simulations, the predictor of which trajectories are more likely to lead to rare events than others was taken as $\langle m_z(x, y, t)\rangle$, the spatial average of $m_z(x, y, t)$ normalized to the magnitude of $\langle \mathbf{m}(x, y, t)\rangle$. Then, also as for the macrospin simulations, a threshold value of $\langle m_z(x, y, t)\rangle$, $m_{z,\mathrm{th}}$, was used to identify the rare, slow switching trials.

4.3.2 Results from REE enabled micromagnetic simulations

Figure 4.7(a) illustrates the selection of the threshold $m_{z,\mathrm{th}}$ for the micromagnetic REE simulations similar to Figure 4.5(b), except m_z is now spatially averaged and then normalized. Variation of standard deviation of transit time among 10^3 non-enhanced trials is plotted as a function of $m_{z,\mathrm{th}}$. The inflection points at approximately $m_{z,\mathrm{th}} = 0.95$ for $2I_{\mathrm{c0}}$ and $m_{z,\mathrm{th}} = 0.97$ for $3I_{\mathrm{c0}}$ are selected as the threshold for the respective simulations of WER with REE.

Figures 4.7(b) and (c) show the thus calculated WERs from micromagnetic simulations with REE, exhibiting the ability to calculate WERs down to 10^{-9}, which is where we terminated our simulations, and likely beyond. Macrospin results also are provided

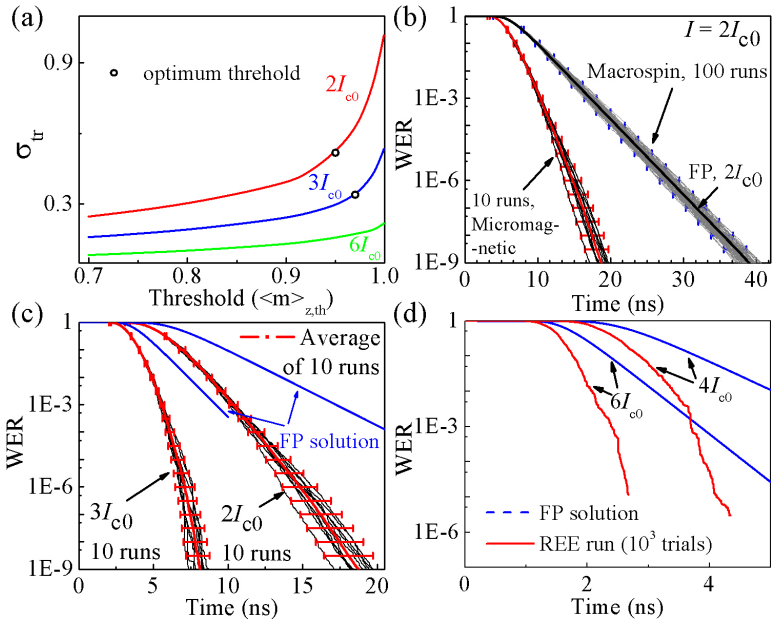

Figure 4.7: WER obtained from micromagnetic simulations with REE. (a) $\sigma_{\rm tr}$ of 10^3 trials as a function of the threshold $m_{z,\rm th}$. The approximate inflection points are marked by the red circles for $I = 2I_{\rm c0}$ and $3I_{\rm c0}$. A well-defined inflection point is not found for $6I_{\rm c0}$. (b) WER calculated using REE for $I = 2I_{\rm c0}$ using a threshold of 0.95 for both micromagnetic and macrospin calculations. (c) 10 independent REE runs with micromagnetic simulations for $I = 2I_{\rm c0}$ ($m_{z,\rm th} = 0.95$) again and of $3I_{\rm c0}$ ($m_{z,\rm th} = 0.97$). Corresponding FP solutions are also shown. The error bars in (b) and (c) indicate plus or minus two times expected standard deviation among the sets of 10^3 trials in the time taken to reach the corresponding WER, calculated using 10 runs (100 runs) for the micromagnetic (macrospin) calculations. (d) WER calculated from REE enhanced micromagnetic simulations at increased applied currents of $I = 4I_{\rm c0}$ and $I = 6I_{\rm c0}$. This figure has been adapted from [158].

for comparison to the micromagnetic results for an applied current of $2I_{\rm c0}$ in (b), while micromagnetic results are provided for applied currents of both $2I_{\rm c0}$ and $3I_{\rm c0}$ in (c). FP results also are supplied for reference. Each of the 10 individual lines for the micromagnetic simulations for each value of applied current represents an independent set of 10^3 simulation trials with REE. The reliability of these WER predictions is illustrated by the $\pm 2\sigma$ (95%) confidence intervals in the time to achieve a given WER based on the variation among the 10 sets. Again, the expected $\pm 2\sigma$ confidence interval for the average result of all 10 sets of trials considered as a whole is smaller by a factor of 3 here. The error bars for the macrospin simulations in Figure 4.7(b) also represent the

$\pm 2\sigma$ confidence interval among independent sets of 10^3 trials, although with 100 sets, as allowed by the much less computationally demanding simulations, as in Section II. The macrospin results again remain consistent with the reference FP results even allowing for the order-of-magnitude smaller confidence interval for all 100 macrospin sets considered as a whole. In absolute terms, the $\pm 2\sigma$ confidence interval is much the same for the micromagnetic and macrospin simulations, although the error in the micromagnetic simulations relative to the average is significantly larger.

For practical applications $3I_{\mathrm{c0}}$ already may be considered a large current [45,170], particularly given that the employed I_{c0} obtained in the macrospin limit may well be an overestimate of the true I_{c0} as previously noted. Nevertheless, it is informative from a modeling perspective to consider what happens as we follow the applied current higher. Figure 4.7(d) shows one REE run each for $I = 4I_{\mathrm{c0}}$ and $I = 6I_{\mathrm{c0}}$. As shown, we were unable to reliably predict WER below $\sim 10^{-6}$ for an applied current of $4I_{\mathrm{c0}}$, and below $\sim 10^{-5}$ for an applied current of $6I_{\mathrm{c0}}$. While well beyond what is otherwise possible to simulate, these WERs may not be sufficient for device applications. There are multiple potential reasons for this limitation. We will only note a few. For larger currents and an associated larger percentage of initial trajectories leading to fast deterministic switching once the current is turned on, the initial distribution of magnetization trajectories may need to be enhanced as well. A more refined predictor than comparison of $\langle m_z(x,y,t)\rangle$ to $m_{z,\mathrm{th}}$ may be possible for micromagnetic simulations. In part, this reduced range of reliable WER predictions behavior is—we have performed test simulation—an artifact of our choosing to hold the number of simulation trials constant in this primary work by waiting to enhance the trials with m_z closer to unity than $m_{z,\mathrm{th}}$ until an equal number of trial had switched, $m_z \leq 0$. If the transit time between $m_{z,\mathrm{th}}$ and switching becomes large compared to the incubation time to reach $m_{z,\mathrm{th}}$, few trial trajectories remain close to unity above $m_{z,\mathrm{th}}$ to enhance, leading to less statistical independence among the rare trial trajectories. Enhancing trials with m_z closer to unity than $m_{z,\mathrm{th}}$ as soon as the number of such trials dropped to one-half the original number alleviates this problem significantly, although leading to somewhat more variability in the number of trials. While results improved we still did not reach 10^{-9} WERs by this approach alone. In addition, for

larger applied currents, shorter time periods between checking the status of the trials is required.

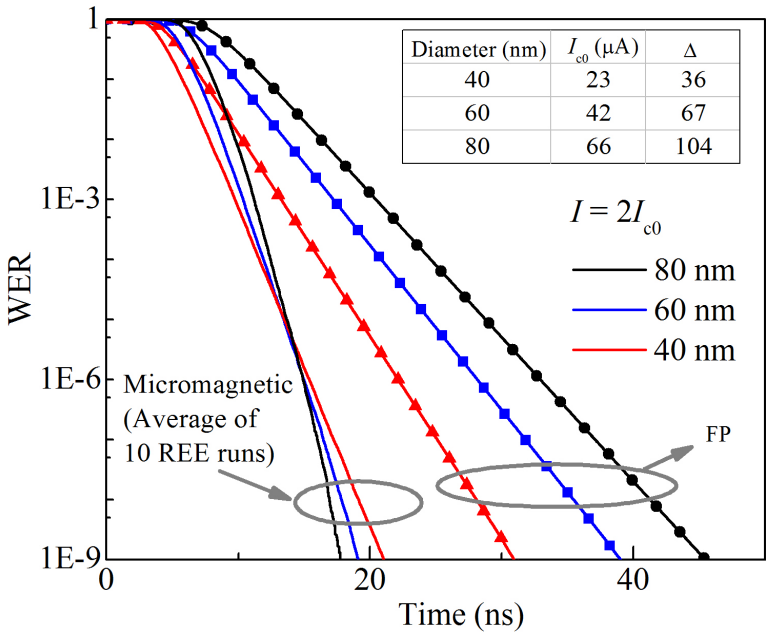

Figure 4.8: WERs of P-STT bits for varying magnet diameters, from macrospin FP calculations and from REE enabled micromagnetic simulations. For each diameter, average of 10 REE runs (each with 10^3 trajectories) has been shown for the micromagnetic result. The applied current for each diameter is twice the corresponding macrospin critical current as noted in the table.

In short, as previously noted, the REE method used here is a basic prototype. Use of improved and more sophisticated REE methods should lead to still more reliable prediction for a given computational effort and allow for still larger applied currents if needed. In other words, even with the already great advantage of REE for simulation of WERs for practical micromagnetic systems demonstrated with the simple approach used here, there remains room to further improve the REE-based calculation of WER in the future.

4.3.3 Variation of WER with magnet diameter

Figure 4.8 shows the variation of WER slopes for circular magnets of diameter 40 nm, 60 nm and 80 nm. All other parameters are taken to be same as in Section 4.3.1

and 4.2.1. The circular magnet is discretized into a $16 \times 16 \times 1$ (for the 40 nm magnet) or $32 \times 32 \times 1$ (for the 60 nm and 80 nm diameter magnets) grid for the micromagnetic simulations. The critical currents I_{c0} for the 40 nm and the 80 nm magnets, obtained within the macrospin approximation, are 22.9 μA and 65.7 μA, respectively. For each diameter the REE calculations has been repeated 10 times for an applied current of $I = 2I_{c0}$. The averages of 10 REE runs are then plotted in Figure 4.8 together with the FP solutions for the three diameters. As is evident form the figure, WER from the REE-enabled micromagnetic simulations are much lower than the FP solution for all three diameters. This deviation is larger for a larger bit. Even for the 40 nm diameter bit, time required to achieve a WER of 10^{-9} considering micromagnetic effects is much shorter than what is expected from the macrospin approximation. For larger bit REE predicted WER decreases with a steeper slope than the smaller bit. The results provide insight into scaling properties of the STTRAM write process, beyond that can be captured by the macrospin approximation.

4.4 Summary

In this chapter, we have focused on the stochastic write process of a P-STT bit. We have developed a relatively simple, prototype REE method tailored to calculation of WER in micromagnetic STTRAM systems, and have demonstrated statistically reliable prediction of WER down to $\sim 10^{-9}$ (representing a simulation choice, not limits of the method) for practical values of applied currents with sample sets of only 10^3 stochastic LLGS-based switching trials. The total number of ongoing stochastic LLGS simulations, the computational burden, is effectively conserved through simulation time. Improved REE methods could be developed based on this work for more reliable prediction of WERs, to lower WERs, and under more extreme switching conditions. REE enabled micromagnetic simulations predicted a much lower WER than that obtained within the macrospin approximation.

Chapter 5

Write error rates of in-plane spin-transfer-torque random access memory

In the previous chapter we focused on the stochastic write process of a perpendicular STTRAM bit. Using a rare-event-enhancement (REE) technique combined with the micromagnetic simulations, we demonstrated calculation of WER to 10^{-9} using only 10^3 micromagnetic simulations. In this chapter we attempt to extend the REE technique toward an in-plane STTRAM bit with elliptic free layer magnets. Although perpendicular magnets are preferred over in-plane ones (see Section 1.2.1), stochastic switching process of an in-plane magnet remains relevant from a modeling perspective as majority of the experimental evidence of incoherent switching affecting WERs used in-plane magnets [154, 155, 171]. There is also a renewed interest towards in-plane magnets as they are more compatible with recently discovered spin-orbit torque switching mechanisms, wherein current driven parallel (vs. perpendicular in a conventional MTJ structure) to the surface of the magnet in an underlying spin-Hall-effect metal [172, 173] or a topological insulator material [174–178] generates a spin-current with spin-polarization direction in the plane of the magnet, perpendicular to the direction of the charge current.

To investigate spatially-incoherent magnetization reversal processes and estimate switching probabilities for in-plane magnets, prior studies employed up to 10^3 independent micromagnetic simulations [157, 179–182]. However, extreme tails of WERs are beyond the scope of such simulations as noted in the previous chapter. In this chapter, we

The results reported in this chapter will be published as a journal article titled (tentative) "Write error rates of in-plane spin-transfer-torque random access memory calculated from rare-event enhanced micromagnetic simulations" by T. Pramanik, U. Roy, P. Jadaun, L. Register, S. Banerjee. The manuscript is under review. Contributions: T. Pramanik developed the codes and ran the simulations with help from U. Roy and P. Jadaun. L. F. Register and S. K. Banerjee supervised the work. T. Pramanik and U. Roy wrote the manuscript. All authors reviewed and commented on the results and the manuscript.

first extend the REE technique to an in-plane STTRAM (I-STT) bit using a predictor of rare events based on the easy-axis magnetization and, to address the oscillatory nature of the switching process for I-STT, time averaging over the natural oscillation period for the hard-axis component of the magnetization. This REE technique allows us to investigate the tails of the WER with increasing switching time, and, thereby, investigate the physical reasons behind the extremely slow switching without incurring a prohibitively large computational expense. Our study finds that, among other things, the extremely slow cases of switching can become dominated by certain types of spatial incoherence in the magnetization, such as vortex (V) and anti-vortex (AV) states. Moreover, once these latter states become dominant, they lead to a reduced slope (magnitude) of the WER vs switching time curve, i.e., a "branching" in the WER characteristics. These V and AV states, not only cannot be captured by macrospin models, of course, but also become problematic to follow to much smaller WERs for the so-far considered REE-enhanced Monte Carlo micromagnetic simulations. Therefore, we further modified the REE method by adding a new predictor of rare events to selectively address these vortices and anti-vortices based on what is called the "topological charge" or "skyrmion number," which then allows for reliable REE-enhanced prediction of WERs to the lowest considered values of 10^{-9} for all considered currents.

5.1 REE technique for in-plane STTRAM bits

5.1.1 Details of the simulated bit

Figure 5.1(a) shows a magnetic tunnel junction (MTJ) with a free layer (FL) and a reference layer (RL) magnet patterned in an elliptic shape, as used for an I-STT bit. Switching from the parallel state to the anti-parallel state is considered. Only the FL is included in our simulations assuming the RL acts only as a source of spin-polarized current that flows along the surface-normal direction (z-axis) of the free layer. The FL is assumed to have a major axis of 150 nm along the x-axis, a minor axis of 50 nm along the y-axis and a thickness of 2 nm along the z-axis. A saturation magnetization $M_{\rm s} = 0.8 \times 10^6$ A/m and a Gilbert damping constant $\alpha = 0.01$ were used. The spin-

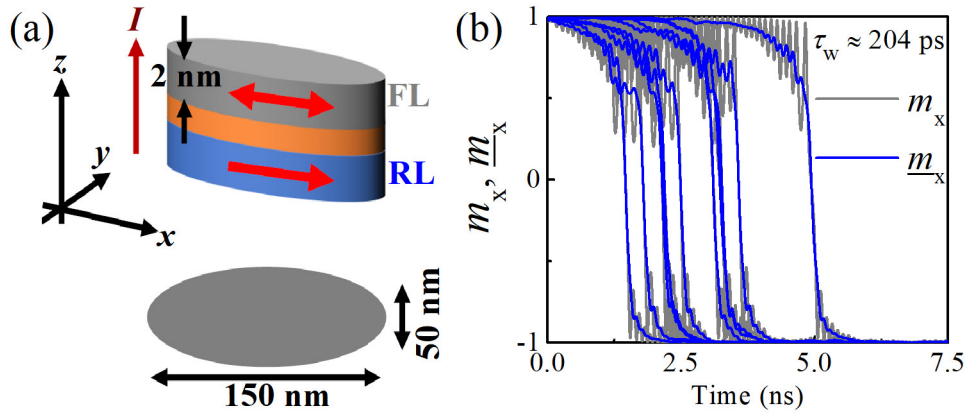

Figure 5.1: (a) MTJ with elliptic free layer (FL) and reference layer (RL) magnets, as used in a typical I-STT cell. Magnetization dynamics of FL will be considered. Axes convention, direction of current flow and lateral dimensions of the FL are marked. (b) Example magnetization trajectories, m_x, and corresponding filtered trajectories, $\underline{m}_x$, obtained from macrospin stochastic LLGS simulations of the STT-induced switching of the FL magnet.

polarization direction, $\bar{m}_{\rm p}$, of the current is along the $+x$ direction with a spin polarization factor $\eta = 0.4$. Field-like torque has not been considered. Assuming a rectangle of same lateral dimensions as the elliptic bit, demagnetization factors of the FL magnet are estimated to be $N_{\rm xx} = 0.0181$, $N_{\rm yy} = 0.0562$ and $N_{\rm zz} = 0.9257$ [43]. Temperature is set to $T = 300$ K for all simulations. Within the macrospin limit, with the above set of parameters, the thermal stability factor of the I-STT bit (calculated from Equation 1.12) is $\Delta = 43.7$ and the critical current of STT switching (calculated from Equation 1.14) is $I_{\rm c0} = 0.34$ mA. As for the P-STT bit in the previous chapter, the stochastic LLGS equation (Equation 4.1) is then integrated with a time step of 0.1 ps using the scheme of Heun [161] for all the macrospin simulations. Initial ($t = 0$) equilibrium thermal distributions of $\vec{m}(t)$ are obtained by starting with $m_x = 1$ and integrating the stochastic LLGS equation for 5 ns without STT.

5.1.2 Modified REE technique

The basic idea remains the same as described in Section 4.2.2 for a perpendicular magnet. Again, the first requirement is to choose a predictor of which trajectories, $\vec{m}(t)$,

are more likely to lead to rare events than others. For a P-STT bit, the state of the bit is well characterized by the surface-normal component of magnetization unit vector, m_z, and hence m_z was used as the predictor to identify rare trials. Similarly, for an I-STT bit, we choose m_x, the component of magnetization unit vector along the in-plane easy axis, as the predictor. Due to the axial symmetry of a circular P-STT bit, m_z varies monotonically (except small fluctuations due to random thermal field) from the initial state ($m_z \approx +1$) toward the final state ($m_z \approx -1$) during switching. In case of an elliptic I-STT bit, m_x switches from the initial state ($m_x \approx$ +1) to the final state ($m_x \approx -1$) via large pre-switching oscillations, as shown by the grey trajectories in Figure 5.1(b). At any time, t, the state of the trajectory may not be obvious from the instantaneous value of the predictor m_x. To substantially resolve this issue, m_x is filtered via a moving average over a time window (τ_{w}). τ_{w} is taken as the oscillation period of the strongest frequency component present in the pre-switching small-amplitude oscillations of m_y, the component of magnetization along the in-plane hard axis. Within the macrospin approximation, e.g., this frequency is found to be the same as the frequency of the uniform mode given by Kittel's formula [183]. As shown in Figure 5.1(b) (blue trajectories), pre-switching oscillations are strongly suppressed in the time averaged trajectories, $\underline{m}_x$, making it suitable for use as a predictor. The suppression is not perfect because the oscillation period can vary for large oscillations.

Figure 5.2 depicts the REE technique with the help of a few sample macrospin trajectories of $\underline{m}_x$ (T1-T5) for visual clarity. Total simulation time is subdivided into smaller intervals. These intervals are terminated at times $\{t_1, t_2, t_3, ...\}$ that are decided on the fly such that the number of trajectories that have switched ($\underline{m}_x < 0$) are approximately equal to the number of trajectories that have $\underline{m}_x$ greater than a predetermined threshold, $\underline{m}_{x,\mathrm{th}}$ (0.8 in Figure 5.2) (with again $m_x = 1$ corresponding to the ideal initial state). Then, at the beginning of the next interval, trajectories above the threshold (e.g., T1 at time t_1 in Figure 5.2) are split into two offspring trajectories each with half the weight of the parent trajectory. Trajectories that have switched (e.g., T4, T5 at time t_1) are discontinued and trajectories with $0 \leq \underline{m}_x \leq \underline{m}_{x,\mathrm{th}}$ (e.g., T2, T3 at time t_1) are continued without any splitting. This process is repeated at subsequent time intervals. Note that to

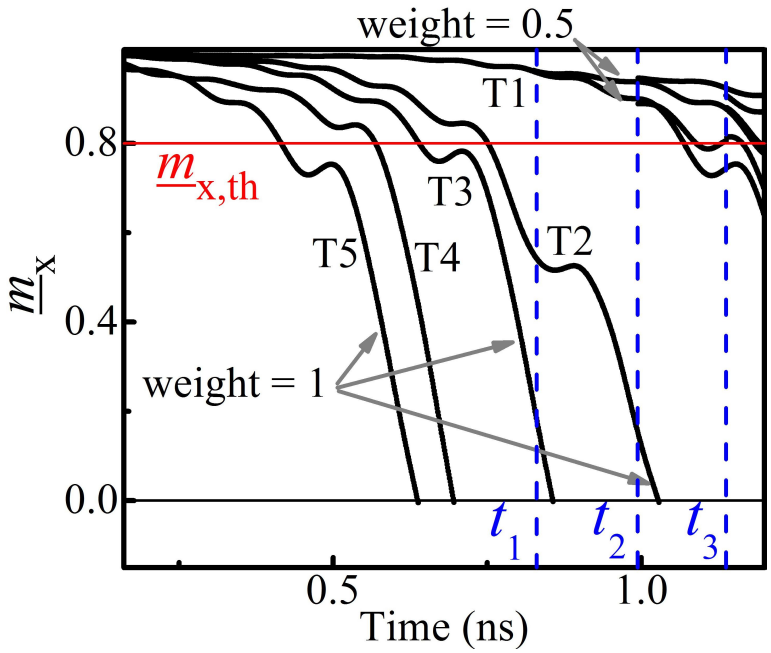

Figure 5.2: Illustration of the splitting technique of REE for stochastic LLGS trajectories of $\underline{m}_x$ at discrete times $= t_1$, t_2, t_3 etc. Switching current is applied at $t = 0$ ns on a thermalized distribution with m_x close to unity. The threshold, $\underline{m}_{x,\mathrm{th}} = 0.8$ in this example, is marked by the red horizontal line.

obtain the filtered value $\underline{m}_x$ at any given time instant, for example t_l, the simulation must be continued until $t_\mathrm{l} + t_\mathrm{d}$, where $t_\mathrm{d} = \tau_\mathrm{w}/2$. For all REE simulations, 10^3 independent trials, each assigned a weight of 1, are considered at $t = 0$. Including the weighting of all continued and switched (terminated) trajectories derived from these 10^3 trials, the total weighting remains conserved at 10^3 throughout the simulation time. Hence, the WER is estimated as:

$$\mathrm{WER}(t) = \frac{1}{10^3} \sum_{\mathrm{not-switched}} \mathrm{weight}. \tag{5.1}$$

Previous studies of I-STT bits showed the presence of magnetization trajectories that may return to the initial state even after an apparently successful switching [184–186]. To identify such cases, trajectories with $\underline{m}_x < 0$ are simulated for a short additional time (1 ns for macrospin simulations, 0.5 ns for micromagnetic simulations) unless they settle down with $\underline{m}_x \leq -0.95$. If a trajectory returns above $\underline{m}_x > 0$ during this time period, we place it back in the unswitched population and follow it as any other

unswitched trajectory. (We note that by this procedure, until such paths are eliminated as switched or the enhancement time interval is reached, they add to the otherwise conserved number of paths. However, a subsequent modification to be discussed in Section 5.3.2 then essentially eliminates this overhead.) However, for the macrospin simulations, only few such trajectories were encountered and no noticeable change of the WER was observed from the case when this additional simulation time was not considered (i.e., all trajectories with $\underline{m}_x < 0$ were immediately declared switched and hence their simulations were stopped). For micromagnetic simulations, as will be discussed in the later sections, the number of such trajectories increased considerably at higher applied currents leading to a change in the WER slope.

5.1.3 Results of REE within the macrospin approximation

Again, as for the perpendicular magnet in the previous chapter, we calculate the WER for the in-plane magnet in the macrospin limit to verify the correctness of the technique. However, for an in-plane magnet as the one considered here, one needs to solve full two-dimensional Fokker-Planck equation (Equation 4.2). Instead, the REE estimated WER in the macrospin limit will be compared with WER calculated from 10^5 independent macrospin LLGS simulations (without any enhancement).

To identify the optimum thresholds we followed the method as in the previous chapter (see Section 4.2.3). First, 10^3 trajectories are simulated without REE for each applied current of interest. Then, transit times ($\tau_{\rm tr}$) for each of 10^3 filtered (using the moving average filter as discussed earlier) trajectories are calculated for a given choice of threshold $\underline{m}_{x,\rm th}$. The definitions used for the transit ($\tau_{\rm tr}$) and incubation ($\tau_{\rm in}$) times are shown in Figure 5.3(a) inset. The standard deviation of transit times ($\sigma_{\rm tr}$), shown in Figure 5.3(a), increases with increased $\underline{m}_{x,\rm th}$. The inflection points on these curves are then considered to be reasonably optimal choices for $\underline{m}_{x,\rm th}$.

To illustrate proposed REE scheme and its correctness, we compare the results of REE predicted WER to those obtained from 10^5 independent LLGS simulations without REE. Results are shown in Figure 5.3(b) for applied currents of $I = 1.5I_{\rm c0}$, $2I_{\rm c0}$, $3I_{\rm c0}$

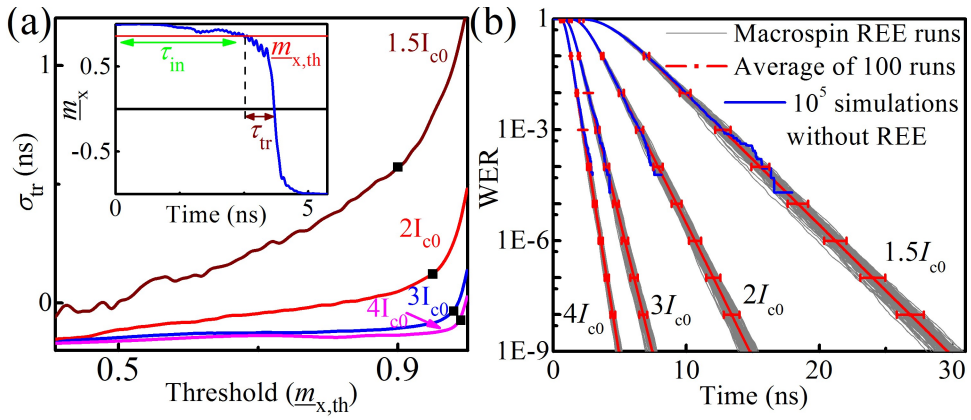

Figure 5.3: WER from REE enhanced macrospin simulations: (a) Variation of the standard deviation of the transit time ($\sigma_{\rm tr}$) of 10^3 macrospin trajectories without REE. Inflection points, marked by black squares on each line, depict the optimal values of the threshold, $\underline{m}_{x,\rm th}$. Definition of transit times ($\tau_{\rm tr}$) and incubation times ($\tau_{\rm in}$) are shown in the inset. (b) WER estimated from REE within macrospin approximation. Thin grey lines for each applied current are results of independent REE runs each with 10^3 trajectories. The average of the 100 such REE runs (thick red lines) and the $\pm 2\sigma$ confidence interval (error bars) for individual REE sets also are shown. The thick blue lines are from 10^5 independent LLGS simulations without REE.

and $4I_{\rm c0}$. For each applied current, REE calculation employing with 10^3 trials each, are performed 100 times (thin gray lines in Figure 5.3(b)), using the optimum thresholds chosen from Figure 5.3(a). Figure 5.3(b) also shows the average (thick red line) of all 100 REE runs, along with error bars representing a plus or minus two standard deviations $\pm 2\sigma$ (95%) confidence interval for the individual runs based on the variation among the 100 independent runs. This average WER from the all REE-enhanced stochastic LLGS trials and that from the 10^5 non-enhanced LLGS trials are consistent, until (as expected) the latter could not be continued any beyond (or accurately to) 10^{-5}, with all non-enhanced trials having switched.

Figure 5.4 shows a few examples of rare macrospin trajectories from the REE simulations for two different applied currents. As is evident, for each case, the magnetization remained confined within a narrow zone close to $m_x = 1$ until just before switching. This initial phase could be understood as the incubation phase. The term "incubation" was used in previous studies to denote the initial "non-reactive" time duration after applying

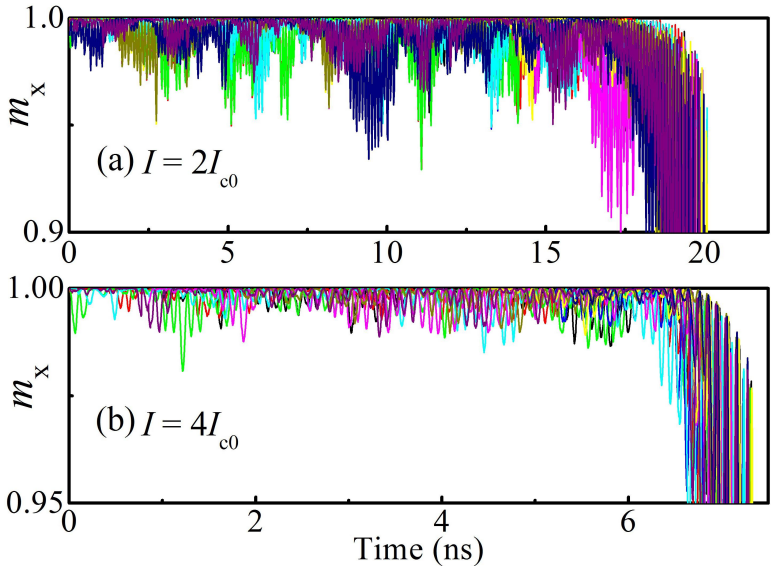

Figure 5.4: Examples of rare macrospin trajectories of m_x (each color is one trajectory), with extremely long switching times, for (a) $I = 2I_{c0}$ and (b) $I = 4I_{c0}$. 10 trajectories are plotted together for each current. Magnetization remained confined within a narrow "incubation zone" until very close to the switching time.

the current pulse, when magnetization of the free layer does not show any appreciable deviation from the equilibrium state [167, 187, 188]. Within a macrospin picture an incubation delay is attributed to the vanishing strength of the STT term in the LLGS equation in the limit of collinear magnetization of the FL and the RL magnets ($\bar{m}_{\rm p} \times \bar{m} = 0$ in Equation 4.1) [51, 189]. During this time, thermal field may help the magnetization to escape from the incubation phase or may push the magnetization back into the incubation. This stochastic nature of the escape mechanism is the sole source of rare events within the macrospin approximation. Figure 5.4 also reveals that with increasing STT strength, the boundary of this incubation phase is pushed toward $m_x = 1$, which is consistent with higher optimum threshold, $\underline{m}_{x,\rm th}$, at higher applied currents. Once out of the incubation phase, the magnetization switched very quickly, following rather deterministic paths.

5.2 REE with micromagnetic simulations

Micromagnetic simulations were carried out using MuMax3 [42]. The dimensions and material parameters of the simulated magnet are same as for the macrospin sim-

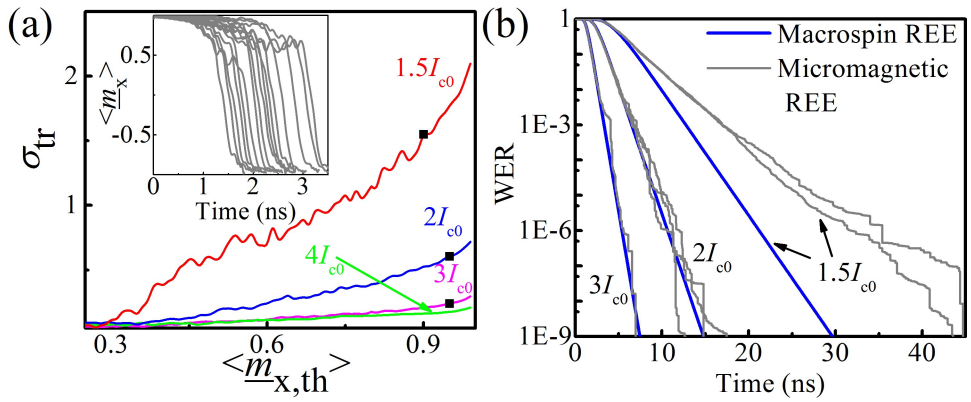

Figure 5.5: REE with micromagnetic simulations: (a) Variations of $\sigma_{\rm tr}$ with choice of threshold $\langle m_{x,\rm th} \rangle$ computed from 10^3 non-enhanced trajectories. Inset shows a few example trajectories of space averaged, normalized and filtered magnetization, $\langle m_x \rangle$ from the micromagnetic simulations. (b) WER estimated from REE enabled micromagnetic simulations. Thin grey lines for each applied current are results of independent REE runs each with 10^3 trajectories. Thresholds picked from (a) (black dots) have been used for REE runs in (b). Step-like artifacts in (b) point to room for improvement in the choice of threshold. Blue lines are the average WER obtained from 100 macrospin REE runs shown in Figure 5.3(b).

ulations. The elliptic FL magnet is discretized into a simulation grid of $64 \times 32 \times 1$ cells. An exchange stiffness $A_{\rm ex} = 20$ pJ/m is used. The Heun solver has been chosen with an integration step size of 10 fs for all the micromagnetic simulations. The initial population of magnetization is prepared by simulating magnetization dynamics under thermal fluctuation (without the STT term) for 5 ns starting from a state uniformly magnetized along the $+x$ direction. For micromagnetic simulations, to determine the predictor of which trajectories are more likely to lead to rare events, the following method is adopted. First, the spatial-average of magnetization, $m_x(x, y, t)$, $\langle m_x \rangle$, is normalized to the magnitude of the spatial-average of $\vec{m}(x, y, t)$. This normalized quantity is then filtered via a moving average over a time window ($\tau_{\rm w}$) that is calculated as for the macrospin REE simulations. The filtered quantity $\langle m_x \rangle$ is now used as the predictor in the REE simulations.

Standard deviation of transit times ($\sigma_{\rm tr}$) computed from 10^3 non-enhanced micromagnetic simulations are plotted in Figure 5.5(a) as a function of the threshold, $\langle m_{x,\rm th} \rangle$. Figure 5.5(a) inset shows a few example trajectories of $\langle m_x \rangle$. As can be seen, inflection points are hard to identify here, unlike the macrospin counterpart in Figure 5.3(a). Nev-

ertheless, one can still pick the approximate inflection points (marked by black squares) as initial estimates for thresholds. Figure 5.5(b) shows WERs from REE-enabled micromagnetic simulations with thresholds, $\underline{\langle m_{x,\mathrm{th}} \rangle}$, picked from Figure 5.5(a) for applied currents of $I = 1.5I_{\mathrm{c0}}$, $2I_{\mathrm{c0}}$ and $3I_{\mathrm{c0}}$. Subsequent presence of step-like artifacts in the WER vs. time results suggest room-for-improvement in the choice of threshold. Such steps are found to result from trajectories that fail to switch for periods long compared to the nominal transit time, but have predictor ($\underline{\langle m_x \rangle}$) value lower than the chosen thresholds and, thus, continue without splitting through many enhancement windows. Hence, these trajectories maintain a large weight and create a sharp decrease of the WER when they switch. For P-STT [158], such steps could be avoided by lowering the threshold (also explained in Section 4.2.3). Figure 5.6 shows improved results with lower thresholds ($\underline{\langle m_{x,\mathrm{th}} \rangle}$): 0.8 for $I = 1.5I_{\mathrm{c0}}$ and $2I_{\mathrm{c0}}$, 0.4 for $I = 3I_{\mathrm{c0}}$, 0.2 for $I = 4I_{\mathrm{c0}}$ and $6I_{\mathrm{c0}}$. However, increased variability and step-like features below WER $= 10^{-6}$ could not be avoided for $I = 3I_{\mathrm{c0}}$ (Figure 5.6(a)). These features became much stronger and appeared at even higher WER (below 10^{-3}) for $I = 4I_{\mathrm{c0}}$ and $6I_{\mathrm{c0}}$, as shown in Figure 5.6(b).

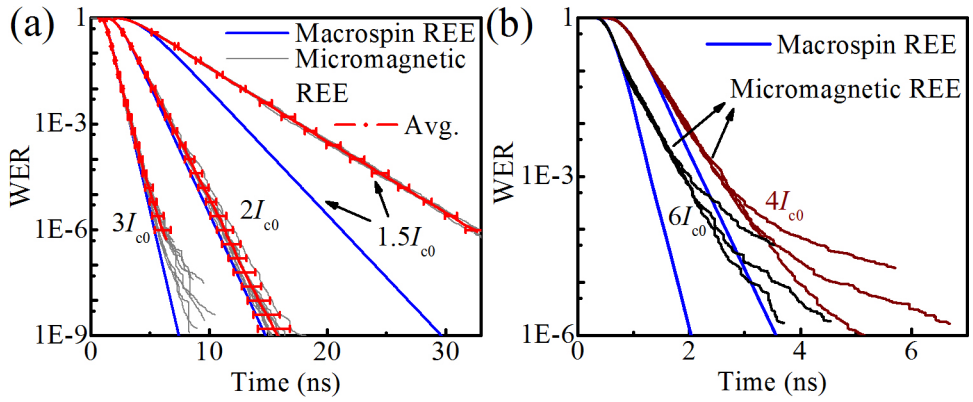

Figure 5.6: REE with micromagnetic simulations, with lowered threshold: (a) $I = 1.5I_{\mathrm{c0}}, 2I_{\mathrm{c0}}$ and $3I_{\mathrm{c0}}$, (b) $I = 4I_{\mathrm{c0}}$ and $6I_{\mathrm{c0}}$. Thin gray lines for each current are results of independent REE runs each with 10^3 trajectories. The red curves show the average of 10 REE runs for $2I_{\mathrm{c0}}$, $3I_{\mathrm{c0}}$ and 5 REE runs for $1.5I_{\mathrm{c0}}$. The error bars represent $\pm 2\sigma$ confidence interval for the individual runs of 10^3 trials based on the variation among the runs. WERs for $I = 4I_{\mathrm{c0}}$ and $6I_{\mathrm{c0}}$, repeated 3 times for each applied current, show a change of slope and large variation among the individual runs at lower WER. Blue lines are the average WER obtained from 100 macrospin REE runs shown in Figure 5.3(b).

In Figure 5.6(a), the REE runs for $I = 1.5I_{c0}$ have been repeated 5 times each with 10^3 trials and terminated after WER $< 10^{-6}$ due to constraints on simulation time. For $I = 2I_{c0}$ and $3I_{c0}$, REE runs have been repeated 10 times each with 10^3 trials. Average of these individual REE runs for each applied current is also plotted. The reliability of these WER predictions again is illustrated by the $\pm 2\sigma$ (95%) confidence intervals for the individual runs in the time to achieve a given WER, based on the variation among the individual runs of 10^3 trajectories.

For $I = 4I_{c0}$ and $6I_{c0}$, REE runs have been repeated 3 times [Figure 5.6(b)]. In each case, a change of slope is observed in the WER at the tail of these curves (below WER $= 10^{-3}$). Around this point, we have terminated these runs as the results could be unreliable. This change of slope is also found to be correlated with an increasing number of trajectories switching back toward the initial state after $\underline{\langle m_x \rangle}$ reached zero, which in macrospin simulations was a reliable predictor of successful switching. As discussed in the next section, such trajectories emerged from the excitation of vortices or anti-vortices. At higher applied currents and lower WERs, number of such trajectories increased rapidly, leading to a change in WER slopes as well as a large variation of WER among the individual REE sets.

Macrospin WERs shown in Figure 5.6(a)-(b) are the averages of 100 REE runs [same as shown in Figure 5.3(b)]. Micromagnetic simulations predicted higher WERs than the macrospin case for this I-STT bit. As discussed in the next section, this increased WER is a result of different spatially-incoherent excitations that impede STT switching. At lower currents (e.g., $I = 1.5I_{c0}$) the end mode dominates, causing delayed switching and higher-than-macrospin WER. This mode is presumably suppressed at higher currents ($I = 2I_{c0}$ and $I = 3I_{c0}$) leading to a WER slope close to the macrospin ones. However, at even higher currents, vortex or anti-vortex like states are excited, leading to a change in the WER slope.

5.3 Excitation and modeling of end mode, vortex, and anti-vortex magnetization states during switching

5.3.1 Switching via end mode, vortex, and anti-vortex magnetization states

Lower values of thresholds required for the micromagnetic simulations suggest that the mechanism that slows down (or keeps in an "incubation" phase) some of the trajectories is different for these micromagnetic simulations than the macrospin case. As explained in Section II, the vanishing strength of STT in the limit of collinear magnetization of the FL and RL magnets gives rise to the incubation phase and acts as a source of rare events in the macrospin magnetization dynamics. Within the micromagnetic framework, such an incubation effect is expected to be weakened as the local magnetization vector is now allowed to deviate significantly from a collinear orientation and initiate the STT switching. However, another effect observed in micromagnetic simulations is that the current-induced non-uniform magnetization states may keep the free layer locked into trajectories that are not favorable for switching, resulting in an effective incubation-like delay. Existence of non-uniform switching modes and metastable excitations, such as so called "C-states", named after the shape of the magnetization profile, and vortices, are well known for I-STT bits [171, 179, 181, 186, 190–195]. Such spatially-incoherent switching modes are also known to cause prolonged switching delays [179,190,196,197]. Here, we find that combined action of STT and thermal fluctuation could push the free layer into these non-uniform magnetization states. Similar to the incubation phase in the macrospin case, escape from such trajectories is then strongly influenced by thermal fluctuations. Hence, these excitations of spatially-incoherent states now act as a source of rare events in micromagnetic WER simulations. Average magnetization of such a non-uniform state is much lower than the average magnetization of the initial equilibrium state ($\langle m_x \rangle \approx 1$). Hence lower thresholds are required to capture these trajectories.

To visualize these states, we selected the magnetization trajectories that remained unswitched for extremely long times (e.g., trajectories that switched when WER is below 10^{-6}) and traced their dynamics back all the way till $t = 0$. These trajectories are expected to have avoided switching through many enhancement windows and thus, should depict the incubation phases of interest.

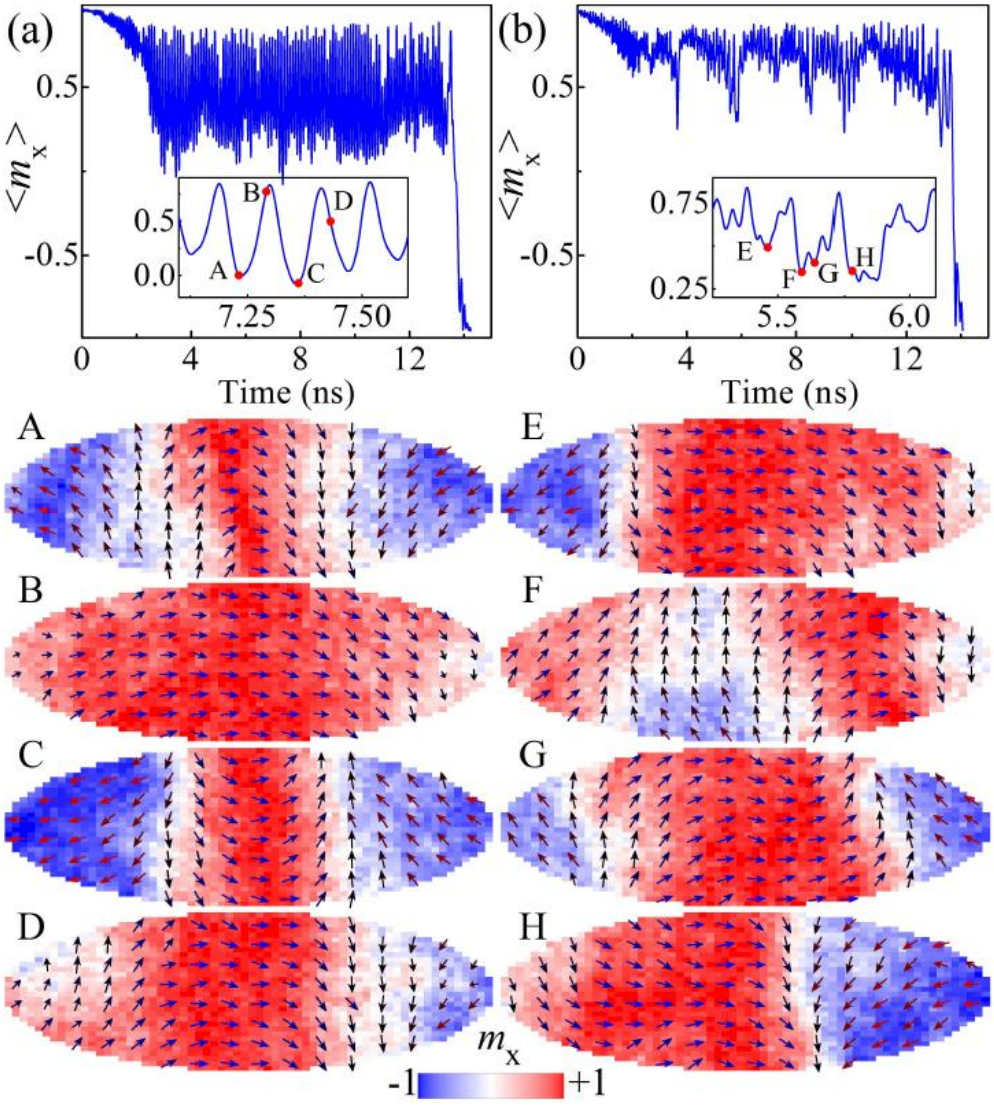

Figure 5.7: Example rare trajectories for $I = 2I_{c0}$. Average magnetization m_x in (a) shows persistent oscillations. A-D show magnetization snapshots at time instants marked with red dots on the inset in (a). (b) shows another type of fluctuation. E-H show magnetization snapshots at time instants marked with red dots on the inset in (b). All snapshots follow the same color map shown at the bottom of the figure.

Figure 5.7 shows two rare trajectories for $I = 2I_{c0}$. It can be easily recognized that these rare trajectories from micromagnetic simulations are quite different from the ones shown in Figure 5.4 from macrospin simulations. In Figure 5.7(a), the average magnetization shows large fluctuations centered at $\langle m_x \rangle \approx 0.5$ for a prolonged interval before switching. As seen from the inset, this fluctuation is rather periodic. Magnetization snapshots (shown in Figure 5.7(A-D)) at a few time instants along the trajectory reveal repeated excitation of end domains (blue domains in Figure 5.7(A,C)). Such precession has been shown to be related to the end mode with out-of-phase precession at the opposite ends of the ellipse [182, 190, 194]. The central domain (red domains in Figure 5.7(A, C)) in these states are very similar to C-states reported in Refs. [171, 192, 193]. These trajectories could also explain the existence of intermediate states that are far from the equilibrium states (although closer to the initial state in terms of spatially averaged m_x) and the random waiting times before switching, as described in [188]. Figure 5.7(b) shows another type of excitation with little or no periodicity in the magnetization trajectory that results from the end mode combined with other higher order modes. Trajectories (not shown) are also observed where excitations like Figure 5.7(a) transformed into the one in Figure 5.7(b) or vice versa. These types of trajectories dominate the unswitched population for $I = 2I_{c0}$ and $1.5I_{c0}$ giving rise to a WER higher than the macrospin WER, as shown in Figure 5.6(a).

With increased applied current, along with the end mode (like Figure 5.7(A-D)), vortex (V) or anti-vortex (AV) like excitations also arise. An example trajectory for $I = 3I_{c0}$ with magnetization distribution at selected times are shown in Figure 5.8. As shown in Figure 5.8(A), two end domains approaching each other from both sides may result in a vortex core moving into the magnet. Once inside, the vortex core rotates along the periphery of the magnet (Figure 5.8(B-E)), altering it's circulation (rotation of the in-plane magnetization around the vortex core) at the two ends of the ellipse (clockwise in B, F, counterclockwise in D, E). Such rotations can survive for a long time (e.g., from E to F). A very similar rotational motion is also observed for AV cores as shown in Figure 5.8(G-L). With the AV core moving along the periphery of the magnet, it can drag a domain wall (Figure 5.8(J)) along with it, causing sharp jumps (~ 3.8 ns in the right inset) in

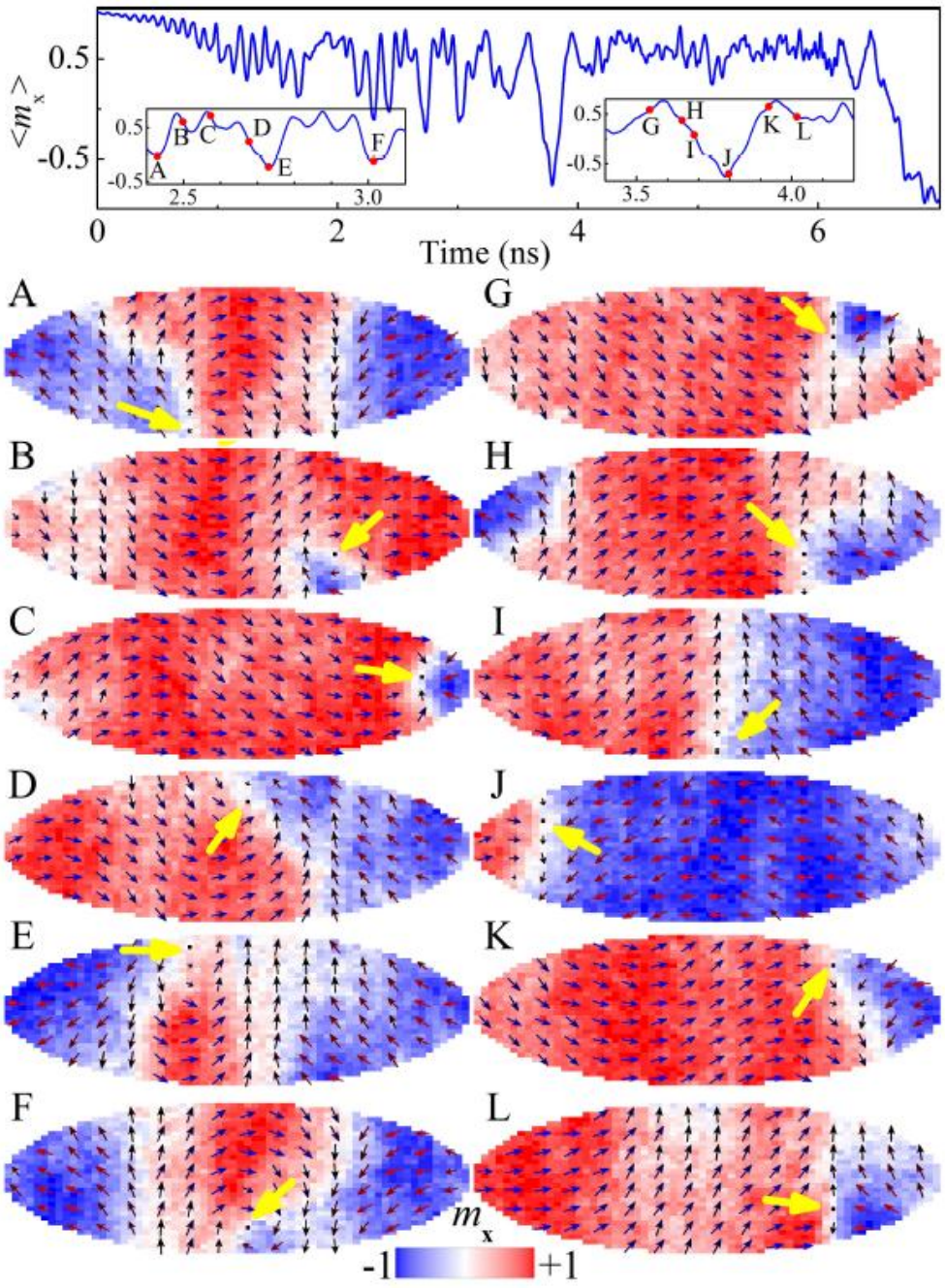

Figure 5.8: Magnetization dynamics of a rare trajectory for $I = 3I_{c0}$. Magnetization snapshots (A-L) shows two different type of excitations. In A-F (time instants marked with red dots on the left inset), a vortex is observed to be rotating around the edge. In G-L (times marked with red dots on the right inset), an anti-vortex is observed to be rotating around the edge. All snapshots follow the same color map shown at the bottom of the figure. Yellow arrows point to the core of the vortex or anti-vortex.

the average magnetization while preventing successful switching. Rotating vortex cores has been observed previously in experiments studying STT-induced dynamics of in-plane magnets [193, 198]. However, rotation of AV cores has not been studied so far in detail.

In an even rarer scenario, the V or AV core is forced to move closer to the center of the ellipse. Such trajectories are observed only below WER $= 10^{-6}$ for $I = 3I_{c0}$. They become more frequent when the applied current is increased to $I = 4I_{c0}$ and $I = 6I_{c0}$, presumably due to the additional energy being supplied by STT. Two such trajectories are depicted in Figure 5.9(a) and 5.9(b) showing an AV and a V, respectively. For both cases, the magnetization dynamics become quite slow (compared to the rapid fluctuations due to domain walls as in Figure 5.7) and the average magnetization remains between the two equilibrium states. Hence even lower thresholds are required to capture these rare events. Once the core of the V or AV reaches the center of the ellipse, the core movement completely controls the magnetization dynamics (unlike Figure 5.8 where the end mode seems to be present while the core continues to rotate). The V or AV core at the center can protect a small unswitched domain (e.g., 5.9(E, K, L)) and prevent complete switching. As shown in Figure 5.9(a), one of the two offspring of the initial trajectory switched by pushing the AV toward the edge (5.9F), while the other failed to switch. Interestingly, behavior of such trajectories reminds one of the experimentally well-known back-hopping phenomenon [184], although the time scales of these events are much shorter in our case (e.g., $<$ 10 ns, whereas back-hopping was observed in longer timescales of ~ 100 ns or more in the experiment). Due to the prolonged lifetime and repeated "back-hopping" of such states, the unswitched fraction increases and a change of slope in the WER is observed (see Figure 5.6(b)). Increased WER due to V/AV excitations also agrees well with Ref. [179], where presence of vortices resulted in reduced and non-monotonic variation of switching probabilities over time. Intermediate states with resistances halfway from the equilibrium states were also observed previously in many experiments [186, 191, 195]. Time evolution of intermediate states observed by Aoki et al. [195] and Heindl et al. [186], are quite similar to the ones in Figure 5.9(a) and (b).

Presence of an AV near a V with opposite core polarization may result in their collision and formation of a Bloch point [199, 200]. A Bloch point is a singularity in

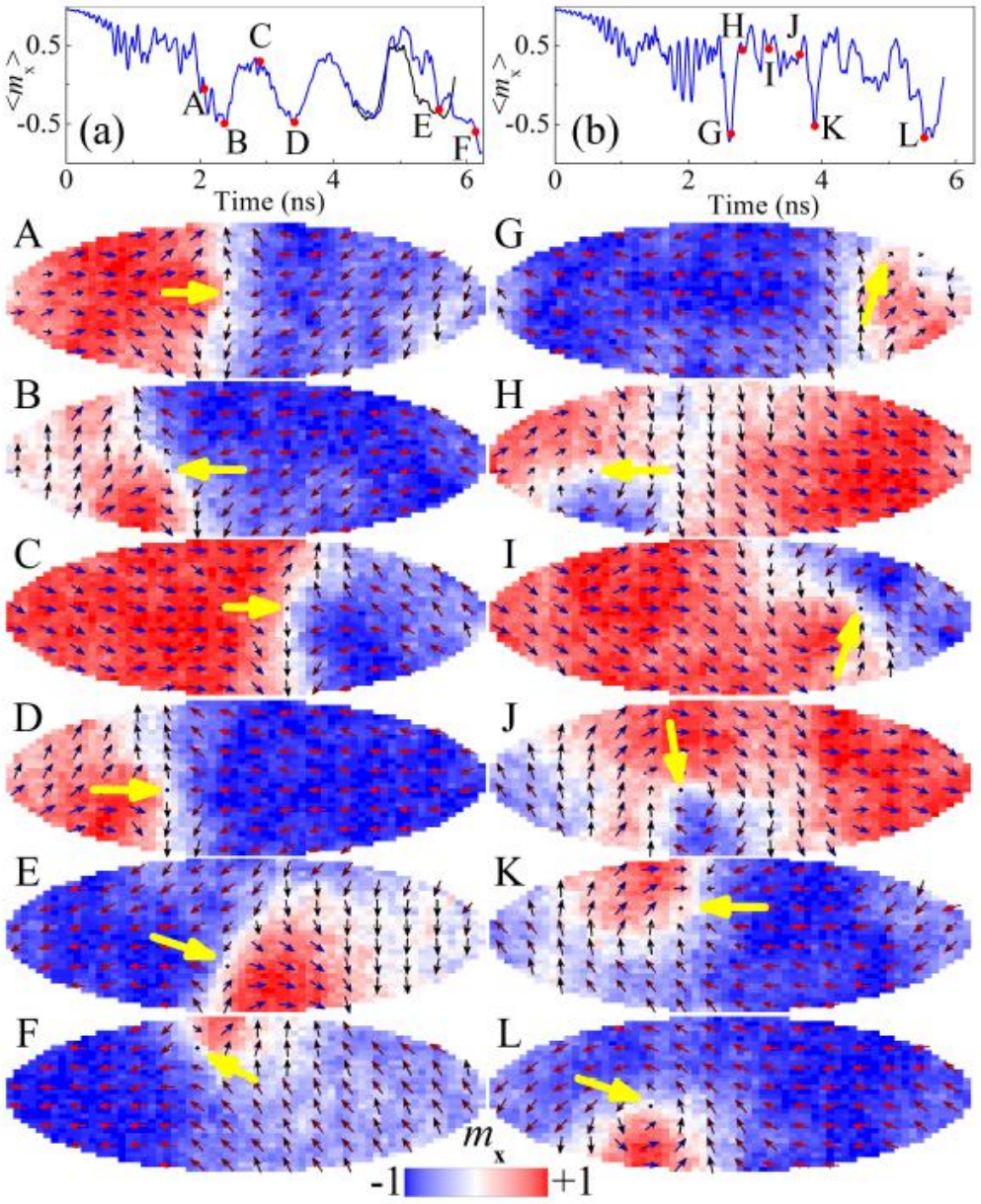

Figure 5.9: Example rare trajectories for $I = 4I_{c0}$. (a) Trajectory with a near periodic variation of $\langle m_x \rangle$ over time and repeated "back-hopping". Magnetization snapshots A-F (times marked with red dots on (a)) show excitation of an anti-vortex that moves close to the center of the elliptical magnet. One offspring (black line in (a)) failed to switch at 6 ns while the other offspring (blue line) switched by pushing the anti-vortex core out of the magnet. (b) Trajectory with a vortex excitation. Snapshots G-L (times marked with red dots on (b)) show the formation and movement of the vortex core. All snapshots follow the same color map shown at the bottom of the figure. Yellow arrows point to the core of the vortex or anti-vortex.

the ferromagnet with vanishing magnetization at the center that violates the assumption of constant magnetization magnitude commonly used in micromagnetic simulators including that used here. Evolution of a Bloch point during STT switching of an in-plane magnet has been reported previously [201]. Although, micromagnetic simulations with fine 3D meshing have been used in prior studies to investigate Bloch point structures, the simulation results could still remain grid size dependent [200, 202]. A finer mesh, in our case, also requires a much smaller integration time step demanding a formidable amount of computation even with the REE technique. Nonetheless, we have verified that test simulations with a finer grid and smaller integration time step reproduced the essential features observed here, without significantly affecting the quantitative results.

5.3.2 Detection and enhancement of trajectories with vortex and anti-vortex states

The large variability among individual REE runs at higher currents (Figure 5.6(b)) presumably results from a poor choice of threshold and/or enhancement technique. The "rare" trajectories of interest at higher applied currents, such as the ones in Figure 6, are confined around $\langle m_x \rangle \sim 0$, making them difficult to detect with a scheme guided by a macrospin-like threshold selection (see Figure 5.3(a) and 5.5(a)). A better approach would be to detect and enhance trajectories like Figure 5.9 using their integrated "topological charge", or "skyrmion number" Q, defined as,

$$Q \equiv \frac{1}{4\pi} \iint \vec{m} \cdot (\frac{\partial \vec{m}}{\partial x} \times \frac{\partial \vec{m}}{\partial y}) dx dy, \tag{5.2}$$

where, $\vec{m}$ is the space-varying magnetization unit vector [203]. For a V or AV, the above integral results in $\pm$ 0.5 depending on the core polarization and the winding number (in-plane rotation direction of the magnetic moments around the core). For quasi-uniform magnetizations $Q \approx 0$. Numerical evaluation of the above integral enables one to detect existence of topological textures within the magnet. Therefore, we now propose a modified REE scheme also making use of the quantity Q, combined with the continuing use of $\underline{\langle m_x \rangle}$.

To quantify the number of trajectories with excitations like Figure 5.9(a) or (b), the histograms of Q numbers are obtained at the end of each enhancement window (e.g.,

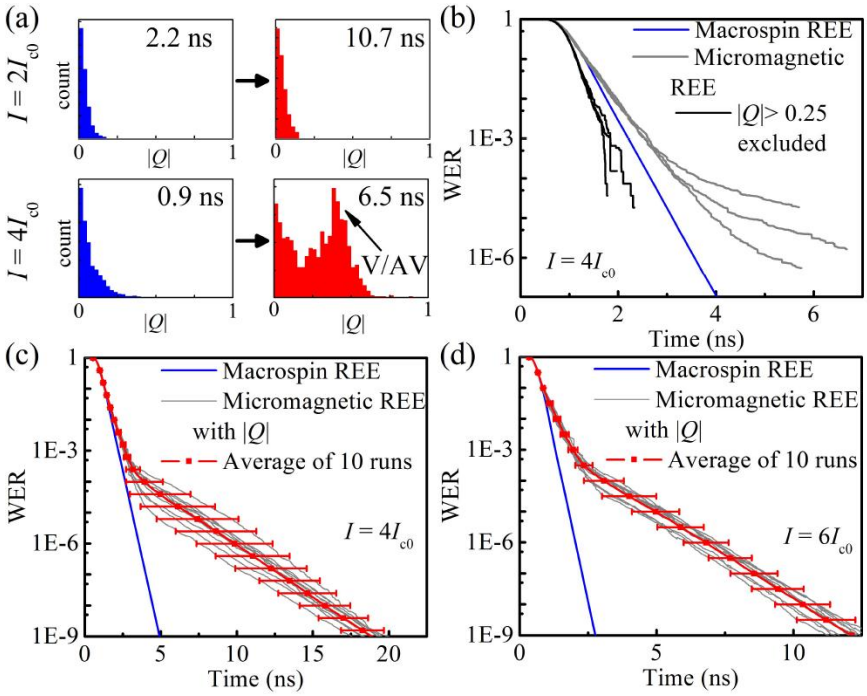

Figure 5.10: Modified REE technique based on the integrated topological charge Q within the magnet. (a) Histograms of $|Q|$ for $I = 2I_{c0}$ and $4I_{c0}$ at two different time instants show growing population near $|Q| \sim 0.4$ for $I = 4I_{c0}$ which is absent for $I = 2I_{c0}$. (b) WER estimated from the REE enhanced micromagnetic simulations showed lower-than-macrospin WER when trajectories with $|Q| > 0.25$ are excluded from the calculation. (c)-(d) WER estimated from improved REE simulations, for $I = 4I_{c0}$ and $6I_{c0}$, respectively, with $|Q|$ added as an additional predictor of rare trajectories. Macrospin WERs are the average WER obtained from 100 macrospin REE runs shown in Figure 5.3(b).

at times { t_1, t_2, t_3, ...} in Figure 5.2). Figure 5.10(a) shows example histograms of $|Q|$ at a time instant close to $t = 0$ and at a later instant $t = t_N$ where WER$(t_N) \approx 10^{-6}$, for applied currents of $I = 2I_{c0}$ and $4I_{c0}$. We plot $|Q|$ instead of Q, as the excitations can't be classified *a priori* as V or AV without knowing their core polarity. For lower currents, as in $I = 2I_{c0}$, the total population remained confined near $|Q| \approx 0$ always, indicating absence of any excitations that can generate significant topological charge density. On the other hand, histograms at higher current, e.g. $I = 4I_{c0}$, clearly show a shift of the population toward $|Q| \approx 0.5$, revealing significant number of trajectories with half-integer topological number e.g. V or AV. Note that the peak at higher $|Q|$ is not centered exactly

at 0.5, presumably due to distorted shape of the excitations or edge effects.

To verify that these higher $|Q|$ excitations are indeed responsible for a higher-than-macrospin WER for $I = 4I_{c0}$ and $6I_{c0}$, we recalculated WER excluding all the paths from the initial population of 10^3 trajectories (all offspring, all the way till $t = 0$) that turn into a state with $|Q| > 0.25$. As shown in Figure 5.10(b) for $I = 4I_{c0}$, WER excluding these trajectories are much lower than the macrospin estimates. However, as all rare trajectories are due to a V or AV like path (hence excluded from the estimate in Figure 5.10(b), black curves), the WER could not be calculated below $\sim 10^{-4}$ when these paths were excluded artificially.

The above observation that states with $|Q| > 0.25$ are responsible for slow switching suggests that $|Q|$ can be used to identify rare trials in the REE technique together with $\underline{\langle m_x \rangle}$ for efficient detection of rare trajectories. Instead of only depending on the threshold $\underline{\langle m_{x,\mathrm{th}} \rangle}$, now the trajectories with $|Q| > 0.25$ are also enhanced (split into two offspring). Additionally, a trajectory is not discontinued until it achieves $|Q| \leq 0.25$, even if $\underline{\langle m_x \rangle}$ becomes negative. (This approach essentially eliminates the previously noted overhead of following paths below $\underline{\langle m_x \rangle} = 0$.) The switching time for each trajectory is calculated by detecting the time instant after which $\langle m_x \rangle$ does not appear above zero ever again. Figure 5.10(c) and (d) show the calculated WERs for $I = 4I_{c0}$ and $I = 6I_{c0}$, respectively, with the above modifications to REE technique. The variability among the individual REE runs are now much reduced compared to Figure 5.6(b). Change of slope in the WER curve is also more consistent among the individual REE runs for a given applied current compared to Figure 5.6(b).

To further confirm that the modified slope is a result of high $|Q|$ excitations, additional simulations (without enhancement) are carried out on a population of $\sim 10^3$ AV-like states, similar to the one in Figure 5A, each having $|Q| \approx 0.5$, picked from the REE runs at $I = 4I_{c0}$ (Figure 5.10(c), grey lines) at different times varying from 5 ns to 15 ns. Each of them is re-assigned a weight of 1 and declared as an initial state ($t = 0$). Two different simulations, one with STT (at $I = 4I_{c0}$) and another without STT, are carried out on each of these states. Simulation for each state is continued until $|\langle m_x \rangle| > 0.95$

is reached. In presence of STT, all of these states switched (reached $\langle m_x \rangle \approx -1$). WER calculated from these simulations with STT is shown in Figure 5.11(a) (black line), with a shift along the x and y axes for easy comparison with the slope estimated from the REE simulations (red line). As can be seen, the slope obtained from the STT-induced switching of these sampled AV-like states agrees well with the REE-estimated slope, confirming that the reduced switching speed of AV-like states indeed causes the modified slope. From the simulations without STT, we observed that, approximately half of these AV-like states switched to the desired equilibrium state ($\langle m_x \rangle \approx -1$) and the other half relaxed to the other equilibrium state ($\langle m_x \rangle \approx +1$). That is, an un-torqued AV state has equal probability to end up in either of the equilibrium states, regardless of its $\langle m_x \rangle$ (greater or less than zero) in the AV state. An example trajectory of $\langle m_x \rangle$ from these simulations is shown in Figure 5.11(a) inset along with the definition of the switching time. As the AV core could still be present within the magnet at $\langle m_x \rangle \approx 0$, the trajectory may return to the initial state if the current is indeed turned off at the so-called switching time, causing a write error. However—and conveniently for computational purposes—in the absence of STT, both the switching probability of initial states with $\langle m_x \rangle$ less than 0 and those with $\langle m_x \rangle$ greater than 0 are equal to one-half. Hence, the definition of switching time used throughout, when $\langle m_x \rangle$ falls below 0, leads to the same WER prediction on average for a given time period whether or not the current pulse is actually turned off at the end of that time period.

Although turning off the current at the defined switching instant does not change the calculated WER considerably, the rate at which these states relaxes to either of the equilibrium states in absence of STT, is much slower compared to the case when STT is present. From the simulations without STT, we monitor the fraction of unrelaxed AV-like states with time, separately for the cases with final state of $\langle m_x \rangle \approx -1$ or $+1$. The results are shown in Figure 5.11(b), along with the WER from the simulations with STT (black line, unshifted). As can be seen, the slopes in absence of STT is even lower, implying a longer time scale of relaxing to an equilibrium state in absence of STT. Longer time to relax to the equilibrium states implies that the bit could remain in an undefined state (other than the equilibrium states) for a short time interval after the write pulse has been

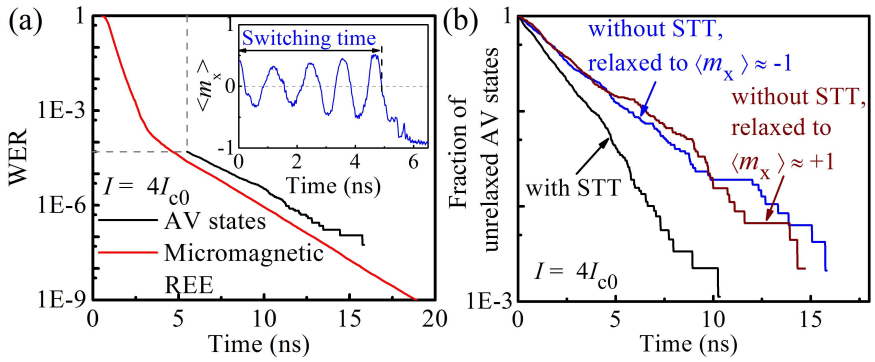

Figure 5.11: (a) Comparison of REE-estimated WER slope with simulations of $\sim 10^3$ sampled non-equilibrium AV-like states. Average WER of 10 REE runs (shown in Figure 7(c)) for $I = 4I_{c0}$ is shown by the red line. For comparison, the black line, shifted by the dashed lines, shows the WER vs. time behavior of a sampled purely AV population simulated in presence of STT. The inset shows the definition of switching time with the help of an example trajectory of $\langle m_x \rangle$. (b) Decay of AV population over time towards $\langle m_x \rangle \approx -1$ (blue line) and $\langle m_x \rangle \approx +1$ (brown line), when allowed to relax without STT. The black line is the same as in (a), shown here unshifted.

turned off.

The onset of a decreased slope of the WER curves at low WERs for high currents, as in Figure 5.10(c)-(d) is similar to the "branching" effect observed in previous experiments [154,155,191]. In experiments, branching is usually identified from WER variation with switching voltage for fixed pulse widths [154, 155, 191], whereas we have estimated the WER variation with time for fixed applied currents. Nonetheless, a change of slope in the one interpretation should correspond to a similar change of slope in the other. In these experiments branching has been observed to be present only in a subset of devices that exhibit same branching characteristics in repeated measurements, while others do not exhibit branching [154, 155, 191]. This difference could arise from variations in device geometry and/or material parameters [155, 191]. As shown in Ref. [154], branching effects are already known to change with applied easy axis magnetic field, temperature etc. Thus, using the methods presented in the paper, it may be possible to identify geometries that help suppress (or inadvertently enhance) such branching and, associated extended required switching times.

For the simulations discussed so far, we have not included the current-induced

Oersted fields. The Oersted field, generated by the current flowing through the nanopillar tunnel junction, is known to influence the switching process of I-STT bits by setting a preference for certain type of C-states and vortices consistent with the symmetry of the field [171, 181]. To verify if Oersted field reduces the probability of AV-like paths (as seen Figure 6(a), e.g.), we include the Oersted field in a set of control simulations. In these simulations, the Oersted field was calculated by assuming a uniform and constant current density flowing through a vertical nanopillar of 50 nm height and cross-section same as the elliptic magnet [201]. The free layer was assumed to be at the center of the nanopillar. However, no visible changes are observed in the WERs, and the presence of AV-like excitations were not notably affected. However, the current density applied to achieve switching in these early studies [171,180,181,192,193,195] involving spin-valve nanopillars were at least an order of magnitude higher than the range of applied current studied here. Hence, a much stronger Oersted field was expected in these experiments. When the Oersted field is increased in our simulations artificially by $20\times$ (keeping the STT same at $I = 4I_{c0}$), more V-type excitations (e.g. Figure 5.9(b)) are observed and presence of AV-like trajectories are reduced drastically. Nonetheless, these V-type trajectories now become the bottleneck for successful switching and results in a very similar WER behavior (not shown) as in Figure 5.10(c)-(d).

5.4 Summary

In summary, we have extended the previously proposed REE technique for WER calculation to the STT switching of in-plane magnets, including adding a rare-event predictor based on the topological charge of the magnetic excitation. The modified technique allows us to estimate ultra-low WERs taking into account spatially-incoherent switching processes including the end mode, vortex and anti-vortex states. The results show that spatially-incoherent excitations give rise to increased WER predictions as compared to those of spatially coherent macrospin calculations. Moreover, magnetization locked into such spatially-incoherent states, can lead to an incubation-like delay and failed switching attempts. At higher applied currents, vortex and anti-vortex excitations start to domi-

nate the unswitched population. The result of prolonged lifetimes while in these states is a decrease in the slope (magnitude) of the WER vs. switching time curve once they become dominant, and, thus, longer required switching times than otherwise would be expected. Notably, the onset of this reduced slope cannot even be reached practically in the required micromagnetic simulation without REE Monte Carlo simulation, let alone modeled to probabilities of 10^{-9} or below. The branching of the WER slope observed in simulation here appears conceptually consistent with observed branching of WER vs. switching voltage in experimental studies. Finally, we note that we have focused on basic REE methods to allow modeling of WERs, including identifying appropriate predictors of rare events.

Chapter 6

Conclusion

6.1 Summary of the dissertation

The work discussed in this dissertation covered a number of topics broadly related to the write process of STTRAM. Two key facts of interest, as mentioned in Chapter 1, are the large write current required to switch the free layer magnet in an STTRAM bit and the stochastic nature of this switching process. In subsequent chapters, possible techniques to evaluate and improve the write process have been studied. Reduced storage density is one of the problems related to the write current requirement. This study focused on the magnetization switching process of a multi-state magnetic memory bit with an aim to increase the storage density (Chapter 2). Reduced write currents of perpendicular magnets motivated the study of chromium telluride thin films, a perpendicular magnetic anisotropy material (Chapter 3). For the problems related to the stochastic write process, this dissertation primarily focused on the techniques to quantify write error rates caused by this stochastic process (Chapters 4 and 5). Micromagnetic simulations have been employed in each of these studies to investigate the switching processes and estimate quantities of interest. Conclusions from each of the chapters are noted below:

- Chapter 2 evaluates a multi-state STTRAM bit based on the shape anisotropy of a cross-shaped ferromagnet for possible improvements in the bit storage density. STT-induced write process for such shape-engineered ferromagnet required quite large write currents, that ultimately outweigh the advantage of a 2 bit per cell storage. A voltage controlled precessional write process is found to be more energy efficient than the STT-based write process. Switching times and write energies of the proposed multi-state bit are estimated from micromagnetic simulations. Thermal stability of the bit then is calculated employing the string method. The results

show that such a multi-state memory with an ultra-low power write process could be viable if the material properties and device dimensions are chosen appropriately.

- Chapter 3 investigates the magnetic properties of epitaxial chromium telluride thin films. These thin films exhibit strong perpendicular magnetic anisotropy. The study quantifies the magnetic anisotropy energies of the thin film from the magnetization hysteresis loops measurements. For these thin films, a relatively large second order anisotropy coefficient is obtained. The angular dependence of the switching field then is compared with different models of magnetization reversal. Finally, using a 1D model of a defect and considering both nucleation and pinning mechanisms, the angular dependence of the switching field is explained satisfactorily. Micromagnetic simulations then are carried out to visualize the switching process.

- Chapter 4 introduces the topic of write errors related to the stochastic nature of the STT switching process at finite temperatures. First, the existing techniques for calculating write error rates are summarized. The majority of the existing studies assumed a macrospin description that fails to capture spatially-incoherent switching processes. To estimate write errors to ultra-low values of 10^{-9} while capturing these processes, a rare-event-enhanced micromagnetic simulation approach has been developed. This technique enables us to estimate write error rates to 10^{-9} from only $\sim 10^3$ micromagnetic simulations. This technique first is applied within the macrospin approximation to benchmark the predicted write error rates with that obtained from the Fokker-Planck equation. Then applying this technique together with micromagnetic simulations, WERs for perpendicular STT-RAM bits have been estimated.

- Chapter 5 extends the rare-event-enhancement based approach toward the STT-induced switching of an in-plane magnet. Again the technique first is applied within the macrospin approximation to verify the correctness of the solutions. Then write error rates from full micromagnetic simulations are obtained. The result show presence of multiple switching pathways with spatially-incoherent magnetization states such as end mode, vortex or anti-vortex, which cannot be captured by the

macrospin simulations. Moreover, vortex or anti-vortex excitations cause the basic rare-event-enhancement technique to fail. However, adding a "topological charge" based predictor to the rare-event-enhancement technique leads to reliable estimates again.

6.2 Future work

The research presented in this dissertation also serves as the groundwork for a number of interesting future research directions. Some of these possibilities are noted below:

- The study of the multi-state STTRAM in Chapter 2 concludes that, despite being able to store two bits, the structure may not provide enhanced storage density as compared to two analogous single-bit devices. It may be worth reevaluating the above statement by repeating the study with a stronger VCMA coefficient and designing an optimized layout density of the proposed multi-bit memory. Then the result could be compared with a single bit memory to quantify possible improvements in the storage density, if any.

- As noted in Chapter 3, strong uniaxial magnetic anisotropy of chromium telluride thin films could be useful for achieving thermally stable magnets of nanoscale dimensions as well as an alternative to rare-earth based permanent magnet materials. Further experiments may be carried out to investigate if the Curie temperature could be increased beyond the room temperature by varying the composition of the thin film, while preserving the strong uniaxial magnetic anisotropy.

- Chapter 4 shows that the write error rate slopes of the perpendicular STTRAM bits, estimated from the rare-event-enhanced micromagnetic simulations, are much higher (in magnitude) than the slopes obtained within the macrospin approximation. Details of the switching process that gives rise to an improved write error behavior could be studied further following the approach taken in Chapter 5. Finally,

the predicted write error rates for varying applied currents and device dimensions may be fitted into a model suitable for circuit level simulations.

- The study in Chapter 4 considered a perpendicular STTRAM bit of circular cross-section. Although, circular magnets are preferred for all practical purposes, process variations could result into shape distortion. It would be interesting to study how the shape affects the write error slopes of a perpendicular STTRAM bit. Note that the precise rare-event-enhancement technique used for a circular magnet may not work well for a different shape (elliptic e.g.) and the technique could then be modified following the one described in Chapter 5 for the elliptic in-plane bit.

- The onset of a decreased (in magnitude) slope of the write error curves for high currents, as discussed in Chapter 5, Section 5.3.2, appears conceptually consistent with observed branching of WER vs. switching voltage in experimental studies. The fact that in the experiments branching has been observed to be present only in a subset of devices, suggests that variation in device geometry and/or material parameters could possibly alter the "branching" observed in our simulations. This could be studied employing the techniques discussed in Chapter 5 and repeating the write error calculation for devices with varying dimensions and shapes. Such a study will probably require some experimental investigations as well, to identify possible shape distortions that occur during the fabrication.

Bibliography

[1] M. T. Bohr and I. A. Young, "CMOS Scaling Trends and Beyond," *IEEE Micro*, vol. 37, pp. 20–29, November 2017.

[2] S. Yu and P. Y. Chen, "Emerging Memory Technologies: Recent Trends and Prospects," *IEEE Solid-State Circuits Magazine*, vol. 8, pp. 43–56, Spring 2016.

[3] T. N. Theis and H. S. P. Wong, "The End of Moore's Law: A New Beginning for Information Technology," *Computing in Science Engineering*, vol. 19, pp. 41–50, Mar 2017.

[4] A. Makarov, V. Sverdlov, and S. Selberherr, "Emerging memory technologies: Trends, challenges, and modeling methods," *Microelectronics Reliability*, vol. 52, no. 4, pp. 628–634, 2012.

[5] ITRS, "ITRS Reports," tech. rep., International Technology Roadmap for Semiconductors, 2013.

[6] J. S. Meena, S. M. Sze, U. Chand, and T.-Y. Tseng, "Overview of emerging nonvolatile memory technologies," *Nanoscale Research Letters*, vol. 9, p. 526, Sep 2014.

[7] U. Roy, *Towards high-density low-power spin-transfer-torque random access memory*. PhD thesis, University of Texas at Austin, 2015.

[8] C. C. Hsieh, *Cerium oxide based resistive random access memory devices*. PhD thesis, University of Texas at Austin, 2017.

[9] H. Yoda, S. Fujita, N. Shimomura, E. Kitagawa, K. Abe, K. Nomura, H. Noguchi, and J. Ito, "Progress of STT-MRAM technology and the effect on normally-off computing systems," *Technical Digest - International Electron Devices Meeting, IEDM*, pp. 259–262, 2012.

[10] S. Yuasa, A. Fukushima, K. Yakushiji, T. Nozaki, M. Konoto, H. Maehara, H. Kubota, T. Taniguchi, H. Arai, H. Imamura, K. Ando, Y. Shiota, F. Bonell, Y. Suzuki, N. Shimomura, E. Kitagawa, J. Ito, S. Fujita, K. Abe, K. Nomura, H. Noguchi, and H. Yoda, "Future prospects of MRAM technologies," in *2013 IEEE International Electron Devices Meeting*, pp. 3.1.1–3.1.4, Dec 2013.

[11] A. V. Khvalkovskiy, D. Apalkov, S. Watts, R. Chepulskii, R. S. Beach, A. Ong, X. Tang, A. Driskill-Smith, W. H. Butler, P. B. Visscher, D. Lottis, E. Chen, V. Nikitin, and M. Krounbi, "Basic principles of STT-MRAM cell operation in memory arrays," *Journal of Physics D: Applied Physics*, vol. 46, no. 7, p. 074001, 2013.

[12] M. N. Baibich, J. M. Broto, A. Fert, F. N. Van Dau, F. Petroff, P. Etienne, G. Creuzet, A. Friederich, and J. Chazelas, "Giant magnetoresistance of (001)Fe/(001)Cr magnetic superlattices," *Phys. Rev. Lett.*, vol. 61, pp. 2472–2475, Nov 1988.

[13] G. Binasch, P. Grünberg, F. Saurenbach, and W. Zinn, "Enhanced magnetoresistance in layered magnetic structures with antiferromagnetic interlayer exchange," *Phys. Rev. B*, vol. 39, pp. 4828–4830, Mar 1989.

[14] M. Julliere, "Tunneling between ferromagnetic films," *Physics Letters A*, vol. 54, no. 3, pp. 225 – 226, 1975.

[15] T. Miyazaki and N. Tezuka, "Giant magnetic tunneling effect in Fe/Al_2O_3/Fe junction," *Journal of Magnetism and Magnetic Materials*, vol. 139, no. 3, pp. L231 – L234, 1995.

[16] J. S. Moodera, L. R. Kinder, T. M. Wong, and R. Meservey, "Large magnetoresistance at room temperature in ferromagnetic thin film tunnel junctions," *Phys. Rev. Lett.*, vol. 74, pp. 3273–3276, Apr 1995.

[17] J. Daughton, "Magnetoresistive memory technology," *Thin Solid Films*, vol. 216, no. 1, pp. 162 – 168, 1992. Papers presented at the International Workshop on

Science and Technology of Thin Films for the 21^{st} Century, Evanston,IL, USA, July 28-August 2, 1991.

[18] S. Tehrani, M. Durlam, M. DeHerrera, E. Chen, J. Calder, and G. Kerszykowski, "High density pseudo spin valve magnetoresistive RAM," in *Seventh Biennial IEEE International Nonvolatile Memory Technology Conference Proceedings*, pp. 43–46, Jun 1998.

[19] R. Scheuerlein, W. Gallagher, S. Parkin, A. Lee, S. Ray, R. Robertazzi, and W. Reohr, "A 10 ns read and write non-volatile memory array using a magnetic tunnel junction and FET switch in each cell," in *2000 IEEE International Solid-State Circuits Conference. Digest of Technical Papers (Cat. No.00CH37056)*, pp. 128–129, Feb 2000.

[20] M. Durlam, P. Naji, M. DeHerrera, S. Tehrani, G. Kerszykowski, and K. Kyler, "Nonvolatile RAM based on magnetic tunnel junction elements," in *2000 IEEE International Solid-State Circuits Conference. Digest of Technical Papers (Cat. No.00CH37056)*, pp. 130–131, Feb 2000.

[21] S. Tehrani, J. M. Slaughter, M. Deherrera, B. N. Engel, N. D. Rizzo, J. Salter, M. Durlam, R. W. Dave, J. Janesky, B. Butcher, K. Smith, and G. Grynkewich, "Magnetoresistive random access memory using magnetic tunnel junctions," *Proceedings of the IEEE*, vol. 91, pp. 703–714, May 2003.

[22] J. H. Park, W. C. Jeong, H. J. Kim, J. H. Oh, H. C. Koo, G. H. Koh, G. T. Jeong, H. S. Jeong, Y. J. Jeong, S. L. Cho, J. E. Lee, H. J. Kim, and K. Kim, "An $8F^2$ MRAM technology using modified metal lines," in *IEEE International Electron Devices Meeting 2003*, pp. 34.3.1–34.3.4, Dec 2003.

[23] W. J. Gallagher and S. S. P. Parkin, "Development of the magnetic tunnel junction MRAM at IBM: From first junctions to a 16-Mb MRAM demonstrator chip," *IBM Journal of Research and Development*, vol. 50, pp. 5–23, Jan 2006.

[24] W. H. Butler, X.-G. Zhang, T. C. Schulthess, and J. M. MacLaren, "Spin-dependent tunneling conductance of $\mathrm{Fe|MgO|Fe}$ sandwiches," *Phys. Rev. B*, vol. 63, p. 054416, Jan 2001.

[25] J. Mathon and A. Umerski, "Theory of tunneling magnetoresistance of an epitaxial Fe/MgO/Fe(001) junction," *Phys. Rev. B*, vol. 63, p. 220403, May 2001.

[26] S. S. Parkin, C. Kaiser, A. Panchula, P. M. Rice, B. Hughes, M. Samant, and S.-H. Yang, "Giant tunnelling magnetoresistance at room temperature with MgO (100) tunnel barriers," *Nature Materials*, vol. 3, no. 12, p. 862, 2004.

[27] S. Yuasa, T. Nagahama, A. Fukushima, Y. Suzuki, and K. Ando, "Giant room-temperature magnetoresistance in single-crystal Fe/MgO/Fe magnetic tunnel junctions," *Nature Materials*, vol. 3, no. 12, p. 868, 2004.

[28] J. C. Slonczewski, "Current-driven excitation of magnetic multilayers," *Journal of Magnetism and Magnetic Materials*, vol. 159, pp. L1–L7, June 1996.

[29] L. Berger, "Emission of spin waves by a magnetic multilayer traversed by a current," *Phys. Rev. B*, vol. 54, pp. 9353–9358, Oct 1996.

[30] S. Ikeda, H. Sato, H. Honjo, E. C. I. Enobio, S. Ishikawa, M. Yamanouchi, S. Fukami, S. Kanai, F. Matsukura, T. Endoh, and H. Ohno, "Perpendicular-anisotropy CoFeB-MgO based magnetic tunnel junctions scaling down to 1X nm," in *2014 IEEE International Electron Devices Meeting*, pp. 33.2.1–33.2.4, Dec 2014.

[31] J. J. Nowak, R. P. Robertazzi, J. Z. Sun, G. Hu, J. H. Park, J. Lee, A. J. Annunziata, G. P. Lauer, R. Kothandaraman, E. J. O'Sullivan, P. L. Trouilloud, Y. Kim, and D. C. Worledge, "Dependence of voltage and size on write error rates in spin-transfer torque magnetic random-access memory," *IEEE Magnetics Letters*, vol. 7, pp. 1–4, 2016.

[32] G. Hu, J. J. Nowak, G. Lauer, J. H. Lee, J. Z. Sun, J. Harms, A. Annunziata, S. Brown, W. Chen, Y. H. Kim, N. Marchack, S. Murthy, C. Kothandaraman,

E. J. O'Sullivan, J. H. Park, M. Reuter, R. P. Robertazzi, P. L. Trouilloud, Y. Zhu, and D. C. Worledge, "Low-current Spin Transfer Torque MRAM," in *2017 International Symposium on VLSI Design, Automation and Test (VLSI-DAT)*, pp. 1–2, April 2017.

[33] E. Y. Tsymbal, O. N. Mryasov, and P. R. LeClair, "Spin-dependent tunnelling in magnetic tunnel junctions," *Journal of Physics: Condensed Matter*, vol. 15, no. 4, p. R109, 2003.

[34] S. Ikeda, J. Hayakawa, Y. Ashizawa, Y. M. Lee, K. Miura, H. Hasegawa, M. Tsunoda, F. Matsukura, and H. Ohno, "Tunnel magnetoresistance of 604% at 300k by suppression of Ta diffusion in CoFeB/MgO/CoFeB pseudo-spin-valves annealed at high temperature," *Applied Physics Letters*, vol. 93, no. 8, p. 082508, 2008.

[35] E. Y. Tsymbal and I. Zutic, *Handbook of Spin Transport and Magnetism*. CRC press, 2011.

[36] W. Brown, *Micromagnetics*. Interscience tracts on physics and astronomy, Interscience Publishers, 1963.

[37] A. Aharoni, *Introduction to the Theory of Ferromagnetism*. Clarendon Press, 1996.

[38] J. M. D. Coey, *Magnetism and Magnetic Materials*. Cambridge University Press, 2010.

[39] M. Johnson, P. Bloemen, F. Den Broeder, and J. De Vries, "Magnetic anisotropy in metallic multilayers," *Reports on Progress in Physics*, vol. 59, no. 11, p. 1409, 1996.

[40] S. Ikeda, K. Miura, H. Yamamoto, K. Mizunuma, H. D. Gan, M. Endo, S. Kanai, J. Hayakawa, F. Matsukura, and H. Ohno, "A perpendicular-anisotropy CoFeB-MgO magnetic tunnel junction," *Nature Materials*, vol. 9, no. 9, pp. 721–724, 2010.

[41] M. J. Donahue and D. G. Porter, "OOMMF User's Guide, Version 1.0," tech. rep., National Institute of Standards and Technology, Gaithersburg, MD, Sept 1999.

[42] A. Vansteenkiste, J. Leliaert, M. Dvornik, M. Helsen, F. Garcia-Sanchez, and B. Van Waeyenberge, "The design and verification of MuMax3," *AIP Advances*, vol. 4, p. 107133, Oct. 2014.

[43] A. Aharoni, "Demagnetizing factors for rectangular ferromagnetic prisms," *Journal of Applied Physics*, vol. 83, pp. 3432–3434, Mar. 1998.

[44] R. D. McMichael and M. D. Stiles, "Magnetic normal modes of nanoelements," *Journal of Applied Physics*, vol. 97, no. 10, p. 10J901, 2005.

[45] Z. Diao, Z. Li, S. Wang, Y. Ding, A. Panchula, E. Chen, L.-C. Wang, and Yiming Huai, "Spin-transfer torque switching in magnetic tunnel junctions and spin-transfer torque random access memory," *Journal of Physics: Condensed Matter*, vol. 19, no. 16, p. 165209, 2007.

[46] C. W. Smullen IV, V. Mohan, A. Nigam, S. Gurumurthi, and M. R. Stan, "Relaxing non-volatility for fast and energy-efficient STT-RAM caches," *Proceedings - International Symposium on High-Performance Computer Architecture*, pp. 50–61, 2011.

[47] J. Z. Sun, "Spin-current interaction with a monodomain magnetic body: A model study," *Phys. Rev. B*, vol. 62, pp. 570–578, Jul 2000.

[48] J. Grollier, V. Cros, H. Jaffrès, A. Hamzic, J. M. George, G. Faini, J. Ben Youssef, H. Le Gall, and A. Fert, "Field dependence of magnetization reversal by spin transfer," *Phys. Rev. B*, vol. 67, p. 174402, May 2003.

[49] W. F. Brown, "Thermal Fluctuations of a Single-Domain Particle," *Physical Review*, vol. 130, pp. 1677–1686, June 1963.

[50] Z. Li and S. Zhang, "Thermally assisted magnetization reversal in the presence of a spin-transfer torque," *Phys. Rev. B*, vol. 69, p. 134416, Apr 2004.

[51] W. H. Butler, T. Mewes, C. K. A. Mewes, P. B. Visscher, W. H. Rippard, S. E. Russek, and R. Heindl, "Switching Distributions for Perpendicular Spin-Torque Devices Within the Macrospin Approximation," *IEEE Transactions on Magnetics*, vol. 48, pp. 4684–4700, Dec. 2012.

[52] S. Mangin, D. Ravelosona, J. Katine, M. Carey, B. Terris, and E. Fullerton, "Current-induced magnetization reversal in nanopillars with perpendicular anisotropy," *Nature Materials*, vol. 5, no. 3, pp. 210–215, 2006.

[53] Y. Zhang, L. Zhang, W. Wen, G. Sun, and Y. Chen, "Multi-level cell STT-RAM: Is it realistic or just a dream?," in *2012 IEEE/ACM International Conference on Computer-Aided Design (ICCAD)*, pp. 526–532, Nov 2012.

[54] B. K. Kaushik, S. Verma, A. A. Kulkarni, and S. Prajapati, *Next Generation Spin Torque Memories*, pp. 51–70. Singapore: Springer Singapore, 2017.

[55] X. Lou, Z. Gao, D. V. Dimitrov, and M. X. Tang, "Demonstration of multilevel cell spin transfer switching in MgO magnetic tunnel junctions," *Applied Physics Letters*, vol. 93, no. 24, p. 242502, 2008.

[56] T. Ishigaki, T. Kawahara, R. Takemura, K. Ono, K. Ito, H. Matsuoka, and H. Ohno, "A multi-level-cell spin-transfer torque memory with series-stacked magnetotunnel junctions," in *VLSI Technology (VLSIT), 2010 Symposium on*, pp. 47–48, IEEE, 2010.

[57] R. Sbiaa, R. Law, S. Lua, E. Tan, T. Tahmasebi, C. Wang, and S. Piramanayagam, "Spin transfer torque switching for multi-bit per cell magnetic memory with perpendicular anisotropy," *Applied Physics Letters*, vol. 99, no. 9, p. 092506, 2011.

[58] Y. Kim, X. Fong, K. W. Kwon, M. C. Chen, and K. Roy, "Multilevel Spin-Orbit Torque MRAMs," *IEEE Transactions on Electron Devices*, vol. 62, pp. 561–568, Feb 2015.

[59] Q. Shi, Z. Wang, Y. Gao, L. Chang, W. Kang, Y. Zhang, and W. Zhao, "A spin Hall effect-based multi-level cell for MRAM," in *2016 IEEE/ACM International Symposium on Nanoscale Architectures (NANOARCH)*, pp. 143–144, July 2016.

[60] W. Zhao, S. Chaudhuri, C. Accoto, J. O. Klein, C. Chappert, and P. Mazoyer, "Cross-Point Architecture for Spin-Transfer Torque Magnetic Random Access Memory," *IEEE Transactions on Nanotechnology*, vol. 11, pp. 907–917, Sept. 2012.

[61] H. Park, R. Dorrance, A. Amin, F. Ren, D. Markovic, and C. K. K. Yang, "Analysis of STT-RAM cell design with multiple MTJs per access," in *2011 IEEE/ACM International Symposium on Nanoscale Architectures*, pp. 53–58, June 2011.

[62] N. Sakimura, T. Sugibayashi, T. Honda, S. Miura, H. Numata, H. Hada, and S. Tahara, "A 512kb cross-point cell MRAM," in *2003 IEEE International Solid-State Circuits Conference, 2003. Digest of Technical Papers. ISSCC.*, pp. 278–279 vol.1, Feb. 2003.

[63] A. Chen, "Feasibility Analysis of High-Density Spin-Transfer-Torque Random-Access-Memory With Shared Access Transistor Structure," *IEEE Electron Device Letters*, vol. 36, pp. 1325–1328, Dec. 2015.

[64] M. Sharad, R. Venkatesan, A. Raghunathan, and K. Roy, "Multi-level magnetic RAM using domain wall shift for energy-efficient, high-density caches," in *International Symposium on Low Power Electronics and Design (ISLPED)*, pp. 64–69, Sept 2013.

[65] J. Cai, B. Fang, C. Wang, and Z. Zeng, "Multilevel storage device based on domain-wall motion in a magnetic tunnel junction," *Applied Physics Letters*, vol. 111, no. 18, p. 182410, 2017.

[66] D. E. Nikonov, G. I. Bourianoff, and T. Ghani, "Proposal of a spin torque majority gate logic," *IEEE Electron Device Letters*, vol. 32, no. 8, pp. 1128–1130, 2011.

[67] D. E. Nikonov, S. Manipatruni, and I. A. Young, "Switching efficiency improvement in spin torque majority gates," *Journal of Applied Physics*, vol. 115, no. 17, p. 17C736, 2014.

[68] V. Cambel and G. Karapetrov, "Control of vortex chirality and polarity in magnetic nanodots with broken rotational symmetry," *Physical Review B*, vol. 84, no. 1, p. 014424, 2011.

[69] B. Lambson, Z. Gu, D. Carlton, S. Dhuey, A. Scholl, A. Doran, A. Young, and J. Bokor, "Cascade-like signal propagation in chains of concave nanomagnets," *Applied Physics Letters*, vol. 100, no. 15, p. 152406, 2012.

[70] K. Nanayakkara, A. P. Jacob, and A. Kozhanov, "Spin wave scattering and interference in ferromagnetic cross," *Journal of Applied Physics*, vol. 118, no. 16, p. 163904, 2015.

[71] X. W. Dimitar V. Dimitrov, Zheng Gao, "Multi-bit STRAM memory cells," 07 2010. Patent.

[72] Y. Telepinsky, V. Mor, M. Schultz, Y.-M. Hung, A. D. Kent, and L. Klein, "Towards a six-state magnetic memory element," *Applied Physics Letters*, vol. 108, no. 18, p. 182401, 2016.

[73] U. Roy, T. Pramanik, M. Tsoi, L. F. Register, and S. K. Banerjee, "Micromagnetic study of spin-transfer-torque switching of a ferromagnetic cross towards multi-state spin-transfer-torque based random access memory," *Journal of Applied Physics*, vol. 113, no. 22, p. 223904, 2013.

[74] T. Pramanik, U. Roy, M. Tsoi, L. F. Register, and S. K. Banerjee, "Micromagnetic simulations of spin-wave normal modes and the spin-transfer-torque driven magnetization dynamics of a ferromagnetic cross," *Journal of Applied Physics*, vol. 115, p. 17D123, 2014.

[75] T. Pramanik, U. Roy, L. F. Register, and S. K. Banerjee, "Proposal of a multistate memory using voltage controlled magnetic anisotropy of a cross-shaped ferromagnet," *IEEE Transactions on Nanotechnology*, vol. 14, no. 5, pp. 883–888, 2015.

[76] F. Lee, "Shape-induced biaxial anisotropy in thin magnectic films," *IEEE Transactions on Magnetics*, vol. 4, no. 3, pp. 502–506, 1968.

[77] A. Vatankhahghadim and A. Sheikholeslami, "A Multi-level Cell for STT-MRAM with Biaxial Magnetic Tunnel Junction," in *2015 IEEE International Symposium on Multiple-Valued Logic*, pp. 158–163, May 2015.

[78] T. B. Kumary, B. Ghosh, B. Awadhiya, and A. K. Verma, "Performance analysis of STT-RAM with cross shaped free layer using Heusler alloys," *Journal of Semiconductors*, vol. 37, no. 1, p. 014003, 2016.

[79] J. Sankey, P. Braganca, A. Garcia, I. Krivorotov, R. Buhrman, and D. Ralph, "Spin-Transfer-Driven Ferromagnetic Resonance of Individual Nanomagnets," *Physical Review Letters*, vol. 96, p. 227601, June 2006.

[80] M. Tsoi, A. Jansen, J. Bass, W.-C. Chiang, M. Seck, V. Tsoi, and P. Wyder, "Excitation of a Magnetic Multilayer by an Electric Current," *Physical Review Letters*, vol. 80, pp. 4281–4284, May 1998.

[81] S. I. Kiselev, J. C. Sankey, I. N. Krivorotov, N. C. Emley, R. J. Schoelkopf, R. a. Buhrman, and D. C. Ralph, "Microwave oscillations of a nanomagnet driven by a spin-polarized current.," *Nature*, vol. 425, pp. 380–3, Sept. 2003.

[82] D. Berkov and N. Gorn, "Magnetization precession due to a spin-polarized current in a thin nanoelement: Numerical simulation study," *Physical Review B*, vol. 72, p. 094401, Sept. 2005.

[83] I. Krivorotov, D. Berkov, N. Gorn, N. Emley, J. Sankey, D. Ralph, and R. Buhrman, "Large-amplitude coherent spin waves excited by spin-polarized current in nanoscale spin valves," *Physical Review B*, vol. 76, p. 024418, July 2007.

[84] X.-g. Wang, G.-h. Guo, G.-f. Zhang, Y.-z. Nie, Q.-l. Xia, and Z.-x. Li, "Spin-transfer torque induced domain wall ferromagnetic resonance in nanostrips," *Journal of Magnetism and Magnetic Materials*, vol. 332, pp. 56–60, Apr. 2013.

[85] P. E. Roy, T. Trypiniotis, and C. H. W. Barnes, "Micromagnetic simulations of spin-wave normal modes and the resonant field-driven magnetization dynamics of a 360 degree domain wall in a soft magnetic stripe," *Physical Review B*, vol. 82, p. 134411, Oct. 2010.

[86] D. E. Nikonov, G. I. Bourianoff, G. Rowlands, and I. N. Krivorotov, "Strategies and tolerances of spin transfer torque switching," *Journal of Applied Physics*, vol. 107, no. 11, p. 113910, 2010.

[87] C. Lee, J. Yang, and T. Wu, "Micromagnetic Simulation for Spin-Transfer Switching With a Tilted Spin Polarizer," *Magnetics, IEEE Transactions on*, vol. 47, no. 3, pp. 649–652, 2011.

[88] K. Guslienko, R. Chantrell, and A. Slavin, "Dipolar localization of quantized spin-wave modes in thin rectangular magnetic elements," *Physical Review B*, vol. 68, p. 024422, July 2003.

[89] J. G. A. Vinasco, *Voltage-Controlled Magnetic Dynamics in Nanoscale Magnetic Tunnel Junctions*. PhD thesis, University of California, Los Angeles, 2014.

[90] A. Hallal, H. X. Yang, B. Dieny, and M. Chshiev, "Anatomy of perpendicular magnetic anisotropy in fe/mgo magnetic tunnel junctions: First-principles insight," *Phys. Rev. B*, vol. 88, p. 184423, Nov 2013.

[91] B. Dieny and M. Chshiev, "Perpendicular magnetic anisotropy at transition metal/oxide interfaces and applications," *Rev. Mod. Phys.*, vol. 89, p. 025008, Jun 2017.

[92] C. G. Duan, J. P. Velev, R. F. Sabirianov, Z. Zhu, J. Chu, S. S. Jaswal, and E. Y. Tsymbal, "Surface magnetoelectric effect in ferromagnetic metal films," *Physical Review Letters*, vol. 101, no. September, pp. 1–4, 2008.

[93] T. Maruyama, Y. Shiota, T. Nozaki, K. Ohta, N. Toda, M. Mizuguchi, A. A. Tulapurkar, T. Shinjo, M. Shiraishi, S. Mizukami, Y. Ando, and Y. Suzuki, "Large voltage-induced magnetic anisotropy change in a few atomic layers of iron.," *Nature nanotechnology*, vol. 4, no. March, pp. 158–161, 2009.

[94] M. K. Niranjan, C. G. Duan, S. S. Jaswal, and E. Y. Tsymbal, "Electric field effect on magnetization at the Fe/MgO(001) interface," *Applied Physics Letters*, vol. 96, no. 001, pp. 18–21, 2010.

[95] Y. Shiota, T. Nozaki, F. Bonell, S. Murakami, T. Shinjo, and Y. Suzuki, "Induction of coherent magnetization switching in a few atomic layers of FeCo using voltage pulses," *Nature Materials*, vol. 11, no. 1, pp. 39–43, 2011.

[96] W.-G. Wang, M. Li, S. Hageman, and C. L. Chien, "Electric-field-assisted switching in magnetic tunnel junctions," *Nature Materials*, vol. 11, no. 1, pp. 64–68, 2011.

[97] J. Zhu, J. Katine, G. Rowlands, Y.-J. Chen, Z. Duan, J. Alzate, P. Upadhyaya, J. Langer, P. Amiri, K. Wang, and I. Krivorotov, "Voltage-induced ferromagnetic resonance in magnetic tunnel junctions," *Physical Review Letters*, vol. 108, no. May, pp. 1–5, 2012.

[98] J. G. Alzate, P. K. Amiri, P. Upadhyaya, S. S. Cherepov, J. Zhu, M. Lewis, R. Dorrance, J. a. Katine, J. Langer, K. Galatsis, D. Markovic, I. Krivorotov, and K. L. Wang, "Voltage-induced switching of nanoscale magnetic tunnel junctions," *Technical Digest - International Electron Devices Meeting, IEDM*, pp. 681–684, 2012.

[99] S. Kanai, Y. Nakatani, M. Yamanouchi, S. Ikeda, H. Sato, F. Matsukura, and H. Ohno, "Magnetization switching in a CoFeB/MgO magnetic tunnel junction by combining spin-transfer torque and electric field-effect," *Applied Physics Letters*, vol. 104, no. 21, p. 212406, 2014.

[100] S. Kanai, M. Yamanouchi, S. Ikeda, Y. Nakatani, F. Matsukura, and H. Ohno, "Electric field-induced magnetization reversal in a perpendicular-anisotropy CoFeB-

MgO magnetic tunnel junction," *Applied Physics Letters*, vol. 101, no. 12, p. 122403, 2012.

[101] W. Zhu, D. Xiao, Y. Liu, S. Gong, and C.-G. Duan, "Picosecond electric field pulse induced coherent magnetic switching in MgO/FePt/Pt (001)-based tunnel junctions: a multiscale study," *Scientific reports*, vol. 4, 2014.

[102] P. K. Amiri, P. Upadhyaya, J. Alzate, and K. Wang, "Electric-field-induced thermally assisted switching of monodomain magnetic bits," *Journal of Applied Physics*, vol. 113, no. 1, p. 013912, 2013.

[103] I. D. Mayergoyz, G. Bertotti, and C. Serpico, *Nonlinear magnetization dynamics in nanosystems*. Elsevier, 2009.

[104] S. Kanai, M. Yamanouchi, S. Ikeda, Y. Nakatani, F. Matsukura, and H. Ohno, "Electric field-induced magnetization switching in CoFeB-MgO—static magnetic field angle dependence," *Magnetics, IEEE Transactions on*, vol. 50, no. 1, pp. 1–3, 2014.

[105] M. Yamanouchi, A. Jander, P. Dhagat, S. Ikeda, F. Matsukura, and H. Ohno, "Domain Structure in CoFeB Thin Films With Perpendicular Magnetic Anisotropy," *IEEE Magnetics Letters*, vol. 2, pp. 3000304–3000304, 2011.

[106] K. Kita, D. W. Abraham, M. J. Gajek, and D. C. Worledge, "Electric-field-control of magnetic anisotropy of $Co_{0.6}Fe_{0.2}B_{0.2}$/oxide stacks using reduced voltage," *Journal of Applied Physics*, vol. 112, no. 3, pp. –, 2012.

[107] D. V. Dimitrov, Z. Gao, X. Wang, W. Jung, X. Lou, and O. G. Heinonen, "Dielectric breakdown of MgO magnetic tunnel junctions," *Applied Physics Letters*, vol. 94, 2009.

[108] T. Kawahara, "Challenges toward gigabit-scale spin-transfer torque random access memory and beyond for normally off, green information technology infrastructure (invited)," *Journal of Applied Physics*, vol. 109, no. 7, pp. –, 2011.

[109] M. Schäfers, V. Drewello, G. Reiss, a. Thomas, K. Thiel, G. Eilers, M. Münzenberg, H. Schuhmann, and M. Seibt, "Electric breakdown in ultrathin MgO tunnel barrier junctions for spin-transfer torque switching," *Applied Physics Letters*, vol. 95, no. 2009, pp. 2–5, 2009.

[110] S. Bandiera, R. C. Sousa, Y. Dahmane, C. Ducruet, C. Portemont, V. Baltz, S. Auffret, I. L. Prejbeanu, and B. Dieny, "Comparison of synthetic antiferromagnets and hard ferromagnets as reference layer in magnetic tunnel junctions with perpendicular magnetic anisotropy," *IEEE Magnetics Letters*, vol. 1, pp. 1–4, 2010.

[111] M. M. de Castro, R. Sousa, S. Bandiera, C. Ducruet, A. Chavent, S. Auffret, C. Papusoi, I. Prejbeanu, C. Portemont, L. Vila, *et al.*, "Precessional spin-transfer switching in a magnetic tunnel junction with a synthetic antiferromagnetic perpendicular polarizer," *Journal of Applied Physics*, vol. 111, no. 7, p. 07C912, 2012.

[112] I. Mayergoyz, M. Dimian, G. Bertotti, and C. Serpico, "Critical fields and pulse durations for precessional switching of perpendicular media," *Journal of applied physics*, vol. 97, no. 10, p. 10E509, 2005.

[113] H. Zhao, A. Lyle, Y. Zhang, P. K. Amiri, G. Rowlands, Z. Zeng, J. Katine, H. Jiang, K. Galatsis, K. L. Wang, I. N. Krivorotov, and J. P. Wang, "Low writing energy and sub nanosecond spin torque transfer switching of in-plane magnetic tunnel junction for spin torque transfer random access memory," *Journal of Applied Physics*, vol. 109, no. 2011, pp. 2009–2012, 2011.

[114] G. D. Chaves-O'Flynn, E. Vanden-Eijnden, D. L. Stein, and A. D. Kent, "Energy barriers to magnetization reversal in perpendicularly magnetized thin film nanomagnets," *Journal of Applied Physics*, vol. 113, pp. 2–5, 2013.

[115] R. Dittrich, T. Schrefl, D. Suess, W. Scholz, H. Forster, and J. Fidler, "A path method for finding energy barriers and minimum energy paths in complex micromagnetic systems," *Journal of Magnetism and Magnetic Materials*, vol. 250, pp. 12–19, 2002.

[116] G. D. Chaves-O'Flynn, D. Bedau, E. Vanden-Eijnden, A. D. Kent, and D. L. Stein, "Stability of 2π Domain Walls in Ferromagnetic Nanorings," *Magnetics, IEEE Transactions on*, vol. 46, no. 6, pp. 2272–2274, 2010.

[117] I. Tudosa, M. V. Lubarda, K. T. Chan, M. a. Escobar, V. Lomakin, and E. E. Fullerton, "Thermal stability of patterned Co/Pd nanodot arrays," *Applied Physics Letters*, vol. 100, pp. 4–7, 2012.

[118] W. E, W. Ren, and E. Vanden-Eijnden, "Simplified and improved string method for computing the minimum energy paths in barrier-crossing events," *Journal of Chemical Physics*, vol. 126, no. 2007, 2007.

[119] D. Apalkov, S. Watts, A. Driskill-Smith, E. Chen, Z. Diao, and V. Nikitin, "Comparison of scaling of in-plane and perpendicular spin transfer switching technologies by micromagnetic simulation," *IEEE Transactions on Magnetics*, vol. 46, no. 6, pp. 2240–2243, 2010.

[120] D. Weller, A. Moser, L. Folks, M. E. Best, W. Lee, M. F. Toney, M. Schwickert, J. U. Thiele, and M. F. Doerner, "High K_u materials approach to 100 Gbits/in^2," *IEEE Transactions on Magnetics*, vol. 36, pp. 10–15, Jan. 2000.

[121] R. Sbiaa, H. Meng, and S. N. Piramanayagam, "Materials with perpendicular magnetic anisotropy for magnetic random access memory," *physica status solidi (RRL) Rapid Research Letters*, vol. 5, pp. 413–419, Dec. 2011.

[122] A. F. Andresen, "A neutron diffraction investigation of Cr_2Te_3 and Cr_5Te_6," *Acta Chem. Scand.*, vol. 17, pp. 1335–1342, 1963.

[123] T. Hashimoto, K. Hoya, M. Yamaguchi, and I. Ichitsubo, "Magnetic Properties of Single Crystals $Cr_{2-\delta}Te_3$," *Journal of the Physical Society of Japan*, vol. 31, no. 3, pp. 679–682, 1971.

[124] J. Wontcheu, W. Bensch, S. Mankovsky, S. Polesya, and H. Ebert, "Effect of anion substitution onto structural and magnetic properties of chromium chalcogenides," *Progress in Solid State Chemistry*, vol. 37, no. 2-3, pp. 226–242, 2009.

[125] A. Ohsawa, Y. Yamaguchi, N. Kazama, H. Yamauchi, and H. Watanabe, "Magnetic Anisotropy of $Cr_{1-x}Te$ with x=0.077," *Journal of the Physical Society of Japan*, vol. 33, no. 5, pp. 1303–1307, 1972.

[126] L. Hui, S. T. Lim, J. F. Bi, and K. L. Teo, "Investigation on the antiferromagnetic component in the intrinsic exchange bias in structurally single phase Cr_2Te_3 thin film," *Journal of Applied Physics*, vol. 111, no. 7, p. 07D719, 2012.

[127] M. G. Sreenivasan, J. F. Bi, K. L. Teo, and T. Liew, "Systematic investigation of structural and magnetic properties in molecular beam epitaxial growth of metastable zinc-blende CrTe toward half-metallicity," *Journal of Applied Physics*, vol. 103, no. 4, p. 043908, 2008.

[128] R. Akiyama, H. Oikawa, K. Yamawaki, and S. Kuroda, "Electric-field modulation of ferromagnetism in hexagonal chromium telluride thin film," *Physica Status Solidi (C) Current Topics in Solid State Physics*, vol. 11, no. 7-8, pp. 1320–1323, 2014.

[129] J. Wontcheu, W. Bensch, S. Mankovsky, S. Polesya, and H. Ebert, "Effect of anion substitution onto structural and magnetic properties of chromium chalcogenides," *Progress in Solid State Chemistry*, vol. 37, pp. 226–242, Dec. 2009.

[130] T. Pramanik, A. Roy, R. Dey, A. Rai, S. Guchhait, H. C. Movva, C.-C. Hsieh, and S. K. Banerjee, "Angular dependence of magnetization reversal in epitaxial chromium telluride thin films with perpendicular magnetic anisotropy," *Journal of Magnetism and Magnetic Materials*, vol. 437, pp. 72 – 77, 2017.

[131] A. Roy, S. Guchhait, R. Dey, T. Pramanik, C.-C. Hsieh, A. Rai, and S. K. Banerjee, "Perpendicular Magnetic Anisotropy and Spin Glass-like Behavior in Molecular Beam Epitaxy Grown Chromium Telluride Thin Films," *ACS Nano*, vol. 9, pp. 3772–3779, Apr. 2015.

[132] A. Roy, S. Guchhait, S. Sonde, R. Dey, T. Pramanik, A. Rai, H. C. P. Movva, L. Colombo, and S. K. Banerjee, "Two-dimensional weak anti-localization in Bi_2Te_3

thin film grown on Si(111)-(7×7) surface by molecular beam epitaxy," *Applied Physics Letters*, vol. 102, no. 16, p. 163118, 2013.

[133] R. Dey, "Perpendicular And Parallel Field Magnetoresistance In Molecular Beam Epitaxy Grown Bi_2Te_3," Master's thesis, University of Texas at Austin, 2014.

[134] R. Dey, A. Roy, T. Pramanik, S. Guchhait, S. Sonde, A. Rai, L. F. Register, and S. K. Banerjee, "Localization and interaction effects of epitaxial Bi_2Se_3 bulk states in two-dimensional limit," *Journal of Applied Physics*, vol. 120, no. 16, p. 164301, 2016.

[135] R. Dey, T. Pramanik, A. Roy, A. Rai, S. Guchhait, S. Sonde, H. C. P. Movva, L. Colombo, L. F. Register, and S. K. Banerjee, "Strong spin-orbit coupling and Zeeman spin splitting in angle dependent magnetoresistance of Bi_2Te_3," *Applied Physics Letters*, vol. 104, no. 22, p. 223111, 2014.

[136] A. Roy, H. C. Movva, B. Satpati, K. Kim, R. Dey, A. Rai, T. Pramanik, S. Guchhait, E. Tutuc, and S. K. Banerjee, "Structural and electrical properties of $MoTe_2$ and $MoSe_2$ grown by molecular beam epitaxy," *ACS applied materials & interfaces*, vol. 8, no. 11, pp. 7396–7402, 2016.

[137] A. Roy, R. Ghosh, A. Rai, A. Sanne, K. Kim, H. C. P. Movva, R. Dey, T. Pramanik, S. Chowdhury, E. Tutuc, and S. K. Banerjee, "Intra-domain periodic defects in monolayer MoS_2," *Applied Physics Letters*, vol. 110, no. 20, p. 201905, 2017.

[138] W. Sucksmith and J. E. Thompson, "The Magnetic Anisotropy of Cobalt," *Proceedings of the Royal Society of London A: Mathematical, Physical and Engineering Sciences*, vol. 225, pp. 362–375, Sept. 1954.

[139] S. Purcell, M. Johnson, N. McGee, W. Zeper, and W. Hoving, "Spatially resolved magneto-optical investigation of the perpendicular anisotropy in a wedge-shaped ultrathin epitaxial Co layer on Pd (111)," *Journal of Magnetism and Magnetic Materials*, vol. 113, no. 1-3, pp. 257–263, 1992.

[140] M. G. Sreenivasan, J. F. Bi, K. L. Teo, and T. Liew, "Systematic investigation of structural and magnetic properties in molecular beam epitaxial growth of metastable zinc-blende CrTe toward half-metallicity," *Journal of Applied Physics*, vol. 103, p. 043908, Feb. 2008.

[141] R. M. Bozorth, "Magnetostriction and Crystal Anisotropy of Single Crystals of Hexagonal Cobalt," *Phys. Rev.*, vol. 96, pp. 311–316, Oct 1954.

[142] H. Stillrich, C. Menk, R. Frömter, and H. P. Oepen, "Magnetic anisotropy and the cone state in Co/Pt multilayer films," *Journal of Applied Physics*, vol. 105, no. 7, p. 07C308, 2009.

[143] J. Zhu, J. A. Katine, G. E. Rowlands, Y.-J. Chen, Z. Duan, J. G. Alzate, P. Upadhyaya, J. Langer, P. K. Amiri, K. L. Wang, and I. N. Krivorotov, "Voltage-Induced Ferromagnetic Resonance in Magnetic Tunnel Junctions," *Phys. Rev. Lett.*, vol. 108, p. 197203, May 2012.

[144] E. C. Stoner and E. P. Wohlfarth, "A Mechanism of Magnetic Hysteresis in Heterogeneous Alloys," *Philosophical Transactions of the Royal Society of London A: Mathematical, Physical and Engineering Sciences*, vol. 240, pp. 599–642, May 1948.

[145] C.-R. Chang, "Micromagnetic studies of coherent rotation with quartic crystalline anisotropy," *Journal of Applied Physics*, vol. 69, pp. 2431–2439, Feb. 1991.

[146] A. Singh, V. Neu, S. Fähler, K. Nenkov, L. Schultz, and B. Holzapfel, "Relevance of pinning, nucleation, and interaction in nanograined epitaxial hard magnetic $SmCo_5$ films," *Physical Review B*, vol. 79, p. 214401, June 2009.

[147] T. Thomson, G. Hu, and B. D. Terris, "Intrinsic Distribution of Magnetic Anisotropy in Thin Films Probed by Patterned Nanostructures," *Physical Review Letters*, vol. 96, p. 257204, June 2006.

[148] H. Kronmüller, "Theory of Nucleation Fields in Inhomogeneous Ferromagnets," *physica status solidi (b)*, vol. 144, pp. 385–396, Nov. 1987.

[149] A. Sakuma, S. Tanigawa, and M. Tokunaga, "Micromagnetic studies of inhomogeneous nucleation in hard magnets," *Journal of Magnetism and Magnetic Materials*, vol. 84, pp. 52–58, Feb. 1990.

[150] R. Friedberg and D. I. Paul, "New Theory of Coercive Force of Ferromagnetic Materials," *Physical Review Letters*, vol. 34, pp. 1234–1237, May 1975.

[151] A. Sakuma, "The theory of inhomogeneous nucleation in uniaxial ferromagnets," *Journal of Magnetism and Magnetic Materials*, vol. 88, pp. 369–375, Aug. 1990.

[152] R. Heindl, W. H. Rippard, S. E. Russek, and A. B. Kos, "Physical limitations to efficient high-speed spin-torque switching in magnetic tunnel junctions," *Physical Review B*, vol. 83, p. 054430, Feb. 2011.

[153] J. Z. Sun, R. P. Robertazzi, J. Nowak, P. L. Trouilloud, G. Hu, D. W. Abraham, M. C. Gaidis, S. L. Brown, E. J. O'Sullivan, W. J. Gallagher, and D. C. Worledge, "Effect of subvolume excitation and spin-torque efficiency on magnetic switching," *Physical Review B*, vol. 84, p. 064413, Aug. 2011.

[154] T. Min, Q. Chen, R. Beach, G. Jan, C. Horng, W. Kula, T. Torng, R. Tong, T. Zhong, D. Tang, P. Wang, M. m. Chen, J. Z. Sun, J. K. Debrosse, D. C. Worledge, T. M. Maffitt, and W. J. Gallagher, "A Study of Write Margin of Spin Torque Transfer Magnetic Random Access Memory Technology," *IEEE Transactions on Magnetics*, vol. 46, pp. 2322–2327, June 2010.

[155] E. R. Evarts, R. Heindl, W. H. Rippard, and M. R. Pufall, "Correlation of anomalous write error rates and ferromagnetic resonance spectrum in spin-transfer-torque-magnetic-random-access-memory devices containing in-plane free layers," *Applied Physics Letters*, vol. 104, p. 212402, May 2014.

[156] K. Kawabata, M. Tanizawa, K. Ishikawa, and Y. Inoue, "Micro magnetic simulation of write error probability in STT-MRAM," in *International Conference on Simulation of Semiconductor Processes and Devices, 2008. SISPAD 2008*, pp. 53–56, Sept. 2008.

[157] U. Roy, D. L. Kencke, T. Pramanik, L. F. Register, and S. K. Banerjee, "Write error rate in spin-transfer-torque random access memory including micromagnetic effects," in *Device Research Conference (DRC), 2015 73rd Annual*, pp. 147–148, June 2015.

[158] U. Roy, T. Pramanik, L. F. Register, and S. K. Banerjee, "Write Error Rate of Spin-Transfer-Torque Random Access Memory Including Micromagnetic Effects Using Rare Event Enhancement," *IEEE Transactions on Magnetics*, vol. 52, pp. 1–6, Oct. 2016.

[159] E. Sangiorgi, B. Ricco, and F. Venturi, "MOS^2: an efficient Monte Carlo Simulator for MOS devices," *IEEE Transactions on Computer-Aided Design of Integrated Circuits and Systems*, vol. 7, pp. 259–271, Feb. 1988.

[160] D. Querlioz, J. Saint-Martin, K. Huet, A. Bournel, V. Aubry-Fortuna, C. Chassat, S. Galdin-Retailleau, and P. Dollfus, "On the Ability of the Particle Monte Carlo Technique to Include Quantum Effects in Nano-MOSFET Simulation," *IEEE Transactions on Electron Devices*, vol. 54, pp. 2232–2242, Sept. 2007.

[161] W. Scholz, T. Schrefl, and J. Fidler, "Micromagnetic simulation of thermally activated switching in fine particles," *Journal of Magnetism and Magnetic Materials*, vol. 233, pp. 296–304, Aug. 2001.

[162] Y. Xie, B. Behin-Aein, and A. W. Ghosh, "Fokker Planck Study of Parameter Dependence on Write Error Slope in Spin-Torque Switching," *IEEE Transactions on Electron Devices*, vol. 64, pp. 319–324, Jan. 2017.

[163] M. J. J. Garvels, *The splitting method in rare event simulation*. PhD thesis, University of Twente, Oct. 2000.

[164] M. J. J. Garvels and D. P. Kroese, "A comparison of RESTART implementations," in *Simulation Conference Proceedings, 1998. Winter*, vol. 1, pp. 601–608 vol.1, Dec. 1998.

[165] P. Glasserman, P. Heidelberger, P. Shahabuddin, and T. Zajic, "Multilevel Splitting for Estimating Rare Event Probabilities," *Oper. Res.*, vol. 47, pp. 585–600, Apr. 1999.

[166] G. Rubino and B. Tuffin, *Rare Event Simulation Using Monte Carlo Methods*. Wiley Publishing, 2009.

[167] F. Iga, Y. Yoshida, S. Ikeda, T. Hanyu, H. Ohno, and T. Endoh, "Time-Resolved Switching Characteristic in Magnetic Tunnel Junction with Spin Transfer Torque Write Scheme," *Japanese Journal of Applied Physics*, vol. 51, p. 02BM02, Feb. 2012.

[168] K. Ito, S. Ohuchida, and T. Endoh, "Dependence of Sub-Volume Excitation on Structural and Material Parameters in Precessional Regime of Spin Transfer Torque Magnetization Reversal," *IEEE Transactions on Magnetics*, vol. 50, pp. 1–4, Nov. 2014.

[169] S. Ohuchida, K. Ito, and T. Endoh, "Impact of sub-volume excitation on improving overdrive delay product of sub-40 nm perpendicular magnetic tunnel junctions in adiabatic regime and its beyond," *Japanese Journal of Applied Physics*, vol. 54, p. 04DD05, Apr. 2015.

[170] A. F. Vincent, N. Locatelli, J. O. Klein, W. S. Zhao, S. Galdin-Retailleau, and D. Querlioz, "Analytical Macrospin Modeling of the Stochastic Switching Time of Spin-Transfer Torque Devices," *IEEE Transactions on Electron Devices*, vol. 62, pp. 164–170, Jan. 2015.

[171] Y. Acremann, J. P. Strachan, V. Chembrolu, S. D. Andrews, T. Tyliszczak, J. A. Katine, M. J. Carey, B. M. Clemens, H. C. Siegmann, and J. Stöhr, "Time-Resolved Imaging of Spin Transfer Switching: Beyond the Macrospin Concept," *Physical Review Letters*, vol. 96, p. 217202, May 2006.

[172] S. V. Aradhya, G. E. Rowlands, J. Oh, D. C. Ralph, and R. A. Buhrman, "Nanosecond-Timescale Low Energy Switching of In-Plane Magnetic Tunnel Junctions through

Dynamic Oersted-Field-Assisted Spin Hall Effect," *Nano Letters*, vol. 16, pp. 5987–5992, Oct. 2016.

[173] G. E. Rowlands, S. V. Aradhya, S. Shi, E. H. Yandel, J. Oh, D. C. Ralph, and R. A. Buhrman, "Nanosecond magnetization dynamics during spin Hall switching of in-plane magnetic tunnel junctions," *Applied Physics Letters*, vol. 110, p. 122402, Mar. 2017.

[174] U. Roy, R. Dey, T. Pramanik, B. Ghosh, L. F. Register, and S. K. Banerjee, "Magnetization switching of a metallic nanomagnet via current-induced surface spin-polarization of an underlying topological insulator," *Journal of Applied Physics*, vol. 117, p. 163906, Apr. 2015.

[175] Y. Wang, D. Zhu, Y. Wu, Y. Yang, J. Yu, R. Ramaswamy, R. Mishra, S. Shi, M. Elyasi, K.-L. Teo, *et al.*, "Room temperature magnetization switching in topological insulator-ferromagnet heterostructures by spin-orbit torques," *Nature Communications*, vol. 8, no. 1, p. 1364, 2017.

[176] J. Han, A. Richardella, S. A. Siddiqui, J. Finley, N. Samarth, and L. Liu, "Room-temperature spin-orbit torque switching induced by a topological insulator," *Phys. Rev. Lett.*, vol. 119, p. 077702, Aug 2017.

[177] R. Dey, A. Roy, T. Pramanik, A. Rai, S. H. Shin, S. Majumder, L. F. Register, and S. K. Banerjee, "Detection of current induced spin polarization in epitaxial Bi_2Te_3 thin film," *Applied Physics Letters*, vol. 110, no. 12, p. 122403, 2017.

[178] T. Trivedi, A. Roy, H. C. P. Movva, E. S. Walker, S. R. Bank, D. P. Neikirk, and S. K. Banerjee, "Versatile Large-Area Custom-Feature van der Waals Epitaxy of Topological Insulators," *ACS Nano*, vol. 11, no. 7, pp. 7457–7467, 2017. PMID: 28692797.

[179] K.-J. Lee and B. Dieny, "Micromagnetic investigation of the dynamics of magnetization switching induced by a spin polarized current," *Applied Physics Letters*, vol. 88, p. 132506, Mar. 2006.

[180] G. Finocchio, M. Carpentieri, B. Azzerboni, L. Torres, E. Martinez, and L. Lopez-Diaz, "Micromagnetic simulations of nanosecond magnetization reversal processes in magnetic nanopillar," *Journal of Applied Physics*, vol. 99, p. 08G522, Apr. 2006.

[181] K. Ito, T. Devolder, C. Chappert, M. J. Carey, and J. A. Katine, "Micromagnetic simulation on effect of oersted field and hard axis field in spin transfer torque switching," *Journal of Physics D: Applied Physics*, vol. 40, no. 5, p. 1261, 2007.

[182] D. Aurélio, L. Torres, and G. Finocchio, "Thermal effects on spin-torque-driven switching in high-tunneling-magnetoresistance magnetic tunnel junctions," *Journal of Applied Physics*, vol. 108, p. 083911, Oct. 2010.

[183] R. D. McMichael and M. D. Stiles, "Magnetic normal modes of nanoelements," *Journal of Applied Physics*, vol. 97, p. 10J901, May 2005.

[184] J. Z. Sun, M. C. Gaidis, G. Hu, E. J. O'Sullivan, S. L. Brown, J. J. Nowak, P. L. Trouilloud, and D. C. Worledge, "High-bias backhopping in nanosecond time-domain spin-torque switches of MgO-based magnetic tunnel junctions," *Journal of Applied Physics*, vol. 105, p. 07D109, Feb. 2009.

[185] Y. Acremann, C. H. Back, M. Buess, D. Pescia, and V. Pokrovsky, "Bifurcation in precessional switching," *Applied Physics Letters*, vol. 79, pp. 2228–2230, Sept. 2001.

[186] R. Heindl, W. H. Rippard, S. E. Russek, and M. R. Pufall, "Time-domain analysis of spin-torque induced switching paths in nanoscale CoFeB/MgO/CoFeB magnetic tunnel junction devices," *Journal of Applied Physics*, vol. 116, p. 243902, Dec. 2014.

[187] H. Tomita, K. Konishi, T. Nozaki, H. Kubota, A. Fukushima, K. Yakushiji, S. Yuasa, Y. Nakatani, T. Shinjo, M. Shiraishi, and Y. Suzuki, "Single-Shot Measurements of Spin-Transfer Switching in CoFeB/MgO/CoFeB Magnetic Tunnel Junctions," *Applied Physics Express*, vol. 1, p. 061303, May 2008.

[188] T. Devolder, J. Hayakawa, K. Ito, H. Takahashi, S. Ikeda, P. Crozat, N. Zerounian, J.-V. Kim, C. Chappert, and H. Ohno, "Single-Shot Time-Resolved Measurements of Nanosecond-Scale Spin-Transfer Induced Switching: Stochastic Versus Deterministic Aspects," *Physical Review Letters*, vol. 100, p. 057206, Feb. 2008.

[189] B. Lacoste, M. M. de Castro, T. Devolder, R. C. Sousa, L. D. Buda-Prejbeanu, S. Auffret, U. Ebels, C. Ducruet, I. L. Prejbeanu, L. Vila, B. Rodmacq, and B. Dieny, "Modulating spin transfer torque switching dynamics with two orthogonal spin-polarizers by varying the cell aspect ratio," *Physical Review B*, vol. 90, p. 224404, Dec. 2014.

[190] K.-J. Lee, A. Deac, O. Redon, J.-P. Nozières, and B. Dieny, "Excitations of incoherent spin-waves due to spin-transfer torque," *Nature Materials*, vol. 3, pp. 877–881, Dec. 2004.

[191] Z. Wang, Y. Zhou, J. Zhang, and Y. Huai, "Bit error rate investigation of spin-transfer-switched magnetic tunnel junctions," *Applied Physics Letters*, vol. 101, p. 142406, Oct. 2012.

[192] J. P. Strachan, V. Chembrolu, Y. Acremann, X. W. Yu, A. A. Tulapurkar, T. Tyliszczak, J. A. Katine, M. J. Carey, M. R. Scheinfein, H. C. Siegmann, and J. Stöhr, "Direct Observation of Spin-Torque Driven Magnetization Reversal through Nonuniform Modes," *Physical Review Letters*, vol. 100, p. 247201, June 2008.

[193] V. Chembrolu, J. P. Strachan, X. W. Yu, A. A. Tulapurkar, T. Tyliszczak, J. A. Katine, M. J. Carey, J. Stöhr, and Y. Acremann, "Time-resolved x-ray imaging of magnetization dynamics in spin-transfer torque devices," *Physical Review B*, vol. 80, p. 024417, July 2009.

[194] D. Aurélio, L. Torres, and G. Finocchio, "Magnetization switching driven by spin-transfer-torque in high-TMR magnetic tunnel junctions," *Journal of Magnetism and Magnetic Materials*, vol. 321, pp. 3913–3920, Dec. 2009.

[195] T. Aoki, Y. Ando, M. Oogane, and H. Naganuma, "Dynamic Magnetic Intermediate State during Nanosecond Spin Transfer Switching for MgO-Based Magnetic Tunnel Junctions," *Applied Physics Express*, vol. 3, p. 053002, Apr. 2010.

[196] R. Tomasello, V. Puliafito, B. Azzerboni, and G. Finocchio, "Switching Properties in Magnetic Tunnel Junctions With Interfacial Perpendicular Anisotropy: Micromagnetic Study," *IEEE Transactions on Magnetics*, vol. 50, pp. 1–5, July 2014.

[197] G. D. Chaves-O'Flynn, G. Wolf, D. Pinna, and A. D. Kent, "Micromagnetic study of spin transfer switching with a spin polarization tilted out of the free layer plane," *Journal of Applied Physics*, vol. 117, p. 17D705, Feb. 2015.

[198] W. L. Lim, A. Higgins, and S. Urazhdin, "Measurements of out-of-plane dynamics induced in magnetic nanopillars by spin transfer," *Phys. Rev. B*, vol. 80, p. 104408, Sep 2009.

[199] R. Hertel and C. M. Schneider, "Exchange explosions: Magnetization dynamics during vortex-antivortex annihilation," *Phys. Rev. Lett.*, vol. 97, p. 177202, Oct 2006.

[200] A. Thiaville, J. M. García, R. Dittrich, J. Miltat, and T. Schrefl, "Micromagnetic study of Bloch-point-mediated vortex core reversal," *Phys. Rev. B*, vol. 67, p. 094410, Mar 2003.

[201] M. D. Stiles and J. Miltat, *Spin-Transfer Torque and Dynamics*, pp. 225–308. Springer Berlin Heidelberg, 2006.

[202] K. M. Lebecki, D. Hinzke, U. Nowak, and O. Chubykalo-Fesenko, "Key role of temperature in ferromagnetic Bloch point simulations," *Physical Review B*, vol. 86, p. 094409, Sept. 2012.

[203] J. H. Han, "Solitons and Homotopy," in *Skyrmions in Condensed Matter*, Springer Tracts in Modern Physics, pp. 19–43, Springer, Cham, 2017. DOI: 10.1007/978-3-319-69246-3_2.